Politecnico di Torino

DIPARTIMENTO DI INGEGNERIA ELETTRICA
Corso di Dottorato di Ricerca in Ingegneria Elettrica

EXPERIMENTAL AND MODELING ANALYSIS OF ELECTRIC SYSTEMS WITH HIGH CAPACITIVE AND INDUCTIVE COUPLINGS

Ph.D. Thesis

Candidato:
Ing. Andrea Morando

Relatori:
Prof. Mario Chiampi

Dott.ssa Gabriella Crotti

Ing. Michele Borsero

XXIV Ciclo

Contents

List of Figures

List of Tables

Chapter 1

Dissertation Overview

The present doctoral thesis *Experimental and Modeling Analysis of Electric Systems with High Capacitive and Inductive Couplings* investigates several kinds of electromagnetic coupling which influence strongly the electric system operation.

The electromagnetic coupling is a fundamental phenomenon that governs the behaviour of many electrical devices, but on the other hand can produce detrimental effects on their performances. In particular, electrical devices are frequently dominated by non-ideal parameters, attributable to circuital, geometrical or environmental issues. Electrical engineering deals with the possibility to reduce non-ideality as much as possible through appropriate design solutions and modelling analysis.

The influence and the modelling of the electromagnetic coupling is strongly dependent on the operating frequency. In order to develop a whole analysis, two of the furthest extreme examples in the frequency range are presented and deeply investigated in the present work. The first issue concerns the Rogowski coil operating conditions at power frequency and the analysis is carried out by means of experimental and modelling activities (Chapter 3). The second case regards the calibration set-up of electrostatic discharge (ESD) generators, used in the EMC immunity test for electric and electronic equipment. Since the ESD waveform is a transient characterized by short rise time and important peaks, the stray capacitive and inductive parameters play a fundamental role in stating the compliance with the EMC international standards (Chapter 4).

The intent to support in a comprehensive way the described phenomena with a simulation tool is considered by developing a suitable numerical model, based on the Partial Element Equivalent Circuit (PEEC) method (Chapter 5). The consideration of arbitrary three-dimensional geometry of interconnections and the feature of full-wave method can allow to take into account

properly the electromagnetic behaviour of the above electric systems.

Chapter 2 shortly summarizes the fundamentals of electromagnetic theory, which are necessary to understand the following chapters. The dynamic behaviour of passive interconnections is governed by equations of classical electrodynamics, which are the basis for the derivation of models considered in Chapters 3 - 5. In addition, Chapter 2 introduces some important concepts and techniques of electrodynamics: uniqueness and causality of solutions, reciprocity theorem, image theory, Sommerfeld radiation boundary condition and the Green's function method.

Chapter 3 deals with a modelling analysis which is able to predict the Rogowski coil performances at power frequency when operating under non-ideal conditions. The numerical tool can be employed both in the design phase and the evaluation of the mutual inductance variation as a function of the coil structure and the power circuit arrangement. The use of the model, together with a propagation distribution approach based on Monte Carlo method, allows to evaluate the measurement uncertainty for those on-site arrangements where only a range of variations of the influence parameters can be estimated.

Chapter 4 is focused on the detection and analysis of those stray and measuring parameters related to the calibration set-up of an ESD generator, that contribute to affect strongly the measurement result. The aim of the chapter is to underline the influence of several critical quantities and to warn the laboratory operators about the efforts that should be made during the calibration procedure.

Chapter 5 starts from the generalized formulation of the PEEC (Partial Element Equivalent Circuit) method, which is considered one of the most suitable numerical methods for the simulation of passive interconnections. As all integral-equation techniques, PEEC method requires only the discretization of the conducting structures and not the total solution region. This is the most important advantage with respect to differential methods, since the number of unknowns in the resulting algebraic-equation formulation decreases strongly, although the system matrix is fully-filled. This chapter is then focused on the development of an original software devoted to the PEEC modelling, with special attention to the meshing technique issues, the partial element computational algorithms and relative validation process. In the end, the numerical solver for time- and frequency-domain and the future applications are deeply explained.

Chapter 2

Electromagnetic Fields Theory and Computational Methods

In this chapter a brief overview is given on the basic equations and definitions used in the electrodynamics theory. The intention is to introduce all the concepts useful for this dissertation. In the end, a look at the main analytical and numerical methods involved in the electromagnetic fields computation are presented [1].

2.1 Fundamental equations and definitions

2.1.1 Maxwell's equations

Maxwell's equations are four partial differential equations relating four field vectors and four field sources at the space point $\mathbf{r}$ and at the time t:

$$\begin{aligned}
\nabla \times \mathbf{E}(\mathbf{r},t) &= -\frac{\partial \mathbf{B}(\mathbf{r},t)}{\partial t} - \mathbf{M}(\mathbf{r},t), \\
\nabla \times \mathbf{H}(\mathbf{r},t) &= \frac{\partial \mathbf{D}(\mathbf{r},t)}{\partial t} + \mathbf{J}(\mathbf{r},t) \\
\nabla \cdot \mathbf{D}(\mathbf{r},t) &= \rho_v(\mathbf{r},t) \\
\nabla \cdot \mathbf{B}(\mathbf{r},t) &= \rho_v^m(\mathbf{r},t)
\end{aligned} \tag{2.1}$$

where $\mathbf{E}(\mathbf{r},t)$ is the electric field vector, $\mathbf{H}(\mathbf{r},t)$ is the magnetic field vector, $\mathbf{D}(\mathbf{r},t)$ is the electric flux density vector, $\mathbf{B}(\mathbf{r},t)$ is the magnetic flux density vector. $\mathbf{J}(\mathbf{r},t)$ and $\mathbf{M}(\mathbf{r},t)$ are the electric and magnetic current density vectors, respectively. $\rho_v(\mathbf{r},t)$ and $\rho_v^m(\mathbf{r},t)$ are the volumetric density of electric and magnetic charges. Since the magnetic currents and charges do not exist in reality, we set $\mathbf{M}(\mathbf{r},t)$=0 and $\rho_v^m(\mathbf{r},t)$= 0. The inclusion of these additional

formal sources in Maxwell's equations makes the system symmetric and leads to derivation of some important electromagnetic principles.

Maxwell's equations can be significantly simplified in the frequency domain. They are derived by the application of the direct Fourier transformation to the previous equations:

$$\begin{aligned} \nabla \times \mathbf{E}(\mathbf{r}) &= -j\omega \mathbf{B}(\mathbf{r}) - \mathbf{M}(\mathbf{r}) \\ \nabla \times \mathbf{H}(\mathbf{r}) &= j\omega \mathbf{D}(\mathbf{r}) + \mathbf{J}(\mathbf{r}) \\ \nabla \cdot \mathbf{D}(\mathbf{r}) &= \rho_v(\mathbf{r}) \\ \nabla \cdot \mathbf{B}(\mathbf{r}) &= \rho_v^m(\mathbf{r}) \end{aligned} \tag{2.2}$$

where $\mathbf{E}(\mathbf{r})$, $\mathbf{H}(\mathbf{r})$, $\mathbf{B}(\mathbf{r})$, $\mathbf{D}(\mathbf{r})$, $\mathbf{M}(\mathbf{r})$, $\mathbf{J}(\mathbf{r})$, $\rho_v^m(\mathbf{r})$, and $\rho_v(\mathbf{r})$ are complex vector or scalar functions called phasors, which are the frequency-domain counterparts for the corresponding functions calculated as follows:

$$\mathbf{A}(\mathbf{r}) = \Im\left\{\mathbf{A}(\mathbf{r}, t)\right\},$$

where $\Im\{\}$ denotes the Fourier transformation, $\mathbf{A}(\mathbf{r}$,t) is a space and time-domain function, and $\mathbf{A}(\mathbf{r})$ is its frequency-domain counterpart.

The continuity equations for electric and magnetic sources are developed through the application of the divergence operator to the first and second equations in (1.2):

$$\nabla \cdot \mathbf{J}(\mathbf{r}) + j\omega\rho_v(\mathbf{r}) = 0 \tag{2.3}$$

$$\nabla \cdot \mathbf{M}(\mathbf{r}) + j\omega\rho_v^m(\mathbf{r}) = 0 \tag{2.4}$$

The material equations relate the electric and magnetic flux densities to the electric and magnetic field intensities, respectively:

$$\mathbf{D}(\mathbf{r}) = \overline{\overline{\varepsilon}} \cdot \mathbf{E}(\mathbf{r}) \tag{2.5}$$

$$\mathbf{B}(\mathbf{r}) = \overline{\overline{\mu}} \cdot \mathbf{H}(\mathbf{r}) \tag{2.6}$$

where $\overline{\overline{\varepsilon}} = \overline{\overline{\varepsilon}}(\mathbf{r}, j\omega)$ is the permittivity, and $\overline{\overline{\mu}} = \overline{\overline{\mu}}(\mathbf{r}, j\omega)$ is the permeability. In general, they are dyadic functions of space coordinates and frequency that corresponds to a linear anisotropic and non-uniform media.

However, (2.5),(2.6) may be simplified to the usually implied formulation in the case of an isotropic linear media:

$$\mathbf{D}(\mathbf{r}) = \varepsilon\mathbf{E}(\mathbf{r}) \tag{2.7}$$

$$\mathbf{B}(\mathbf{r}) = \mu\mathbf{H}(\mathbf{r}) \tag{2.8}$$

where $\varepsilon = \varepsilon_0\varepsilon_r$ and $\mu = \mu_0\mu_r$, ε_r and μ_r are the relative permittivity and permeability, $\varepsilon_0 = 8.854 \cdot 10^{-12}$ F/m is the dielectric constant, and $\mu_0 = 4\pi \cdot 10^{-7}$ H/m is the magnetic constant.

The substitution of the material equations (2.5),(2.6) into Maxwell's equations (2.2) results in two independent curl equations relating the vectors $\mathbf{E}(\mathbf{r})$ and $\mathbf{H}(\mathbf{r})$:

$$\begin{aligned} \nabla \times \mathbf{E}(\mathbf{r}) &= -j\omega\overline{\overline{\mu}} \cdot \mathbf{H}(\mathbf{r}) - \mathbf{M}(\mathbf{r}) \\ \nabla \times \mathbf{H}(\mathbf{r}) &= j\omega\overline{\overline{\varepsilon}} \cdot \mathbf{E}(\mathbf{r}) + \mathbf{J}(\mathbf{r}) \end{aligned} \tag{2.9}$$

for anisotropic medium or

$$\begin{aligned} \nabla \times \mathbf{E}(\mathbf{r}) &= -j\omega\mu\mathbf{H}(\mathbf{r}) - \mathbf{M}(\mathbf{r}) \\ \nabla \times \mathbf{H}(\mathbf{r}) &= j\omega\varepsilon\mathbf{E}(\mathbf{r}) + \mathbf{J}(\mathbf{r}) \end{aligned} \tag{2.10}$$

for isotropic one.

2.1.2 Wave equations

The system of the first order partial differential equations (2.9) can be decoupled into two second order partial differential equations called *vector wave* equations:

$$\begin{aligned} \nabla \times \overline{\overline{\mu}}^{-1} \cdot \nabla \times \mathbf{E}(\mathbf{r}) - \omega^2\overline{\overline{\varepsilon}} \cdot \mathbf{E}(\mathbf{r}) &= -j\omega\mathbf{J}(\mathbf{r}) - \nabla \times \overline{\overline{\mu}}^{-1} \cdot \mathbf{M}(\mathbf{r}) \\ \nabla \times \overline{\overline{\varepsilon}}^{-1} \cdot \nabla \times \mathbf{H}(\mathbf{r}) - \omega^2\overline{\overline{\mu}} \cdot \mathbf{H}(\mathbf{r}) &= -j\omega\mathbf{M}(\mathbf{r}) + \nabla \times \overline{\overline{\varepsilon}}^{-1} \cdot \mathbf{J}(\mathbf{r}) \end{aligned} \tag{2.11}$$

The solution of either wave equation in (2.11) provides the complete description of the electromagnetic field in the solution region. The formulation (2.11) for the vector wave equations is simplified for an isotropic and homogeneous medium as:

$$\begin{aligned} \nabla \times \nabla \times \mathbf{E}(\mathbf{r}) - k^2\mathbf{E}(\mathbf{r}) &= -j\omega\mu\mathbf{J}(\mathbf{r}) - \nabla \times \mathbf{M}(\mathbf{r}) \\ \nabla \times \nabla \times \mathbf{H}(\mathbf{r}) - k^2\mathbf{H}(\mathbf{r}) &= -j\omega\varepsilon\mathbf{M}(\mathbf{r}) + \nabla \times \mathbf{J}(\mathbf{r}) \end{aligned} \tag{2.12}$$

where $k = \omega\sqrt{\mu\varepsilon}$ is the wavenumber. The *scalar wave* equations also named *Helmholtz* equations are derived from (2.12) in view of a vector identity and a dyadic identity as:

$$\begin{aligned} \nabla^2\mathbf{E}(\mathbf{r}) + k^2\mathbf{E}(\mathbf{r}) &= j\omega\mu\left(\overline{\overline{I}} + \frac{\nabla\nabla}{k^2}\right) \cdot \mathbf{J}(\mathbf{r}) + \nabla \times \mathbf{M}(\mathbf{r}) \\ \nabla^2\mathbf{H}(\mathbf{r}) + k^2\mathbf{H}(\mathbf{r}) &= j\omega\varepsilon\left(\overline{\overline{I}} + \frac{\nabla\nabla}{k^2}\right) \cdot \mathbf{M}(\mathbf{r}) - \nabla \times \mathbf{J}(\mathbf{r}) \end{aligned} \tag{2.13}$$

where I is the identity dyadic, and the notation $\nabla\nabla$ means dyad. Below the Helmholtz equations for the electric and magnetic fields (2.13) are given for the source-free medium in the homogeneous form:

$$\begin{aligned} \nabla^2\mathbf{E}(\mathbf{r}) + k^2\mathbf{E}(\mathbf{r}) = 0 \\ \nabla^2\mathbf{H}(\mathbf{r}) + k^2\mathbf{H}(\mathbf{r}) = 0 \end{aligned} \tag{2.14}$$

2.2 Some important theorems in electromagnetics

2.2.1 Uniqueness theorem

The uniqueness theorem specifies the necessary conditions needed for a unique solution of an electromagnetic problem.

We consider a problem described by the wave equations (2.12) in the solution region V constrained with a closed surface $S = \partial V$. Assuming the existence of two different solutions $\mathbf{E}_1(\mathbf{r})$ and $\mathbf{E}_2(\mathbf{r})$ for the same excitation, we may write:

$$\begin{aligned} \nabla \times \nabla \times \mathbf{E}_1(\mathbf{r}) - k^2\mathbf{E}_1(\mathbf{r}) = -j\omega\mu\mathbf{J}(\mathbf{r}) - \nabla \times \mathbf{M}(\mathbf{r}) \\ \nabla \times \nabla \times \mathbf{E}_2(\mathbf{r}) - k^2\mathbf{E}_2(\mathbf{r}) = -j\omega\mu\mathbf{J}(\mathbf{r}) - \nabla \times \mathbf{M}(\mathbf{r}) \end{aligned} \tag{2.15}$$

The subtraction of the first equation (2.15) from the second one yields:

$$\begin{aligned} \nabla \times \nabla \times \mathbf{E}_\delta(\mathbf{r}) - k^2\mathbf{E}_\delta(\mathbf{r}) = 0 \\ with \quad \mathbf{E}_\delta(\mathbf{r}) = \mathbf{E}_2(\mathbf{r}) - \mathbf{E}_1(\mathbf{r}) \end{aligned} \tag{2.16}$$

The condition $\mathbf{E}_\delta(\mathbf{r}) = 0$, $r \in V$ guarantees that both solutions are equal and, consequently, unique. In order to prove this condition, we write the volume integral over V of the scalar product $\mathbf{E}^*_\delta(\mathbf{r})\cdot$ (2.16):

$$\iiint\limits_V \mathbf{E}^*_\delta(\mathbf{r}) \cdot (\nabla \times \nabla \times \mathbf{E}_\delta(\mathbf{r}))dV = k^2 \iiint\limits_V \mathbf{E}^*_\delta(\mathbf{r}) \cdot \mathbf{E}_\delta(\mathbf{r})dV \tag{2.17}$$

The kernel of the right-hand side integral in (2.17) may be more or equal to zero. Since it is zero if and only if $\mathbf{E}_\delta(\mathbf{r}) = 0$, the right-hand side integral is equal to zero if and only if the solution is unique. Hence, the solution is unique if the left-hand side integral in (2.17) is zero. The left-hand side integral can be rewritten as:

$$\iiint\limits_V \mathbf{E}^*_\delta(\mathbf{r}) \cdot (\nabla \times \nabla \times \mathbf{E}_\delta(\mathbf{r}))dV = j\omega\mu \oint\limits_S \mathbf{H}_\delta(\mathbf{r}) \cdot (\hat{\mathbf{n}} \times \mathbf{E}^*_\delta(\mathbf{r}))dS \tag{2.18}$$

One may observe (2.18) and formulate the theorem, which is proved above for a homogeneous medium, but may be applied in all cases. The boundary-value problem formulated as

- ◇ a wave equation with
- ◇ non contradicting boundary conditions for the tangential component of either electric or magnetic field intensity

has a unique solution.

2.2.2 Sommerfeld radiation condition

The *Sommerfeld radiation condition* introduced by A. Sommerfeld is used for the correct formulation of open or partially open boundary-value problems. According to the uniqueness theorem, solutions of these problems are not unique if the boundary condition is not defined. The Sommerfeld radiation condition defines the electric and magnetic field intensities at infinitely large distances from the scatterer equal to zero, which allows one to obtain a unique solution. The apparent voluntarism of this definition has a rigorous physical explanation. The solution in the proximity of the scatterer consists of only outgoing waves, while incoming waves cannot appear there because of the infinite propagation time from the boundary. The outgoing waves get the finite energy from the scatterer. As any medium has a dissipation, the energy of the outgoing wave decreases towards increasing the distance from the scatterer and yields zero at infinite distance. The Sommerfeld radiation condition is applicable for not dissipative media also, since the artificial introduction of a tiny dissipation does not change the solution in the scatterer proximity, but results in zero fields at the infinite distance.

2.2.3 Reciprocity theorem

The *Lorentz reciprocity theorem* is one of the most useful tools in the electromagnetic theory. In the following, the reciprocity theorem is derived for an anisotropic linear medium with a symmetric dyadic permittivity and permeability, that is $\overline{\overline{\varepsilon}} \cdot \mathbf{E} = \mathbf{E} \cdot \overline{\overline{\varepsilon}}$ and $\overline{\overline{\mu}} \cdot \mathbf{H} = \mathbf{H} \cdot \overline{\overline{\mu}}$. We suppose that the electromagnetic field in the volume V is excited by two various systems of sources, we denote by E_1 and H_1 the field intensities caused by the electric and magnetic currents J_1 and M_1, while E_2 and H_2 are resulted by J_2 and M_2. Maxwell's equations (2.9) for both excitations are:

$$\nabla \times \mathbf{E_1}(\mathbf{r}) = -j\omega\overline{\overline{\mu}} \cdot \mathbf{H_1}(\mathbf{r}) - \mathbf{M_1}(\mathbf{r}) \tag{2.19}$$
$$\nabla \times \mathbf{H_1}(\mathbf{r}) = j\omega\overline{\overline{\varepsilon}} \cdot \mathbf{E_1}(\mathbf{r}) + \mathbf{J_1}(\mathbf{r})$$

and

$$\nabla \times \mathbf{E_2}(\mathbf{r}) = -j\omega\overline{\overline{\mu}} \cdot \mathbf{H_2}(\mathbf{r}) - \mathbf{M_2}(\mathbf{r}) \tag{2.20}$$
$$\nabla \times \mathbf{H_2}(\mathbf{r}) = j\omega\overline{\overline{\varepsilon}} \cdot \mathbf{E_2}(\mathbf{r}) + \mathbf{J_2}(\mathbf{r})$$

The substitution of (2.19) and (2.20) into the expression $\nabla \cdot (\mathbf{E_1} \times \mathbf{H_2} - \mathbf{E_2} \times \mathbf{H_1})$ leads to the equation:

$$\nabla \cdot (\mathbf{E_1} \times \mathbf{H_2} - \mathbf{E_2} \times \mathbf{H_1}) = \mathbf{H_1} \cdot \mathbf{M_2} + \mathbf{E_2} \cdot \mathbf{J_1} - \mathbf{H_2} \cdot \mathbf{M_1} - \mathbf{E_1} \cdot \mathbf{J_2} \tag{2.21}$$

which may be integrated over the volume V. The application of the Gauss theorem to this integral gives the final formulation for the reciprocity theorem:

$$\oint\limits_{S=\partial V} (\mathbf{E_1} \times \mathbf{H_2} - \mathbf{E_2} \times \mathbf{H_1}) \cdot d\mathbf{S} = \iiint\limits_{V} (\mathbf{H_1} \cdot \mathbf{M_2} + \mathbf{E_2} \cdot \mathbf{J_1} - \mathbf{H_2} \cdot \mathbf{M_1} - \mathbf{E_1} \cdot \mathbf{J_2}) dV \tag{2.22}$$

where $S = \partial V$ is the closed boundary of the volume V, and the direction of $d\mathbf{S}$ is the outward normal to the boundary.

2.2.4 Image theory for a perfectly conducting infinite plane

The electromagnetic field produced by a scatterer may be changed by obstacles in its proximity. One of the most wide-spread obstacles, which appear in problems related to passive interconnection structures, is the well conducting ground plane. A large number of objects may be considered as ground planes, e.g., the conducting earth surface, conducting device cases, metallized layers in printed circuit boards, etc.

A scatterer located in the proximity of a perfectly conducting plane may be simply described using the *image theory*, which is given in this section for the point charge and current sources above an infinite ground plane. In general, the image theory may be applied not only in this case. However, this section considers only this most important application of the image theory.

The boundary-value problem shown in Fig. 2.1a is considered. The electric field intensity caused by a point charge has to be computed in the higher half space, whose lower boundary is the perfectly conducting ground plane located in the (x, y) plane at $z = 0$. The point charge q is located at the point $\mathbf{r} = (x, y, z)$. We consider a free-space problem, where the ground plane is

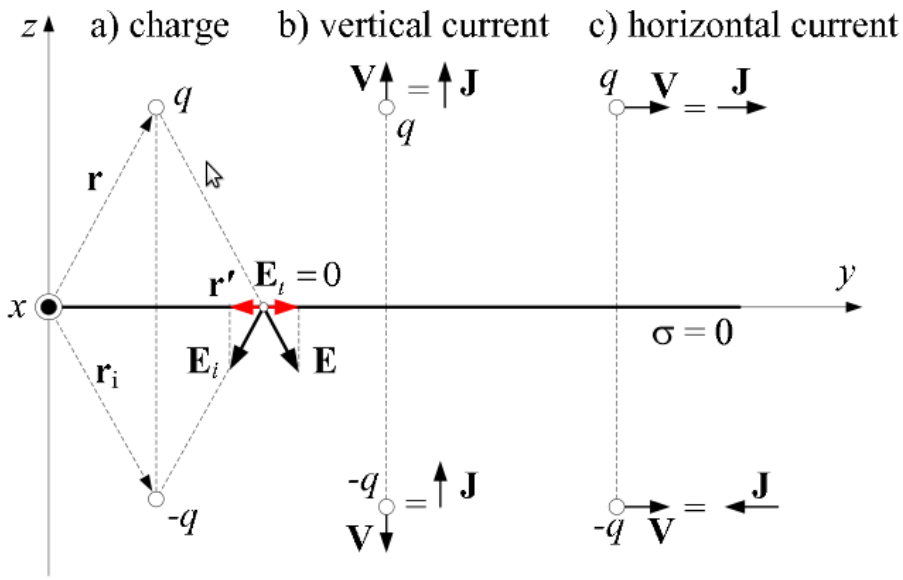

Figure 2.1: Imaged sources for charges (a), and for vertical (b) and horizontal (c) currents.

replaced by an *image charge* $q_i = -q$ located at the point $\mathbf{r}_i = (x, y, -z)$. We consider the tangential component of the electric field intensity produced by q and q_i at the point $\mathbf{r}' = (x', y', 0)$ of the boundary surface. As shown in Fig. 2.1a, $E_t(\mathbf{r}) = 0$ at all points of the boundary. Thus, the solution of the free-space problem satisfies the boundary condition for the tangential component of the electric field intensity and, certainly, to the wave equation. Because of the uniqueness theorem, the solution of this equivalent free-space problem is the unique solution for the initial boundary-value problem.

The second boundary-value problem is shown in Fig. 2.1b. The charge q moves in the vertical direction that may be considered as a point current source $\mathbf{J}(\mathbf{r})$. According to Fig. 2.1a, the equivalent free-space problem is obtained replacing the ground plane by the image charge $q_i = -q$ moving in the negative vertical direction, which means a current in the same direction as $\mathbf{J}(\mathbf{r})$.

The third boundary-value problem is shown in Fig. 2.1c. The charge q moves in the horizontal direction that may be considered as a point current source $\mathbf{J}(\mathbf{r})$. According to Fig. 2.1a, the equivalent free-space problem is obtained replacing the ground plane by the image charge $q_i = -q$ moving in the same direction, which means a current in the opposite direction (see Fig. 2.1c).

These three auxiliary boundary-value problems allow one to deduce the

image principle. The field produced by a system of currents and charges in the proximity of a ground plane may be computed using an equivalent free-space problem, which replaces the ground plane by the mirror images of the current and charge sources. The charges and the horizontal components of currents are reflected with a negative sign, while the vertical components of currents are reflected with a positive sign.

2.3 Green's function method

This analytic technique was developed for the solution of a particular problem, namely, Poisson equation by George Green in 1828. The electrodynamic problems are formulated as partial differential equation systems completed with boundary conditions, i.e., it is a *boundary-value problem.*

Nowadays, the Green's function method is the most wide-spread analytic approach for solution of linear boundary-value problems (BVP). The Green's function method is limited only by linear BV problems because it is based on the superposition principle.

In the following, a linear boundary-value problem is written in the operator form:

$$\begin{aligned} \mathscr{L}\{f(\mathbf{r})\} &= e(\mathbf{r}), \\ \mathbf{r} &\in V \subset \mathbb{R}^3, \\ f(\mathbf{r}), e(\mathbf{r}) &\in \mathbb{C} \end{aligned} \tag{2.23}$$

where V is the three-dimensional solution region with the closed boundary $S = \partial V$, $f(\mathbf{r})$ is the unknown function, $e(\mathbf{r})$ is the known excitation function, and $\mathscr{L}\{\}$ is the linear differential operator. Since the solution of (2.23) is not unique, we complete it with Dirichlet, Neumann or Robin boundary conditions:

- Dirichlet boundary condition $f(\mathbf{r}) = \alpha(\mathbf{r})$,
- Neumann boundary condition $\dfrac{\partial}{\partial n} f(\mathbf{r}) = \beta(\mathbf{r}), \qquad \mathbf{r} \in S$,
- Robin (or mixed) boundary condition $f(\mathbf{r}) + \gamma(\mathbf{r}) \dfrac{\partial}{\partial n} f(\mathbf{r}) = \xi(\mathbf{r})$

The Green's function method gives the solution of the BVP (2.23) in the form of a space convolution integral over the solution region V :

$$f(\mathbf{r}) = -\iiint_V g(\mathbf{r}, \mathbf{r}') e(\mathbf{r}') dV' \tag{2.24}$$

where dV' means the integration over r'. $g(\mathbf{r}, \mathbf{r}')$ is named the Green's function for the BVP, $\mathbf{r}$ and $\mathbf{r}'$ are the *observation* and the *source* points, respectively. The excitation $e(\mathbf{r})$ may be represented using the three-dimensional Dirac delta function $\delta(\mathbf{r} - \mathbf{r}')$:

$$e(\mathbf{r}) = \iiint\limits_V \delta(\mathbf{r} - \mathbf{r}')e(\mathbf{r}')dV' \tag{2.25}$$

The definition for the Green's function is derived by the substitution of (2.24) and (2.25) in (2.23). In view that $\mathscr{L}\{\}$ is a linear operator with respect to $\mathbf{r}$, we write:

$$-\iiint\limits_V \mathscr{L}\left\{g(\mathbf{r}, \mathbf{r}')\right\} e(\mathbf{r}')dV' = \iiint\limits_V \delta(\mathbf{r} - \mathbf{r}')e(\mathbf{r}')dV' \tag{2.26}$$

The comparison of the right- and left-hand sides of (2.26) results in

$$\mathscr{L}\left\{g(\mathbf{r}, \mathbf{r}')\right\} = -\delta(\mathbf{r} - \mathbf{r}') \tag{2.27}$$

Thus, the Green's function is the solution of the BVP at the observation point excited by the minus Dirac delta function at the source point.

Green's functions for wave equations in free space

The most wide-spread application of the Green's function method in electrodynamics is the solution of the scalar wave equation for the free space. The free space is defined as the homogeneous isotropic unlimited space with $\varepsilon = \varepsilon_0$ and $\mu = \mu_0$. The Green's function may be derived as the solution of the wave equation for the scalar electric potential excited by $-\delta(\mathbf{r} - \mathbf{r}')$:

$$\nabla^2 g(\mathbf{r}, \mathbf{r}') + k^2 g(\mathbf{r}, \mathbf{r}') = -\delta(\mathbf{r} - \mathbf{r}') \tag{2.28}$$

Assuming the source point at the coordinate origin and in view of the spherical symmetry, (2.28) may be rewritten in the spherical coordinates $\{\hat{\mathbf{r}}, \hat{\theta}, \hat{\varphi}\}$ as follows:

$$\frac{1}{r^2}\frac{\partial}{\partial r}\left(r^2 \frac{\partial}{\partial r} g(r)\right) + k^2 g(r) = -\delta(r) \tag{2.29}$$

(2.29) is a linear ordinary differential equation (ODE) of the second order, whose solution may be expanded in two independent functions. The functions $\frac{e^{\pm jkr}}{r}$ with $k = \omega\sqrt{\mu_0\varepsilon_0}$ satisfy the homogeneous equation (2.29) and, thus,

compose the basis for the solution subspace of (2.29) in the functional space. Hence, the solution of (2.29) may be expressed via these two functions:

$$g(r) = A\frac{e^{-jkr}}{r} + B\frac{e^{jkr}}{r} \tag{2.30}$$

Since the second term in (2.30) does not satisfy the Sommerfeld radiation boundary condition, the coefficient B has to be zero. The coefficient A may be defined via application to the inhomogeneous differential equation (2.28) the following operator:

$$\lim_{r\to 0}\iiint_V \nabla\cdot\nabla g(\mathbf{r})dV + k^2\lim_{r\to 0}\iiint_V g(\mathbf{r})dV = -\lim_{r\to 0}\iiint_V \delta(\mathbf{r})dV \tag{2.31}$$

where the volume V is a sphere with a radius r about the coordinate origin. The first term on the left-hand side is

$$\lim_{r\to 0}\iiint_V \nabla\cdot\nabla g(\mathbf{r})dV = \lim_{r\to 0}\oint_{A=\partial V} \nabla g(\mathbf{r})dA = -4\pi A \tag{2.32}$$

The second term is

$$k^2\lim_{r\to 0}\iiint_V g(\mathbf{r})dV = k^2\lim_{r\to 0}\int_0^r 4\pi r^2 A\frac{e^{-jkr}}{r}dr = 0 \tag{2.33}$$

Since the right-hand side of (2.31) gives -1, the unknown constant A is equal to 4π, and the solution for (2.29) is

$$g(r) = \frac{1}{4\pi}\frac{e^{-jkr}}{r} \tag{2.34}$$

Using (2.34), the *free-space scalar Green's function* for an arbitrary source point is derived as follows:

$$g(\mathbf{r},\mathbf{r}') = \frac{1}{4\pi}\frac{e^{-jk|\mathbf{r}-\mathbf{r}'|}}{\mid \mathbf{r}-\mathbf{r}' \mid} \tag{2.35}$$

The free-space scalar Green's function (2.35) is the fundamental solution for the scalar wave equation (2.28), which is identical to the equations for the scalar electric and vector magnetic potentials. Thus, the potentials may be calculated using the Green's function method (2.24).

Applying $e(\mathbf{r}') = -\rho_v(\mathbf{r}')/\varepsilon_0$, we may compute the scalar electric potential as follows:

$$\varphi(\mathbf{r}) = \frac{1}{\varepsilon_0}\iiint_V g(\mathbf{r},\mathbf{r}')\rho_v(\mathbf{r}')dV' \tag{2.36}$$

In case of the vector magnetic potential, the excitation is $e(\mathbf{r}') = -\mu_0 \mathbf{J}(\mathbf{r}')$. Thus, we obtain the solution in the following form:

$$\mathbf{A}(\mathbf{r}) = \mu_0 \iiint_V g(\mathbf{r}, \mathbf{r}') \mathbf{J}(\mathbf{r}') dV' \tag{2.37}$$

2.4 Computational methods in electrodynamics

The computational methods, which may be applied to solve the partial differential equation (PDE) system describing the boundary-value problem, are classified as analytical, semi-analytical, and numerical.

The analytical techniques allow one to derive a closed-form solution, which may be calculated explicitly with minor computational efforts. Usually, the application of analytical techniques is possible only under strict assumptions and for very simple structures. As an example of analytical techniques, one can consider the separation of variables that gives the closed-form solutions for some particular problems.

The pure numerical methods (*differential methods*) involve no analytical solutions for electromagnetic problems, instead, the volume is divided into a number of grid cells that allows one to approximate the PDE at local cell volumes. The differential methods lead to a large number of algebraic equations for three-dimensional problems. However, they may be simply applied to the simulation of problems in anisotropic, non-uniform and non-linear media, which is possible if assuming the medium isotropic, uniform and piecewise linear locally at discretization cells.

The semi-analytical methods provide an implicit analytical solution for the initial boundary-value problem that can be solved numerically involving a significantly lower number of unknowns as compared to differential methods. The most significant family of semi-analytical methods in electrodynamics are based on the numerical solutions of integral equations derived from Maxwell's equations. These methods are referenced as *integral equation techniques*. For example, the most common integral equations are the electric-field integral equation (EFIE) and the mixed-potential integral equation (MPIE), whose numerical solutions may be achieved by the method of moments (MoM) and the partial element equivalent circuit method (PEEC), respectively. As the PEEC method is concerned, it will be thoroughly explained and developed in Chapter 5.

2.4.1 Weighted residual method

Since the two aforementioned methods as well as some other methods are based on the weighted residual method, their fundamentals are introduced here.

The method of weighted residuals is an important fundamental mathematical technique used for the approximate solution of boundary-value problems written in the canonical linear operator form. As partial differential and integral equations of classical electrodynamics can be represented in this form, the majority of computational methods apply the principles of the weighted residual method. The Finite Element method (FEM), boundary element method (BEM), method of moments, and the PEEC method are derived from the method of weighted residuals.

Let the boundary-value problem be formulated in a linear-operator form as in (2.23):

$$\begin{aligned} \mathscr{L}\{f(x)\} &= g(x) \qquad x \in V \\ f(x) = \alpha(x), \quad \frac{\partial}{\partial n} f(x) &= \beta(x) \qquad x \in \partial V \end{aligned} \tag{2.38}$$

where V is the solution region, $\alpha(x)$ and $\beta(x)$ are Dirichlet and Neumann boundary conditions. The method of weighted residuals proposes the following approximated solution of (2.38):

$$\tilde{f}(x) = \sum_{k=1}^{N} a_k b_k(x) \tag{2.39}$$

where $b_k(x)$ and a_k are called *basis functions* and *expansion coefficients*, respectively. The choice of the predefined basis functions governs the modification of the weighted residual method. The expansion coefficients are unknown. Thus, the numerical solution is obtained if the expansion coefficients are calculated. As $\tilde{f}(x)$ has to satisfy the given boundary conditions and to approximate $f(x)$ with a finite precision, the substitution of $\tilde{f}(x)$ in (2.38) results in a residual error in all points of the solution region:

$$R(x) = \mathscr{L}\{\tilde{f}(x)\} - g(x) \tag{2.40}$$

We obtain N algebraic equations through an inner product of $R(x)$ and N *weighting functions*:

$$\langle w_m(x), R(x) \rangle_V = 0 \qquad m \in 1, N \tag{2.41}$$

Equation (2.41) demands that the weighted summary residual error of the approximation is equal to zero. The substitution of (2.39) in (2.41) results in the general formulation of the method:

$$\sum_{k=1}^{N} a_k \langle w_m(x), \mathscr{L}\{b_k(x)\}\rangle_V = \langle w_m(x), g(x)\rangle_V \qquad m \in 1, N \tag{2.42}$$

Since the inner products of known functions in (2.42) result in scalar values, (2.42) yields an algebraic equation system with respect to the unknown expansion coefficients.

Because (2.42) applies inner products of functions, the both basis and weighting functions belong to a functional space with an inner product defined as follows:

$$\langle w(x), b(x)\rangle_V = \int_V w(x)b(x)dx \tag{2.43}$$

The weighted residual method has several important modifications related to the weighting and basis functions. The method of weighted residuals with the same basis and weighting functions is called the *Galerkin's approach*. The Galerkin's approach is considered here with regard to the PEEC method (Chapter 5), which can be derived purely on its base.

Chapter 3

Evaluation of Flexible Rogowski Coil Performances in Power Frequency Applications

3.1 Introduction

Rogowski coils have been used for the detection and measurement of time-varying electric currents for decades. They operate on a simple principle: an air-cored coil is placed in a toroidal fashion around the conductor (the primary circuit), whose current has to be measured. The magnetic field produced by the current induces a voltage across the coil, which is proportional to the rate of change of the current.

In 1887, Professor Chattock of Bristol University used a long, flexible coil of wire as a magnetic potentiometer and made magnetic reluctance measurements in iron circuits to investigate "the more satisfactory designing of dynamos". The coils were calibrated by bringing their ends together around an electric current. A recent use of the Chattock potentiometer was developed by the CEGB (Central Electricity Generating Board) for testing the stator cores of generators and motors. Rogowski and Steinhaus also described the technique in 1912. They were interested in measuring magnetic potentials. They describe a large number of ingenious experiments to test that their coil was providing reliable measurements.

In most cases, Rogowski coils have been made by placing the winding on a long, flexible former and then bending it round the conductor, but coils wound on rigid toroidal formers have also been used. The current measurement range is very wide from a few mA to over 1 MA.

The advantages of this type of transducer are immediately clear:

⇒ galvanic separation of the measuring system from the primary circuit;

⇒ non-saturation and good linearity, due to the absence of magnetic material (the probe is air-cored);

⇒ very wide bandwidth extending typically from 50 Hz to about 1 GHz. This enables the transducer to measure and reproduce the waveform of very rapidly transient currents;

⇒ simple circuitry and low price;

⇒ ease of installation.

The disadvantages are:

√ poor sensitivity at low frequencies;

√ problems of interference due to external electromagnetic fields;

√ output influenced by the arrangement of the power circuit.

3.2 Lumped Parameter Model and Frequency Response

The behaviour of the Rogowski coil can be represented by the lumped parameter equivalent circuit in Fig. 3.1:

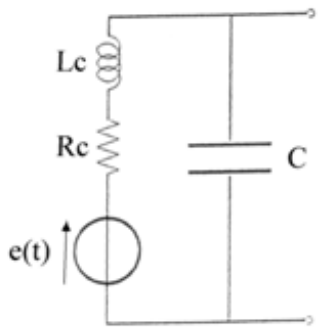

Figure 3.1: Rogowski coil equivalent circuit.

where:
$e(t)$: electromotive force induced in the coil;
R_c: series resistance;

L_c: series auto-inductance;
C: capacitance, which represents leakage capacitances between turns and between the coil and the external environment. This term plays its influence at very high frequency, so it is negligible in quasi-stationary conditions.

The model can be completed including the load R_m and the termination resistance R_k, which is designed to avoid reflection phenomena (Fig. 3.2):

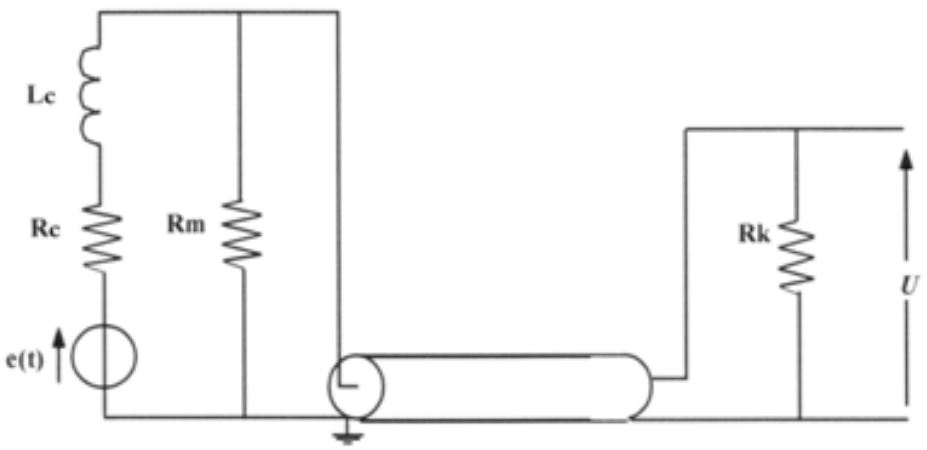

Figure 3.2: Measuring system equivalent circuit.

The model is described by the following equation:

$$e(t) = -M\frac{di}{dt} = L_c\frac{di_c}{dt} + Ri_c \tag{3.1}$$
$$R_b = \frac{R_k R_m}{R_k + R_m} \quad R = R_c + R_b$$

where:
M: is the mutual inductance between the coil and the primary conductor;
i: is the current to be measured;
i_c: is the current flowing in the coil.

The previous equation (3.1) can be rewritten in terms of Fourier transform, where $I(j\omega), I_c(j\omega)$ are the Fourier transforms of the currents defined above, as:

$$-j\omega M I(j\omega) = j\omega L_c I_c(j\omega) + R I_c(j\omega) \tag{3.2}$$

If we introduce the time constant of the coil τ_c equal to $\tau_c = \dfrac{L_c}{R}$, the

transfer function $G(j\omega) = \dfrac{I_c(j\omega)}{I(j\omega)}$ is (Fig. 3.3):

$$G(j\omega) = -\frac{M}{L_c}\frac{j\omega\tau_c + \omega^2\tau_c^2}{1+\omega^2\tau_c^2} \tag{3.3}$$

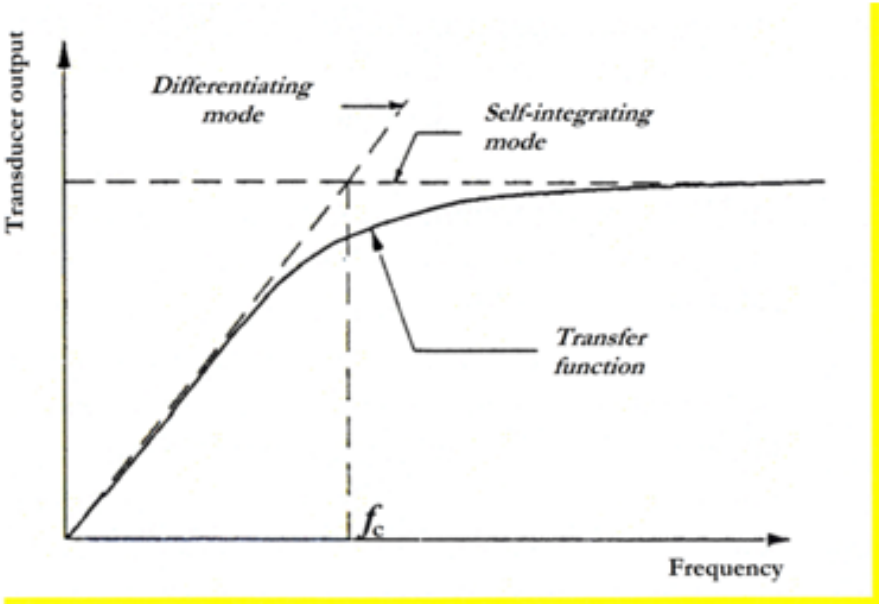

Figure 3.3: Rogowski frequency response.

3.2.1 Differentiating mode

We define as τ the time constant relative to the highest frequency component of the current i

If $\tau \gg \tau_c$ the transfer function becomes:

$$G(j\omega) \simeq -\frac{M}{L_c}j\omega\tau_c \quad \rightarrow i_c \simeq -\frac{M}{R}\frac{di}{dt} \tag{3.4}$$

it means current i varies so slowly that current i_c can be always considered in steady-state condition. This operation is characterized by an upper frequency limit, due to τ_c, so that it is convenient to limit the time constant with an appropriate design (low inductance and high resistance, usually $R_m \rightarrow \infty$). In this case, voltage U is calculated as:

$$U = R_k i_c = -R_k\frac{M}{R}\frac{di}{dt} \simeq -M\frac{di}{dt} \tag{3.5}$$

Disadvantages:

- An analog or digital integration of voltage U is needed to obtain a signal proportional to the measuring current;
- High output voltages, due to the derivative of the current which amplifies the output signal, could cause over-voltages on the measuring system.

3.2.2 Self-integrating mode

If $\tau \ll \tau_c$ the transfer function can be written as:

$$G(j\omega) \simeq -\frac{M}{L_c} \tag{3.6}$$

To operate in integrating mode, it needs to design the probe with a high time constant, that means with a very high inductance and a very small resistance (usually $R_m \ll R_k$). In this case, voltage U is:

$$U = R_m i_c \simeq -R_m \frac{M}{L_c} i \tag{3.7}$$

Advantages:

⋆ Measurement of the high frequency signal is very good;

⋆ No integration process is needed.

Disadvantage:

- Low frequency signals are measured with high distortion.

Unlike current transformers and other ferromagnetic-cored devices, Rogowski coils are linear. There are no effects from saturation and the mutual inductance is independent of the current being measured. The only factor appreciably limiting linearity would be an electrical breakdown in the winding caused by a too high voltage being developed across the ends of the coil.

The integrator is also linear within certain predictable limitations. For reliable operation the designer must be aware of the limitations and design within them. Selection of components and circuit layout are also important in achieving high-integrity measurements.

The main limitations with integrators are saturation, when the output voltage becomes too large and a slew rate limit, which occurs when fast current edges are being measured.

The basic properties of this device (linearity, wide bandwidth, galvanic isolation, lightness and low cost) make it a good alternative to conventional current transducers, such as current transformers (CT) and shunts, and explain the large number of further applications, which include energy management, protection systems, current transformer calibration, current sharing, resistance welding process and measurement of partial discharges and earth resistance of transmission towers [2–7].

3.3 Preliminary Considerations

The uncertainty of the current value measured by RCs can significantly varies, as a function of the coil characteristics and measurement conditions, ranging from some parts in 10^4 to some percent. The RC is a mutual inductor, whose mutual inductance can be easily estimated on the basis of its geometry [4]:

$$M = \mu_0 n A \tag{3.8}$$

where n is the number of turns per meter and A is the cross-sectional area. Equation 3.8 is obtained under the assumption of the following ideal conditions:

- circular coil shape;
- power conductor of infinite length and thin cross-section;
- power conductor placed in the coil centre;
- power conductor orthogonal to the coil plane;
- closed coil with turns uniformly distributed along the circumference;
- absence of any external magnetic field.

These conditions, that can be quite well reproduced in laboratory, are seldom met when commercial coils are used during on-site measurements. As a consequence, a variation of the mutual inductance coefficient can arise, as a function of the coil design characteristics and operating conditions. It becomes then important to investigate the parameters which can affect the measurement results and to predict the accuracy decrease with respect to the reference conditions. Improvement of the RC behaviour and determination of the influence quantity effects, such as presence of external field source, position and path of the current carrying conductor and non-circular coil shape, are often performed experimentally [7–13]. As an alternative, with

reference to RCs for use at power frequency, some modelling approaches have been developed [14–17]. In particular, the influence of the straight power conductor position and the effect of the turn number are investigated in [15]. The presence of a coil terminal gap is taken into account in [16], together with the position of the power conductor. The effect of the non-orthogonal condition between the power conductor and the coil plane is described in [18], but for a current sensor with magnetic core.

To deeply investigate and quantify the effect of the influence quantities on actual RCs, a numerical tool has been developed and applied to the analysis of the differentiate behaviour of RCs under non ideal measurement conditions. The proposed model is able to simulate most of the possible RC non-idealities together with the actual power circuit conditions. It further allows the evaluation of the combined effect of several non-idealities which occur simultaneously. The approach developed is fast enough to be included in a Monte-Carlo procedure for the estimation of the uncertainty associated with the coil use.

The attention is focused on openable and flexible Rogowski coils, which are widely used owing to their ease of installation, despite their lower accuracy and higher temperature sensitivity compared to both the rigid ones and those based on printed circuit board [19]. The study is developed under sinusoidal steady-state condition at power frequency, by modifying both the circuital and coil parameters, such as the power conductor position, shape and path, the presence of an external current, the uniformity of the turn distribution along the coil and the non-circular coil shape. The modelling tool, validated through experimental measurements, also permits the evaluation of those design actions that improve the RC behaviour and its accuracy, such as the addition of a compensation turn or a counter-wound second winding. Taking into account the high number of parameters that can affect the measurement accuracy, their combined effect is conveniently evaluated by a statistical procedure. Two ranges of parameter variations are considered to simulate the on-site operating conditions. In both cases an estimate of the measurement uncertainty is given.

3.4 The Modelling Approach

The RC is essentially a linear mutual inductor, linked with the magnetic field generated by the current $i(t)$, which flows in the power conductor (primary conductor). The electro-motive force $e(t)$ induced in the coil is given by:

$$e(t) = M\frac{di(t)}{dt} \tag{3.9}$$

Under the assumption of an ideal closed coil, wound with a continuous turn distribution (infinite number of turns), with a small cross-sectional area and under no-load electrical operating conditions, the mutual inductance is a constant term. Then, according to the Ampere's law, the linked magnetic flux does not depend on the shape and position of the infinite length primary conductor. Whenever one of the above conditions does not occur, a variation of the mutual inductance coefficient arises.

The developed RC model, based on a 3D quasi-analytical formulation, provides the magnetic flux linking the coil, the mutual inductance coefficient (coil sensitivity) and the electro-motive force induced at the transducer terminals. Under the assumption of coil connected to an impedance of very high value, the current which flows in the winding is negligible, since the presence of displacement currents can be disregarded under low frequency supply. The RC is considered in an open-boundary homogeneous domain. According to these hypotheses, the current $i(t)$ which flows in the filamentary primary conductor produces, in a given point P at the time t, the magnetic vector potential expressed by the well-known relationship:

$$\vec{A}(P,t) = \frac{\mu_0}{4\pi} \int_L \frac{i(t)\, d\vec{l}}{\rho_P} \tag{3.10}$$

where the propagation terms are neglected, μ_0 is the vacuum magnetic permeability, L is the total primary conductor length and ρ_P is the distance between a point of the field source and the point P. The magnetic flux is then given by the line integral of the potential along the winding profile Γ, that is:

$$\Lambda = \int_\Gamma \vec{A}(P,t) \cdot d\vec{\gamma} \tag{3.11}$$

thanks to the divergence-free property of the magnetic flux density and to the Stokes' theorem. Integrals (3.10) and (3.11) are numerically solved by dividing the primary conductor and the coil turns into elements, whose number has been evaluated on the basis of preliminary computations, as explained below.

Since the input and output terminals of an opening coil are usually not coincident, the gap between them is quantified by an opening angle β. In the more general case of an elliptical coil, each point P, which belongs to the toroidal helix made of N turns, is defined by the coordinates (Fig. 3.4):

$$\begin{cases} x = [r \cdot \cos\gamma + S_{max}] \cdot \cos\vartheta \\ y = [r \cdot \cos\gamma + S_{min}] \cdot \sin\vartheta \\ z = r \cdot \sin\gamma \end{cases} \tag{3.12}$$

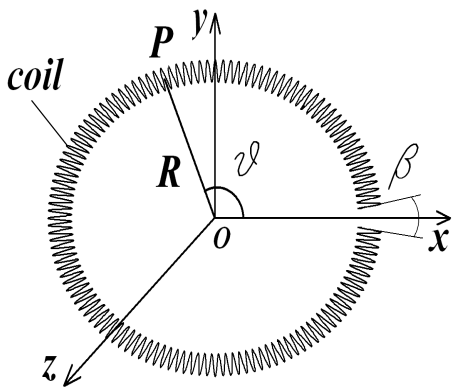

Figure 3.4: Coordinate system assumed in modelling the RC.

where r is the turn radius, γ is the turn angle in the plane R, z ($0 \leq \gamma \leq 2\pi N$), ϑ is the angle in the plane xy whose value is $(((2\pi - \beta)/2\pi N)\gamma + (\beta/2))$; and S_{max}, S_{min} are the maximum and minimum semi-axis, respectively. A RC with circular shape can be described by imposing $S_{max} = S_{min} = R$, where R is the mean radius. In the following computations, the gap β is always centred at $x = S_{max}, y = 0, z = 0$ as shown in Fig. 3.4.

A pitch weight vector is used to describe a non-uniform turn distribution. The element w_i of the vector is associated with the pitch of the ith turn: according to its value, the turn pitch can be enlarged ($w_i > 1$) or reduced ($w_i < 1$), with the constraint $\sum_{i=1}^{N} w_i = N$.

The relation (3.12) can be generalized to the description of RCs fitted by a compensation turn or a counter-wound compensation winding.

The model simulates the effects of bulk primary conductors with different cross-section shapes (circular and rectangular), by representing them with suitable distributions of filamentary wires. The skin effect can be taken into account by assigning proper current values to the wires.

The path of the power circuit is handled by dividing it into straight or curvilinear segments in order to reproduce any configuration, as for example, straight [Fig. 3.5(a)], L-type [Fig. 3.5(b)] or turn [Fig. 3.5(c)] conductors.

In order to define a reliable number of elements in the discretization process, the results obtained with the 3D model are tested by comparing the flux values computed by a Finite Element Method (FEM) model. The 2D FEM model is based on a magnetic vector potential weak formulation, which uses a meshing technique with triangular elements and first order shape functions. These calculations are performed by referring to a circular primary conductor in centred position and a Rogowski coil with the following dimensions:

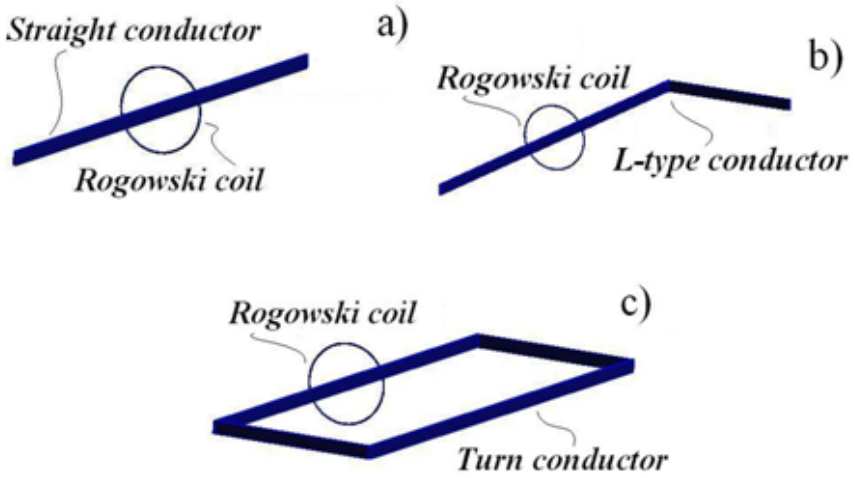

Figure 3.5: Simulated power circuit paths: (a) straight; (b) L-type; and (c) turn conductors.

number of turns N=130, external coil radius R_e=175 mm, internal coil radius R_i=150 mm, coil winding diameter d=2 mm. Under this geometrical hypothesis, the flux linked with the coil can be analytically computed as well. Table 3.1 shows the results obtained by the methods described above. The number of elements is increased progressively until the flux values match better the comparing model results. In the end, the residual deviation may be explained taking into account that a continuous turn distribution is considered in FEM and analytical calculations, whereas in the 3D analysis the magnetic flux is linked with the actual coil helix.

Table 3.1: 3D, 2D and closed-form preliminary computations

Model	**Linked magnetic flux (nWb)**
3D Biot-Savart	78.647
FEM	78.213
Closed-form	78.214

The modelling analysis allows the prediction of the RC behaviour as a function of the following power circuit parameters:

- position of the primary conductor with respect to the coil center;
- shape of the primary conductor cross-section;

- path of the power circuit;
- tilt angle α of the primary conductor with respect to the coil plane.

Moreover, the following coil parameters can be set:

- opening angle β;
- coil eccentricity;
- non-uniform distribution of the turns along the coil;
- presence of a compensation turn or a counter-wound winding.

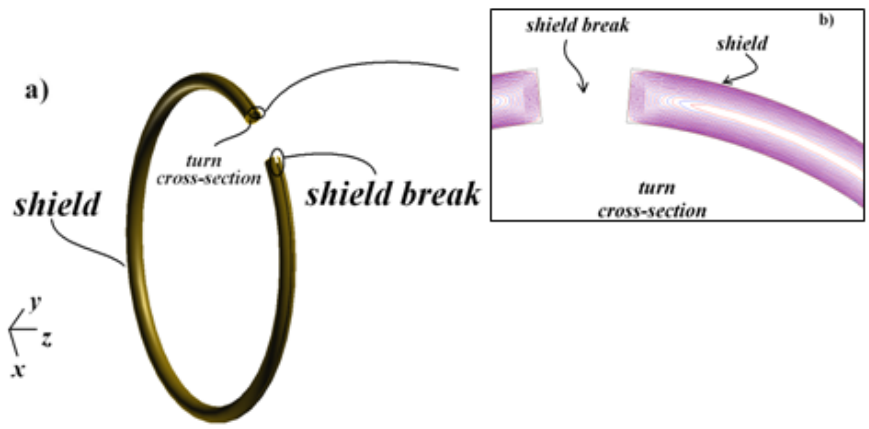

Figure 3.6: (a) Sketch of the open shield geometry. (b) Current density lines induced in an open shield surrounding the turn cross-section.

Actual Rogowski coils are generally shielded by an open metallic screen [3], [20], whose induced eddy currents could modify the magnetic field distribution. The evaluation of this perturbation is obtained through a finite element model, based on a two dimensional flux driven T-Ω formulation [21], which provides the induced current density in the shield (Fig. 3.6). The computations are carried out in the R, z plane by imposing a sinusoidal magnetic flux through the turn cross-section. The shield is modeled as a hollow toroid of circular cross-section (r = 3.6 mm), with 1 mm thickness and $30 \cdot 10^6$ S/m electrical conductivity (aluminium shield), as shown in Fig. 3.6. Figure 3.7 presents the time behaviour of the magnetic flux through the turn cross-section, computed with a closed shield, an open shield (shield break=10°) and without the shield. The flux values Λ are normalized to the flux peak value without the shield Λ_0. An amplitude variation of 0.3% with a phase

shift of about 4° is detected in presence of a closed shield with respect to the unperturbed behaviour. When the shield is open, the magnetic flux variation lowers to a few parts in 10^5. As a result of this analysis, the presence of the open shield is disregarded and (3.10) and (3.11) can be then used.

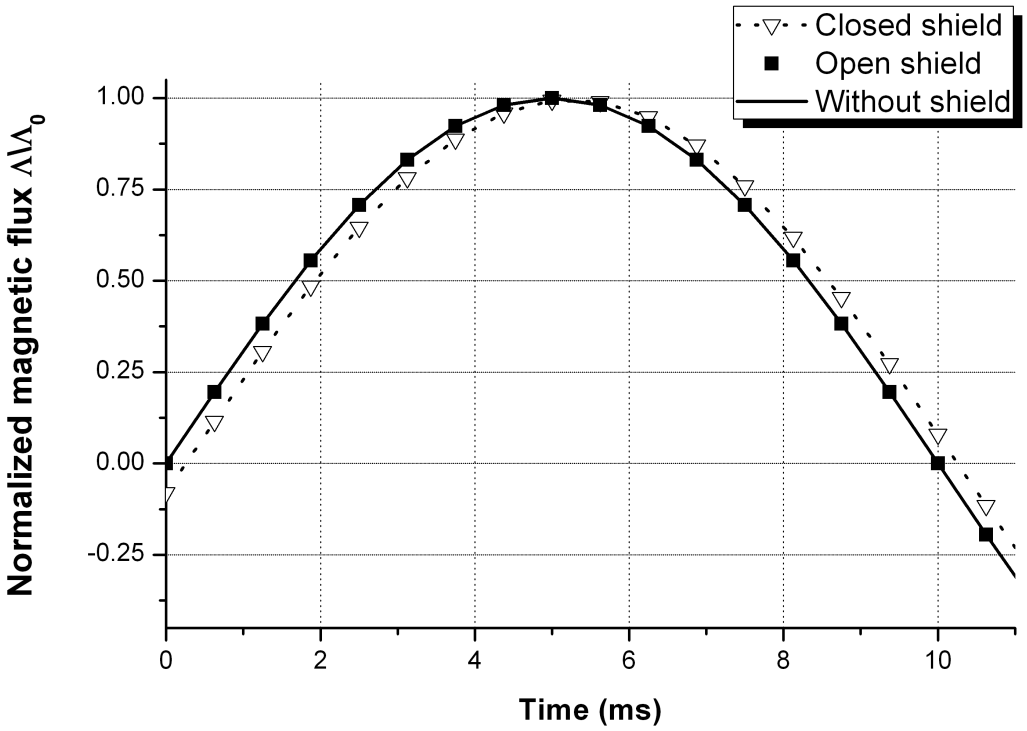

Figure 3.7: Normalized magnetic flux through the turn cross-section, with closed shield, open shield, and without shield.

3.5 Experimental Validation

The validation of the model is carried out by comparing computational and measurement results, under sinusoidal supply at power frequency. The investigation is performed on a commercial flexible Rogowski coil, in the high current laboratory of the Istituto Nazionale di Ricerca Metrologica of Torino (INRIM). The dimensions of the RC and the power conductors are given in Table 3.2. To ensure a good positioning accuracy, a plexiglass disc is employed to support the RC and hold the primary conductor in the stated positions (Fig. 3.8).

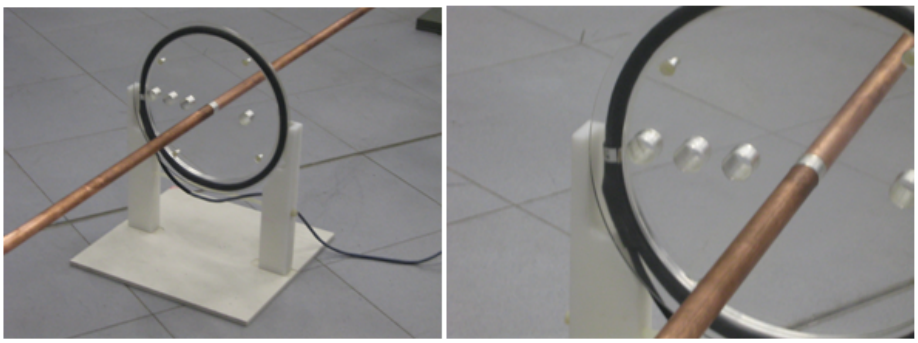

Figure 3.8: Plexiglass disc support for the RC and circular primary conductor.

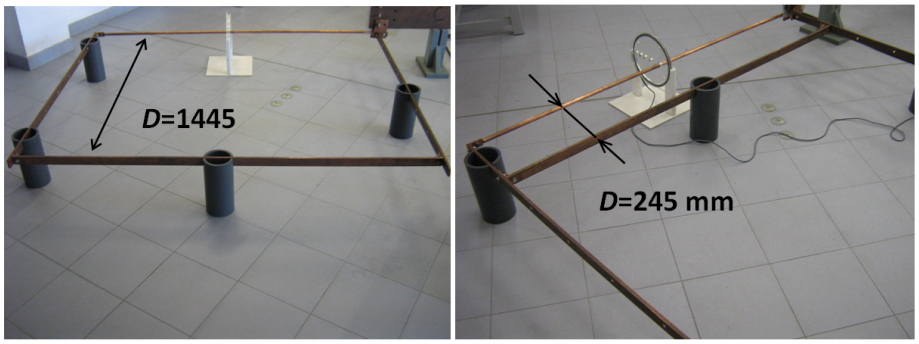

Figure 3.9: RC arrangement with respect to the primary and return conductors.

The current return is made with bar conductors, whose distance D from the primary conductor can be changed (Fig. 3.9). The RC mutual inductance M is evaluated as ratio of the linked flux to the current value. The current is measured by a reference CT and the flux is obtained through integration of the voltage induced across the RC, performed by the associated integrator. A Y-bar system (Fig. 3.10), usually employed when performing calibrations,

Table 3.2: Rogowski coil and conductor dimensions

Primary conductor diameter	18 mm
Primary conductor length	1800 mm
Bar conductor dimensions	10 mm x 40 mm
RC mean diameter	245 mm

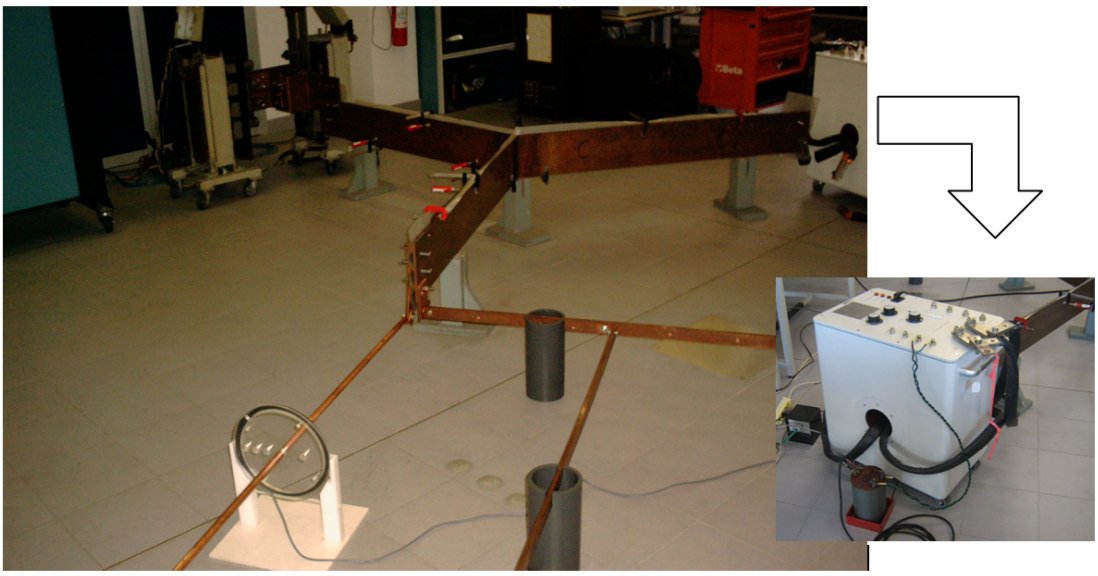

Figure 3.10: Y-bar system, reference current transformer, and RC arrangement.

allows minimization of stray magnetic fields and symmetric positioning of the supply, reference CT and device arrangement.

The scheme of the experimental set-up is shown in Fig. 3.11.

The computed and measurement results are expressed in terms of the mutual inductance M normalized to the value M_0, obtained under reference conditions, that is when the primary conductor is centred, its axis is orthogonal to the coil plane and the return conductor is far from the device ($D \geq 1445$ mm). It must be underlined that M_0 does not refer to the ideal conditions, which imply an infinite primary conductor and can be well approximated when the conductor total length overcomes $\sim 50 \cdot R$.

The integrator associated with the coil is calibrated by applying reference sinusoidal voltages, to verify its linearity and stability. From the results obtained, a standard uncertainty contribution of $2.5 \cdot 10^{-4}$ is attributed to the integrator. The uncertainty associated with the M/M_0 measurement values ($7 \cdot 10^{-4}$, confidence level 95%) is estimated by considering, besides the contribution of the integrator, that due to the coil positioning on the support.

Since the turn number of the commercial RC is not accurately known, some computations are performed by increasing N from 130 to 3000. The results show that N does not appreciably affect the value of M/M_0, provided

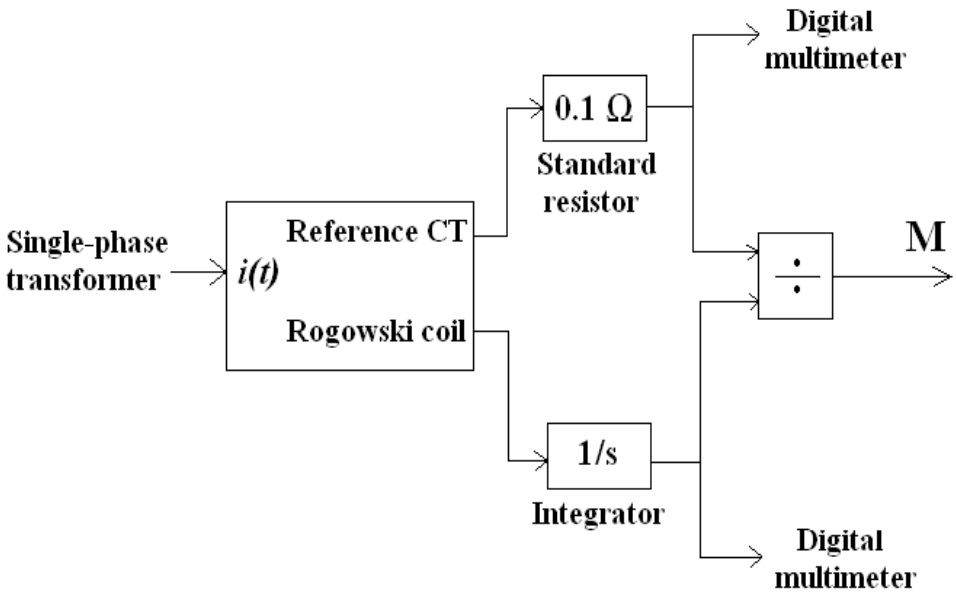

Figure 3.11: Scheme of the experimental setup.

that all the other coil parameters are unvaried. Thus, a coil with 130 turns is used to reduce the computational time. Table 3.3 summarizes the main features of the model used to simulate the Rogowski coil.

Table 3.3: Model parameters

RC Mean radius R	122.5 mm
RC turn cross-section diameter	7 mm
Number of turns N	130
Primary conductor length	1800 mm

Figures 3.12 and 3.13 compare measurements and computations, when the position of the primary and return conductors are varied, respectively.

In Fig. 3.12, the primary conductor is moved along the x axis (Fig. 3.9) and the return conductor is kept 1445 mm distant from the primary conductor. The actual coil opening angle, which can only be estimated, is assumed equal to 0.5°. The maximum relative deviation between model and experimental results is $1.5 \cdot 10^{-3}$, when the primary conductor is very close to the gap ($x_p = 100$ mm). The computation is repeated by slightly increasing the opening angle ($\beta = 0.7°$), in order to determine the sensitivity to the

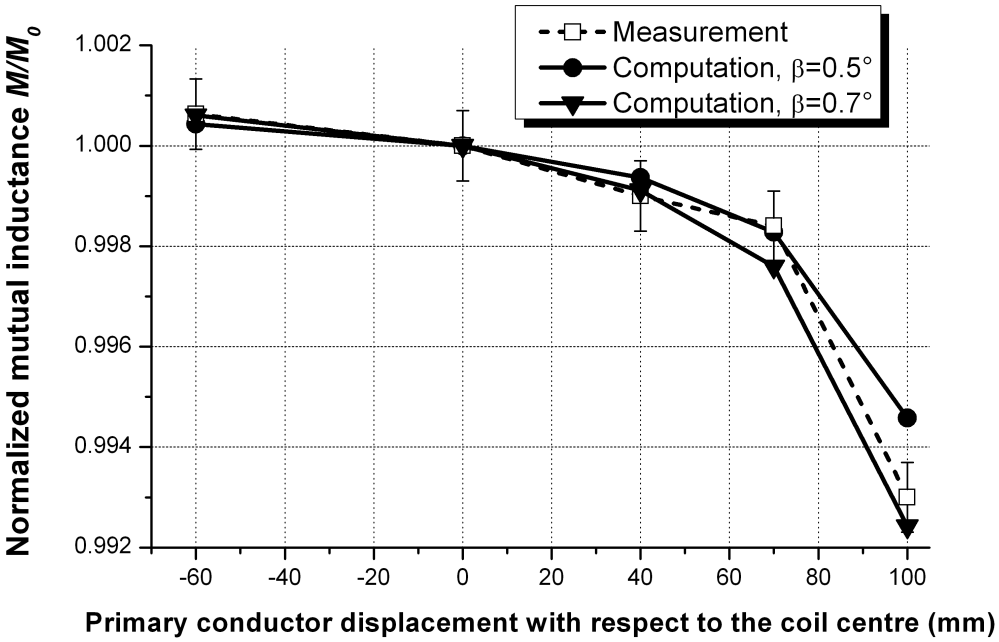

Figure 3.12: Comparison of the measurement and model results versus displacements of the primary conductor from the coil center for two gap angles β.

gap variation. In this case, a measurement-model deviation one order of magnitude lower is found, for the same position of the primary conductor. As shown in Fig. 3.12, all the measurement results fall inside the strip edged by the two modelled cases.

Figure 3.13 shows the influence of the return conductor distance from the coil centre when the primary conductor is placed in two positions ($x_p = 70$ mm, $x_p = -60$ mm), with $\beta = 0.5°$.

The obtained results show an agreement between measurement and computation generally better than the part per thousand and make the use of the numerical model feasible for an exhaustive analysis of the RC behaviour.

3.6 Influence of Coil and Circuital Parameters

The analysis is carried out by simulating the RC, whose characteristics are summarized in Table 3.3.

First, the effect of the primary conductor position on the mutual inductance is investigated by assuming angle β as a parameter.

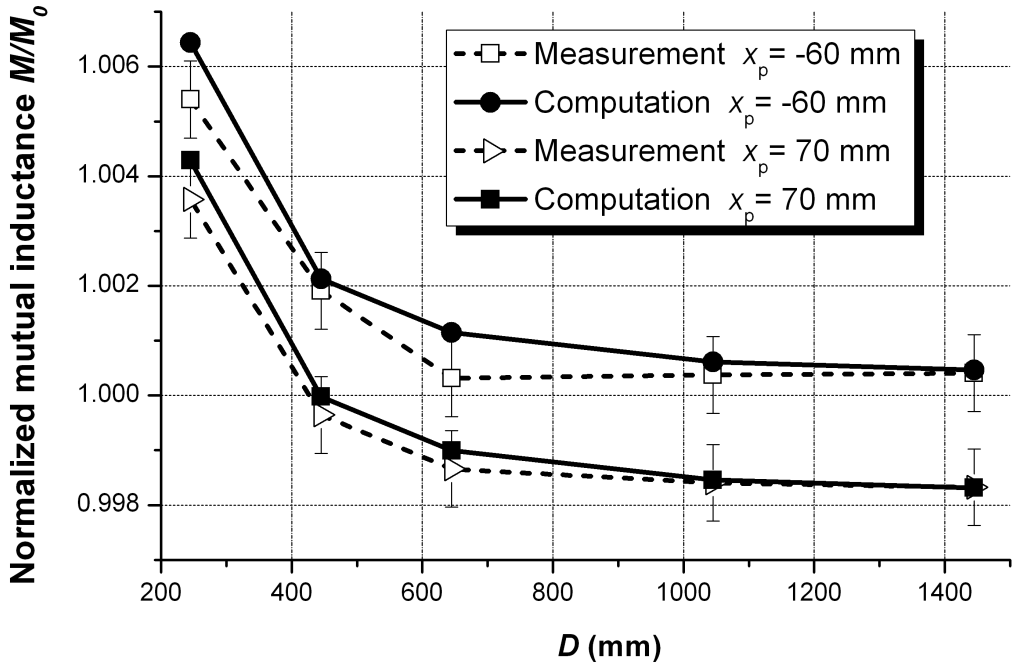

Figure 3.13: Comparison of the measurement and model results as a function of the return conductor position. The displacement of the primary conductor is indicated as a parameter.

The results are shown in Fig. 3.14, where the conductor is moved along the x axis from the coil centre up to 80% of the mean coil radius R. The values shown can be referred to any coil radius R.

As shown in Fig. 3.14, when the primary conductor is close to the coil gap, the mutual inductance decreases significantly with respect to M_0, even for small angles β. To limit this effect, the turns close to the coil terminals are concentrated by decreasing their pitch (Fig. 3.15). The results in Table 3.4 show that, for the primary conductor position $x_p/R = 0.8$, the deviation of M/M_0 from unit can be strongly lowered through a suitable choice of the number m of turns with reduced pitch weight ($w_i = 0.9$). For larger β, m has to be increased or the weight w_i must be decreased. As an indication, an approximated rule to optimize the compensation is given by:

$$\frac{2\pi}{N}\sum_{i=1}^{m}(1 - w_i) \simeq \beta \tag{3.13}$$

This relation is derived by imposing that the linked magnetic flux lost in

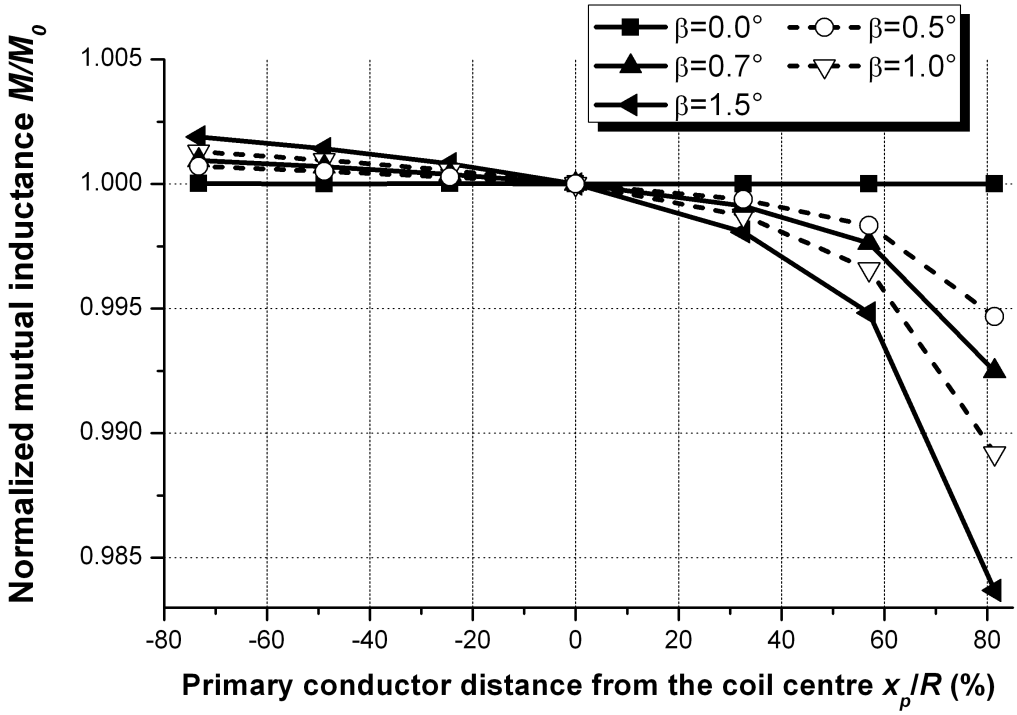

Figure 3.14: Normalized mutual inductance versus primary conductor position from the coil center, for gap angles β from 0° to 1.5°.

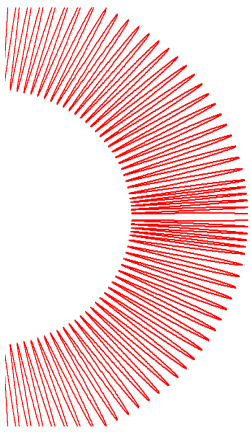

Figure 3.15: Sketch of a non-uniform turn distribution along the coil.

the gap is compensated by the compression of the m turns. It can be noted that the results shown in Table 3.4 agree with (3.13).

In actual situations, the requirement of orthogonal condition between coil plane and primary conductor cannot always be fulfilled. For this reason, the effect of a coil tilt angle α is investigated for different values of the gap β and turn number N. In the present analysis, the primary conductor lays in the y, z plane and is rotated around the x-axis (Fig. 3.4), in centred position. The tilt angle ranges from 80° to 100° with respect to the coil plane (orthogonal condition: $\alpha = 90°$). The Figure 3.16 compares the deviations of the mutual inductance versus α for $\beta = 1°$ computed with 130, 500 and 1000 turns. The results show that the behaviours are almost anti-symmetric with respect to $\alpha = 90°$ and strongly depend on the turn number. To better understand this phenomenon, some considerations are detailed in the Appendix. It must be observed that if the computation is repeated for $\beta = 0°$ (closed coil), the considered tilt α gives rise, for the considered case, to deviations which are at least one order of magnitude lower than those found with $\beta = 1°$.

The tilt effect may be considerably reduced by adding a counter-wound winding or a counter-wound single-turn. This solution, generally adopted to mitigate possible external magnetic fields with components along the coil axis (z-axis), gives advantages also in non-orthogonal conditions. By adding a counter-wound winding with the same turn number as the main coil (Fig. 3.17a), the mutual inductance deviation reduces to less than $2 \cdot 10^{-4}$, even in the worst case ($N = 130$, $\alpha = 100°$). A counter-wound single-turn, instead of a second winding (Fig. 3.17b), leads to a $8 \cdot 10^{-4}$ relative deviation for the same worst case.

All the issues previously discussed concern a primary conductor of circular shape, but in power plants busbars are frequently used. Then, the influence on the mutual inductance of the cross-section dimensions of the

Table 3.4: Mutual inductance relative deviation with uniform and non-uniform optimized turn distributions ($N = 130$)

	Uniform distribution (10^{-2})	**Non-uniform distribution** (10^{-2})
$\beta = 0.5°$	-0.53	0.05 ($m = 2$)
$\beta = 0.7°$	-0.75	0.10 ($m = 3$)
$\beta = 1.0°$	-1.08	0.03 ($m = 4$)
$\beta = 1.5°$	-1.63	-0.10 ($m = 6$)

primary conductor is investigated with respect to the coil radius. To this end, a rectangular conductor with dimensions $h = 10$ mm and $d = 40$ mm is

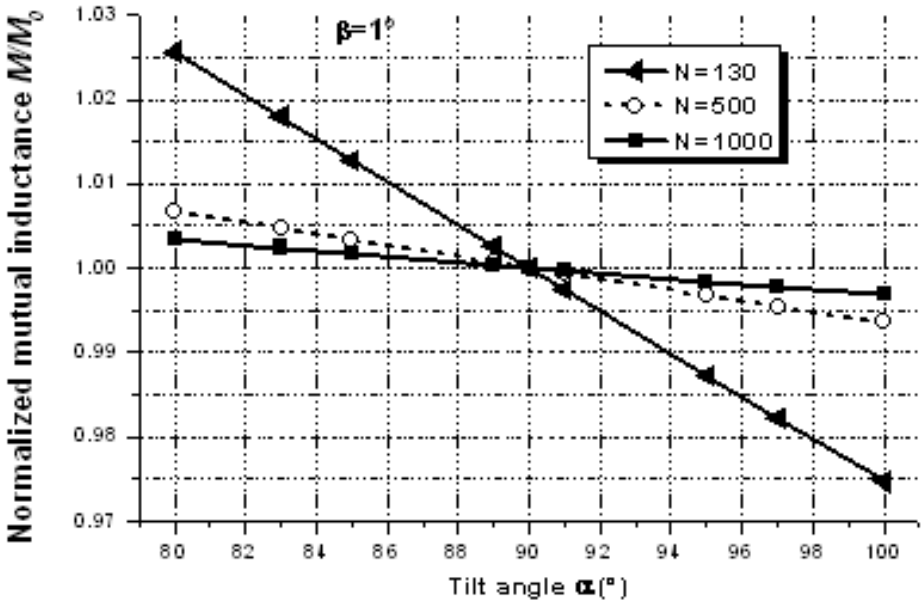

Figure 3.16: Effect of non-orthogonal condition between the RC plane and the primary conductor. The mutual inductance values are shown versus angle α for increasing number N of turns ($\beta = 1°$).

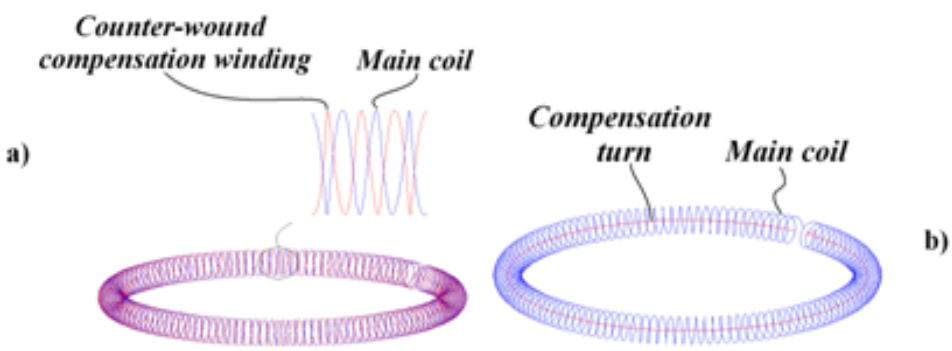

Figure 3.17: Sketch of (a) a second winding counter-wound with the same turns as the main coil and (b) a counter-wound single-turn.

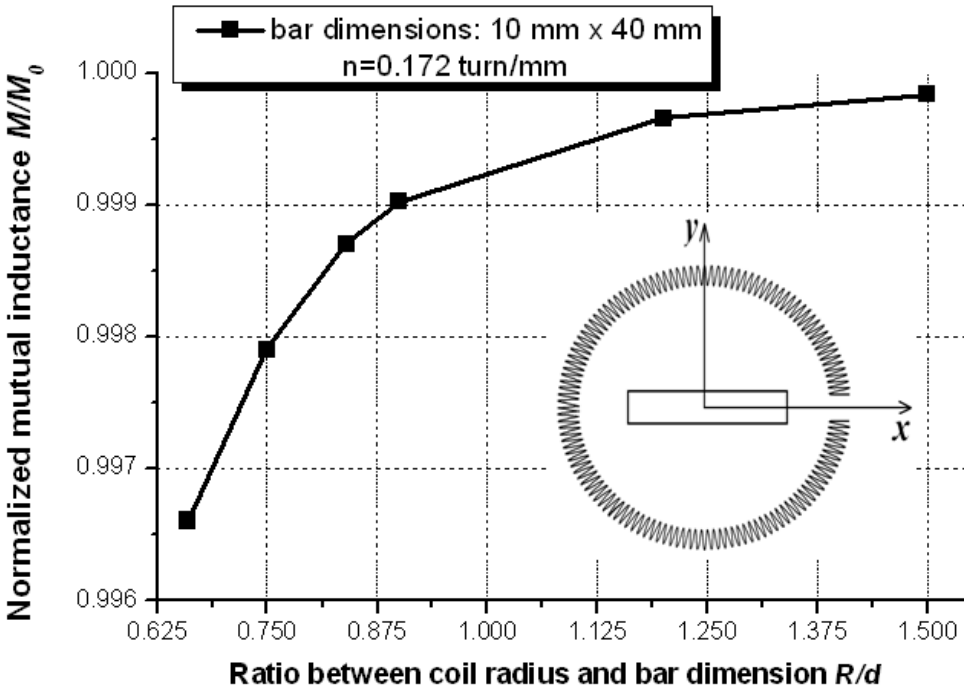

Figure 3.18: Normalized mutual inductance versus the ratio of coil radius to bar dimension.

centred at O with the major dimension along the x-axis. A 1 mm coil gap is assumed with a turn density $n = 0.172$ turn/mm (Fig. 3.18). The mutual inductance computed with the filamentary primary conductor is considered as the reference value M_0. As far as the major bar dimension is sufficiently smaller than the coil radius ($R > 1.5d$), the deviation of the mutual inductance from the reference value is negligible. If the bar conductor has the major dimension d along the y-axis, the deviation is reduced to about $6 \cdot 10^{-4}$ when $R = 0.66d$.

3.7 Estimate of the On-site Measurement Uncertainty

When using the RC for on-site measurements, the circuit arrangement can significantly differ from the optimal one with reference to both the coil positioning around the primary conductor and the presence of the return con-

Table 3.5: Influence quantity ranges for situation A

Influence quantity	**Range of Variation**	**Reference condition**
Eccentricity	0.0 to 0.4	0.0
Turn pitch weight	0.95 to 1.05	1.0
Δx displacement	(-50 to +50) mm	0 mm
Δy displacement	(-30 to +30) mm	0 mm
Return conductor distance from the coil centre	(1.5 to 20)$\cdot R$	20$\cdot R$
Primary conductor length	(3.1 to 6) m	6 m
Tilt angle α	(70 to 110)°	90°

ductor and/or other field sources. In addition, the measurement conditions strongly vary from site to site and in most cases cannot be accurately determined. This situation can lead to a degradation of the RC performances, since the actual value of the mutual inductance M can be different from the one determined in the reference condition (M_0). However, the high number of parameters, which cannot be well controlled, makes a direct analysis unfeasible and suggests the use of a statistical approach.

An estimate of the measurement uncertainty for an on-site situation can be performed by making use of the model previously described, starting with the identification of the influence parameters and their expected ranges of variation. In the following, examples of uncertainty evaluation are given for rough on-site measurements and better controlled measurement conditions. The flexible and openable RC, whose dimensions are listed in Table 3.3 ($\beta = 0.5°$), is fitted by a counter-wound compensation turn (Fig. 3.17b). The influence quantities and their assumed range of variation are shown in Table 3.5 (situation A), together with the reference condition values. The path of the primary conductor, with circular cross-section, is divided in two parts connected in correspondence of the coil plane: the first one has a 3 m fixed length and the second section can be varied, to simulate the effect of a turn made by the power circuit.

A propagation distribution approach based on Monte Carlo method is used to estimate the mutual inductance M, its standard uncertainty and the

Table 3.6: Influence quantity ranges for situation B

Influence quantity	**Range of Variation**	**Reference condition**
Eccentricity	0.0 to 0.2	0.0
Turn pitch weight	0.99 to 1.01	1.0
Δx displacement	(-5 to +5) mm	0 mm
Δy displacement	(-3 to +3) mm	0 mm
Return conductor distance from the coil centre	(5 to 20)$\cdot R$	20$\cdot R$
Primary conductor length	(4 to 6) m	6 m
Tilt angle α	(88 to 92)°	90°

coverage interval corresponding to a 95% confidence level [22]. The standard uncertainty associated with the input quantities is evaluated by assuming, as a first approach, a rectangular probability distribution of half width equal to the variation range. The number of draws T is fixed to 20000, which is sufficient to ensure statistical stabilized results [22].

A more controlled measurement situation is taken into account by considering the reduced range of variations shown in Table 3.6 (situation B).

Figures 3.19 and 3.20 compare the numerically approximated probability density function and distribution function for the situations A and B, respectively. The difference between the estimated mutual inductances M is quite negligible ($M = 8.1503$ nH for case A and $M = 8.1487$ nH for case B, against a calculated reference value $M_0 = 8.1487$ nH). From the data shown in Fig. 3.19, standard deviations of 0.027 nH and 0.0023 nH are found for situations A and B, respectively. A relative standard uncertainty contribution of some parts per thousand can then be attributed to the measurement arrangement, when the range of variations listed in Table 3.5 can be reasonably assumed. However, in a relative more controlled situation, this contribution becomes quite negligible or at most comparable with that associated to M_0, determined in the calibration phase, provided that measurements are performed not too far from the room temperature.

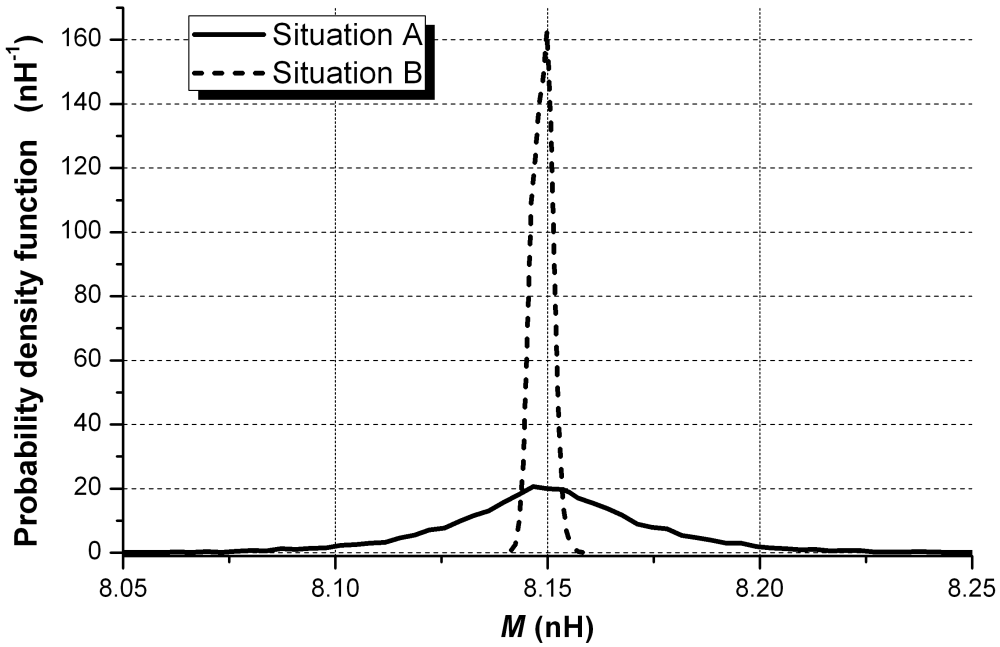

Figure 3.19: Probability density functions for situations A and B.

3.8 Appendix

The analysis of the non-orthogonal condition effects is, in a general case, a quite complicated topic. However, under the assumption that the primary conductor is rotated around the x-axis in the plane y, z (Fig. 3.4) and the turn number N is sufficiently high, some simplified considerations can be developed.

To this end, the RC turn opposite to the coil gap is considered. Under the assumption of square cross-section, this turn is subdivided into four straight segments (I, II, III, IV in Fig. 3.21), with length l. The contribution Λ_t to (3.11), related to the single turn, is expressed as:

$$\Lambda_t = \int_{turn} \vec{A} \cdot d\vec{\gamma} = \int_I \vec{A} \cdot d\vec{\gamma} + \int_{II} \vec{A} \cdot d\vec{\gamma} + \int_{III} \vec{A} \cdot d\vec{\gamma} + \int_{IV} \vec{A} \cdot d\vec{\gamma} \quad (3.14)$$

Figures 3.22a and 3.22b show the relative orientation of the vectors involved in (3.14) for segments I-III and II-IV, respectively, when $\alpha = 90°$ and $\alpha = 90° + \Delta\alpha$ ($\Delta\alpha > 0$). The angle δ is related to the turn pitch, which depends on the turn number N, $A_{90°,i}$ and $A_{90°+\Delta\alpha,i}$ are the average values

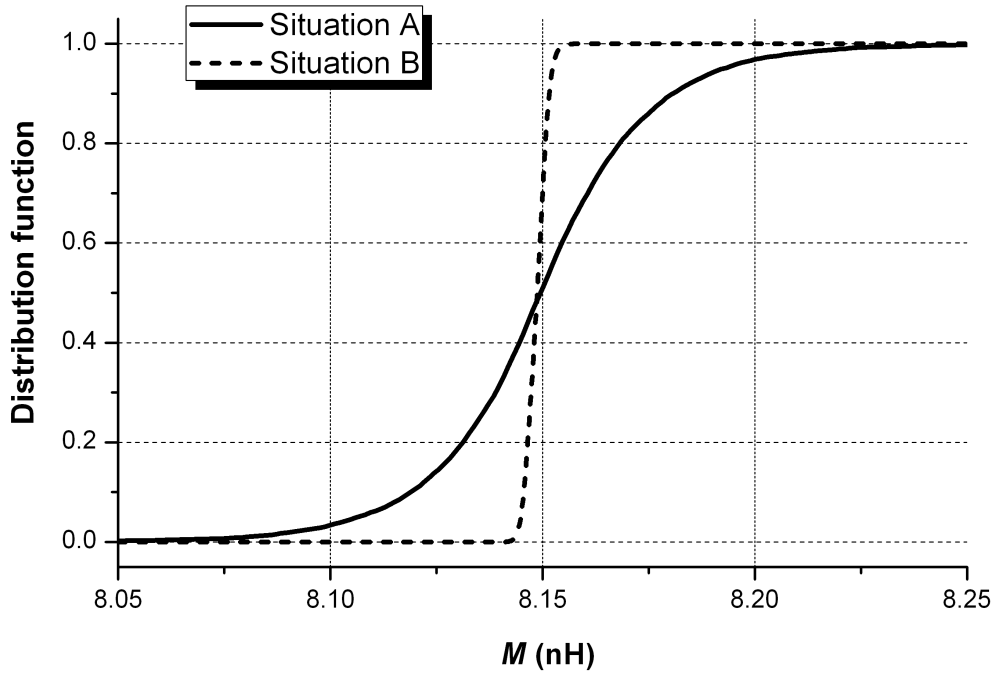

Figure 3.20: Distribution functions for situations A and B.

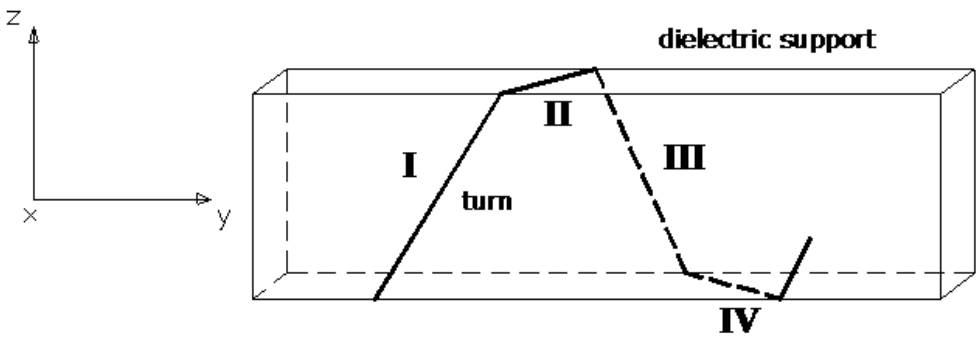

Figure 3.21: Sketch of a square cross-section turn made of four straight segments (I, II, III, and IV).

of the magnetic potential along the segment i (i=I,...,IV).

The flux linked with the single turn when $\alpha = 90°$ is:

$$\Lambda_t = \int_{turn} \vec{A}_{90°} \cdot d\vec{\gamma} = A_{90°,I} l \cos\delta - A_{90°,III} l \cos\delta = l \Delta A \cos\delta \qquad (3.15)$$

where the magnetic potentials in I and III are linked by the expression $A_{*,I} =$

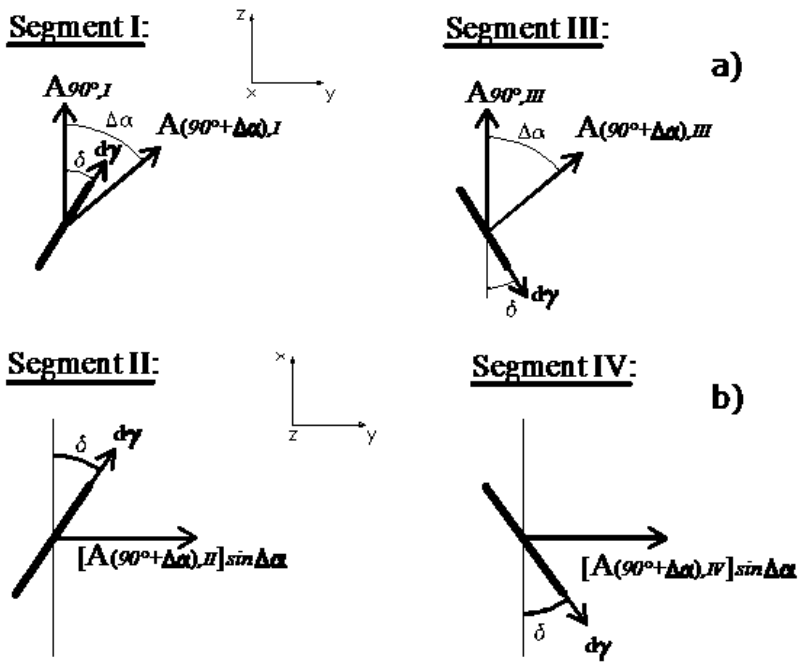

Figure 3.22: Vector orientations involved in the computation of (3.14): (a) Segments I–III. (b) Segments II–IV.

$A_{*,III} + \Delta A$ ($\Delta\alpha > 0$). It should be noted that the integrals along II and IV are null because their paths are perpendicular to the magnetic vector potentials.

When $\alpha = 90° + \Delta\alpha$, the magnetic flux becomes:

$$\Lambda_{t,90°+\Delta\alpha} = \int_{turn} \vec{A}_{90°+\Delta\alpha} \cdot d\vec{\gamma} = l[\Delta A \cos\Delta\alpha \cos\delta + \\ + (2A_{90°+\Delta\alpha,III} + \Delta A)\sin\Delta\alpha \sin\delta + (A_{90°+\Delta\alpha,II} + A_{90°+\Delta\alpha,IV})\sin\Delta\alpha \sin\delta] \tag{3.16}$$

In a similar way, when $\alpha = 90° - \Delta\alpha$ is considered, the magnetic flux is:

$$\Lambda_{t,90°-\Delta\alpha} = \int_{turn} \vec{A}_{90°-\Delta\alpha} \cdot d\vec{\gamma} = l[\Delta A \cos\Delta\alpha \cos\delta + \\ - (2A_{90°-\Delta\alpha,III} + \Delta A)\sin\Delta\alpha \sin\delta - (A_{90°-\Delta\alpha,II} + A_{90°-\Delta\alpha,IV})\sin\Delta\alpha \sin\delta] \tag{3.17}$$

The deviations $e_{90°+\Delta\alpha} = (\Lambda_{t,90°+\Delta\alpha} - \Lambda_{t,90°})$ and $e_{90°-\Delta\alpha} = (\Lambda_{t,90°-\Delta\alpha} -$

$\Lambda_{t,90^\circ}$) are equal to:

$$e_{90^\circ+\Delta\alpha} = [\Delta A \cos\delta(\cos\Delta\alpha - 1) + (2A_{90^\circ+\Delta\alpha,III} + \Delta A)\sin\Delta\alpha\sin\delta + \\ + (A_{90^\circ+\Delta\alpha,II} + A_{90^\circ+\Delta\alpha,IV})\sin\Delta\alpha\sin\delta] \quad (3.18)$$

$$e_{90^\circ-\Delta\alpha} = [\Delta A \cos\delta(\cos\Delta\alpha - 1) - (2A_{90^\circ-\Delta\alpha,III} + \Delta A)\sin\Delta\alpha\sin\delta + \\ - (A_{90^\circ-\Delta\alpha,II} + A_{90^\circ-\Delta\alpha,IV})\sin\Delta\alpha\sin\delta] \quad (3.19)$$

The first term of both (3.18) and (3.19) is smaller than the other ones, under the above assumptions. These two relations define an anti-symmetric function of the tilt angle, which can be related to the behaviour of Fig. 3.16.

Chapter 4

Critical Aspects in Calibration of Electrostatic Discharge Generators

4.1 An overview on electrostatic discharge phenomena

Electrostatic discharge (ESD) problems have started to appear in the electronics industry between the 60s and 70s and have become increasingly critical due to the size of microcircuits; initially the most impacted areas were the military, aeronautical and those involved in the production and testing of computers. Later, owing to the presence of electronic equipment in almost all industrial areas, negative impacts have spread out requiring special precautions in the early stages of assemblage and manipulation as well as in the design and handling phases.

The current electronic components are exposed to ESD events (Table 4.1) of the order of a few hundred volts (*zero class* - see Table 4.2), because of their tiny dimensions.

A man is not usually able to warn such small ESD potentials through his senses and therefore is led to ignore or underestimate this problem in many industrial production cycles. The human perception of an ESD event through the senses occurs in the following way:

$$3000 \text{ V} \Longrightarrow \text{TOUCH}$$
$$5000 \text{ V} \Longrightarrow \text{HEARING}$$
$$10000 \text{ V} \Longrightarrow \text{SIGHT}$$

Table 4.1: Typical sensitivity levels of electronic components to ESD.

Component	**Sensitivity level (V)**
Mosfet	100-200
Eprom	100
Jfet	140-7000
Cmos	250-3000
Bipolar transistor	380-7000
Schottky diodes	300-2500

Table 4.2: ESD Component Classification REF EOS/ESD STM 5.1-1998.

Class	**Voltage range (V)**
0	<250
1A	250 to <500
1B	500 to <1000
1C	1000 to <2000
2	2000 to <4000
3A	4000 to <8000
3B	$\geq$ 8000

The presence of electrostatic fields in a production process, whose electronic components are handled by operators, can affect hardly the quality and the performance of the final product. The ESD faults are much more evident where a protection plan is not carried out or where operators don't observe the ESD standards in a ESD Protected Area (EPA). An EPA is an area without electrostatic fields, that could influence the reliability of handled components. To this end, the standard [23] requires an electrostatic field level lower than 100 V/cm. As concern components with ESD sensitivity threshold less than 100 V is suggested the 50% of that threshold in all areas close to ESD parts.

The protection against electrostatic fields in an EPA is achieved by:

- Grounding all conductive/dissipative materials including the staff.
- Neutralizing static charges on insulating materials by means of ionization-

shielding process.

Table 4.3: Typical discharge values in production process with respect to the relative humidity (UR%).

Event	**UR%: 10-20%**	**UR%: 65-90%**
Walking on a carpet	35000 V	1500 V
Walking on a vinyl floor	12000 V	250 V
Operator at workbench	6000 V	100 V
Vinyl envelopes	7000 V	600 V
Plastic handbag	20000 V	1200 V
Insulated chair	18000 V	1500 V

4.2 Introduction

The European Directive 2004/108/EC [24] on electromagnetic compatibility (EMC) dictates that a lot of tests on electrical and electronic equipment should be carried out in order to guarantee both low electromagnetic emission levels and sufficient immunity degrees against several disturbances in the environment.

Electrostatic discharge (ESD) immunity tests are carried out widely in order to assess the immunity level of several electrical and electronic equipment. ESD is one of the most severe sources of interference which can cause damages, upset or permanent failures in any electronic system. In recent years an increasing interest has been developing in the analysis of ESD phenomena, both in the industrial and academic world.

ESD on electronic devices can occur when a device becomes charged by tribo-electrification and approaches another conductor or when a human charged by tribo-electrification handles a device. Charge accumulation by tribo-electrification or induction process is at the origin of any ESD event. The effects produced by ESD are usually observed by considering separately conducted interference due to the direct injection of a discharge current in the victim device (i.e. *direct* effect), and radiated interference related to the coupling with the electromagnetic field radiated by the ESD current (i.e. *indirect* effect).

A great effort has been made by the scientific community in order to establish ESD standard procedures. To this aim, an important role has been played by several experimental studies on the ESD current waveform, focusing the attention on the amplitude and rise time variations as a function of the main influence quantities (relative humidity, electrode shapes, etc.) [25–27]. On the other hand, modelling approaches have been developed mainly with the aim to study the effect of design choices on the current and the radiated fields. In particular, the analysis has been carried out with satisfactory results through circuit simulation tools [28–31] and full wave electromagnetic methods [28, 29, 32–36], such as the Finite Difference Time-Domain, Finite Integration and Method of Moment techniques. Furthermore, the physical causes of the electric discharge and the capacitive parameters have been investigated in [37, 38].

The immunity test has to comply with specific standards [39, 40], where immunity requirements and test methods are fixed for equipment which must withstand ESD, either directly or indirectly. The standards consider two test methods: the contact discharge (CD) and the air discharge (AD) methods. In the first case the output of the ESD generator is kept in direct contact with the test point and the discharge event is injected by closing a switch. In the second method, the output of the generator is approached to the test point until a discharge in the air is obtained. The standards define ranges of test levels which relate to different environmental and installation conditions and establish test procedures. The object is to set a common and reproducible basis for evaluating the performance of electrical and electronic equipment when tested with electrostatic discharges. EMC standards define the typical waveform of the discharge current, range of test levels, test equipment, test set-up, test procedure, calibration procedure and measurement uncertainty. They also give specifications for tests performed in "laboratories" and "post-installation tests" on equipment in the final installation stage.

Based on the actual discharge characteristics, ESD generators are designed to provide current waveforms similar to those generated by the human body.

To improve the reproducibility of the results, the traceability of ESD generators, obtained by periodical calibrations, has to be accomplished. The calibration experience of INRIM (Istituto Nazionale di Ricerca Metrologica) [41, 42] and international comparisons, as [43], demonstrate that considerable differences may occur in the test results especially when generators of different manufacturers are used.

The chapter is focused on the detection and analysis of those parameters, related to the calibration set-up, that contribute to affect strongly the measurement result. The aim of the present chapter is to underline the influence

of several critical quantities on the fulfilment of the standard requirements and to warn the laboratory operators about the efforts that should be made during the calibration procedure.

An overview of the standard contents and their implications are given in § 4.3, while the results derived from the INRIM calibration experience and a critical analysis are carried out in § 4.4. Finally, § 4.6 is devoted to discussion, conclusions and suggestions.

4.3 Calibration set-up

The standards [39, 40] identify the CD method as the preferred test, whereas the AD one shall be used where contact discharges cannot be applied.

With regards to the CD method, the EMC standards recommend to check the following parameters related to the discharge current waveform: the first peak value (I_p), the rise time (t_r) and the current values at 30 ns (I_{30}) and 60 ns (I_{60}). The calibration of an ESD generator consists in measuring the above parameters and comparing them with those of the reference waveform (Fig. 4.1).

Table 4.4: Contact discharge current waveform parameters and tolerances (IEC 61000-4-2).

Level	**Test voltage, kV**	I_p **(±15%), A**	t_r **(±25%), ns**	I_{30} **(±30%), A**	I_{60} **(±30%), A**
1	2	7.5	0.8	4	2
2	4	15	0.8	8	4
3	6	22.5	0.8	12	6
4	8	30	0.8	16	8

The measurement set-up employed in the calibration of ESD generators, according to the CD mode, is made by several blocks (Fig. 4.2): the ESD generator (also known as *gun*) can be modelled by means of a basic equivalent circuit, consisting of a high voltage DC supply, a charging resistor R_c, a charging switch S', an energy-storage capacitor C_s, a discharging resistor R_d, a discharging switch S and a current return connection. The rated values of the components, stated by the standards, range from 110 pF to 330 pF for C_s and from 330 Ω to 2000 Ω for R_d. The immunity level is defined as the

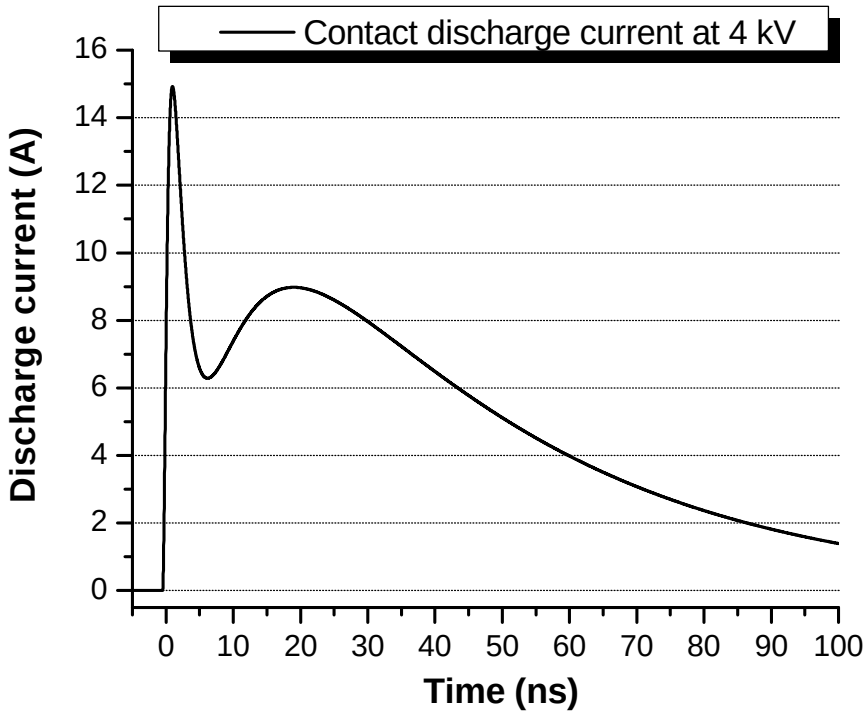

Fig. 4.1: Reference discharge current waveform (IEC 61000-4-2).

charge voltage of the capacitor C_s. The levels fixed by the EMC standards extend from 2 kV to 25 kV.

The discharge current is measured by means of a small-inductance coaxial shunt (the *target*), with nominal resistance of 2 Ω. The target is mounted in the centre of a vertical metal plane (the ground plane). The current return connection between the gun and the ground plane is made of a grounding cable.

An attenuator and a coaxial cable are used to accomplish the impedance matching and to carry the signal to a high speed digital sampling oscilloscope (DSO), whose bandwidth has to be equal to or greater than 2 GHz [39]. The whole measuring chain is placed inside a Faraday cage to protect the DSO from the electromagnetic field radiation of the ESD. Annexes B and C of [39] specify the requirements to build the target, together with the details of the transfer impedance of the target-attenuator-cable chain. A deep and detailed analysis of the whole measurement chain has been dealt with by [44, 45], where the influence of the target parameters and dynamic properties of the oscilloscope on the current "metrics" are highlighted.

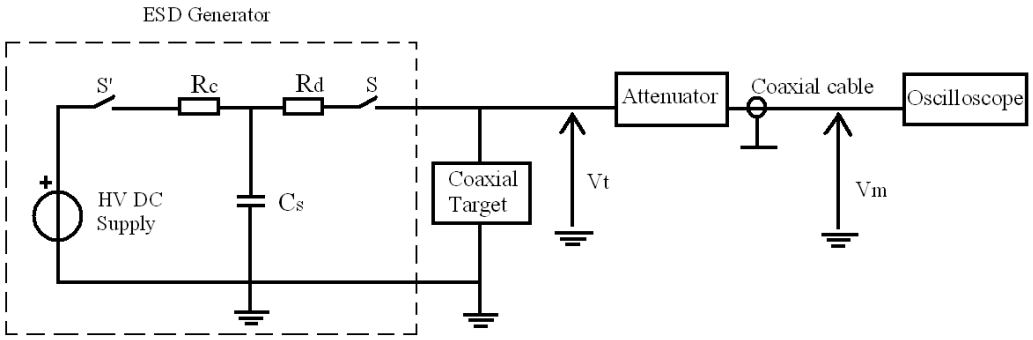

Fig. 4.2: Basic equivalent circuit of the ESD generator and block diagram of the target-attenuator-cable chain. The scheme refers to the CD calibration mode.

Since the ESD event is quite non-repeatable, the calibration of the ESD generator should be carried out carefully in order to verify that the gun fulfils the requirements in Table 4.4. Moreover, [39] fixes limited values for the tolerance associated to the different waveform parameters.

In order to provide some uncertainty values, reference [25] shows the following typical uncertainty contributions (2σ) derived from many calibration reports by accredited laboratories: 8% for the current peak value and 5-7% for the rise time (CD mode).

4.4 Calibration Experience

During the last three years, the EMC laboratory of INRIM performed about thirty calibrations according to both IEC and ISO standards, on fourteen different guns produced by four manufacturers. For some devices, successive calibrations are available up to three. On the basis of the calibration data collected in the INRIM experience [41], [42], an experimental analysis has been carried out in order to detect the main reasons affecting the dispersion of the parameters in the calibration procedure.

4.4.1 CD mode analysis

As far as the contact discharge mode is concerned, the standard calibration chain has been set up. Referring to the scheme sketched in Fig. 4.2, two ESD generators of the same manufacturer have been employed [46]. From here on, they will be referred to as *30N* and *P18*, respectively. The measurements have been performed by means of a digital oscilloscope LeCroy Wavepro

Table 4.5: Target input DC resistance.

Nominal value:	2.000 Ω
Measured value:	1.971 Ω
Uncertainty:	0.006 Ω

Table 4.6: Insertion loss as a function of frequency.

Frequency, MHz	**Insertion Loss, dB**	**Uncertainty, dB**
0.01	42.67	0.40
1	42.78	0.29
100	42.93	0.28
1000	43.08	0.28
2000	43.19	0.28
4000	42.35	0.33

760Zi, which allows to set different analog bandwidths (up to 6 GHz), with a maximum single-shot sample rate of 40 GS/s. The input impedance of the DSO has been set at 50 Ω. The frequency response of the INRIM target has been evaluated accurately by means of a vector network analyser up to 4 GHz. Table 4.5 shows the good agreement between the measured DC resistance and the requirement of the Annex B of IEC standard (maximum 2.1 Ω). The insertion loss variations, reported in Table 4.6, are well within ±0.5 dB over the whole frequency range from 10 kHz to 4 GHz, as required by the standard (±0.5 dB up to 1 GHz, ±1.2 dB from 1 to 4 GHz). The measurement chain has been placed inside a shielded chamber.

The tests have been carried out with the generator supported by both a metal and a non-metal low loss tripod. In this way, a stable placement and an orthogonal position with respect to the vertical plane is ensured and the influence of the constitutive structure of the tripod can be investigated.

The analysis has been performed whilst paying special attention to the items below with regards to the current waveform and parameters.

The situation specified in the Appendix B of the IEC standard (grounding cable connected to the vertical plane at a 500 mm distance below the target and pulled by forming an isosceles triangle) will be referred to as the *reference configuration*. Each generator has been tested at a 4 kV level as a function

of:

- the DSO bandwidth;
- the grounding cable cross-section;
- the grounding cable configuration;
- the connection point of the grounding cable at the vertical plane;
- the tripod type.

Effect of the DSO bandwidth

As mentioned above, the bandwidth of the oscilloscope used may be set at several values, from 20 MHz to 6 GHz. Presently, the standards specify a minimum bandwidth equal to 2 GHz. This section shows the influence of wider bandwidth values mostly on the current peak value and the rise time. The two generators have been tested in the reference situation, by varying the DSO bandwidth from 1 GHz to 6 GHz. The percentage deviations between the minimum and the maximum current peaks have been found equal to 3% for the 30N gun and 10% for the P18 gun, as shown in Fig. 4.3 and Fig. 4.4, where the peak differences have been enlarged. The guns are supported here by a non-metal tripod. It can be discerned that a wider bandwidth of the DSO would allow critical situations to be detected (values close to the standard limits, see Table 4.4), which may influence the calibration result. Moreover, it should be noted that the current waveform of the 30N gun is slightly far from the reference one (Fig. 4.1), whereas the P18 gun complies better.

Effect of the grounding cable cross-section

In order to investigate the influence of the grounding cable cross-section, measurements have been performed by using a circular cross-section cable of small radius (referred to as *thin*) and a rectangular cross-section strap cable (*flat*). Both cables have a 2 m length and are connected to the vertical plane at a 330 mm distance from the target on its right. The bandwidth has been set at 6 GHz. Figure 4.5 compares the waveforms discharged with the two grounding cables and the metal tripod by the P18 gun. It should be noted how the choice of the cable strongly modifies the current waveform. It is worth underlining the standards do not indicate any specific requirement for the cable except for the length ((2±0.05) m).

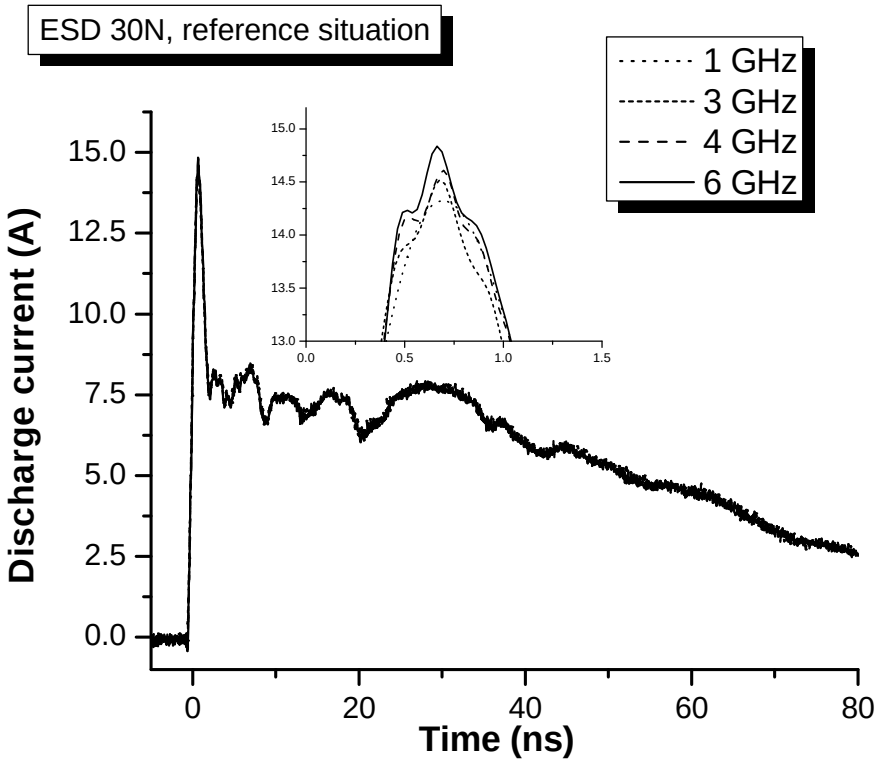

Fig. 4.3: Influence of the bandwidth on the peak value of the discharge current. The ESD generator used is 30N.

Effect of the grounding cable connection

In order to analyse the behaviour of the discharge current as a function of the grounding cable connection to the vertical plane, several set-up configurations have been considered.

Although the EMC standards dictate a contact discharge calibration procedure (reference configuration), often the laboratory technicians, charged with calibrating operations, do not pay sufficient attention to the recommended tips. Therefore, it is important to underline the effects resulting from not following the standard prescription.

The grounding cable has been stuck to the metallic plane in two different points, on the right and left side of the target at a 650 mm distance, always forming an isosceles triangle. From here on, this configuration will be referred to as the Δ configuration. For both guns, the waveforms are very stable and show a good compliance with the standard limits (within the indicated tolerances). Conversely, when the grounding cable is laid on the floor (configuration *free*), the transient behaviour is quite different for

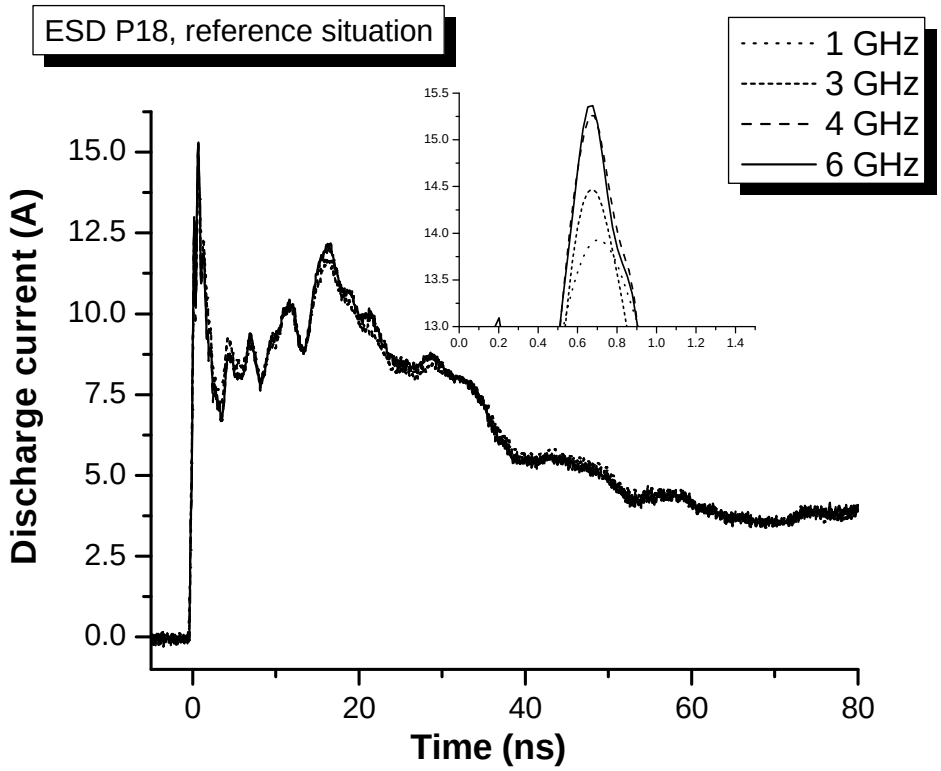

Fig. 4.4: Influence of the bandwidth on the peak value of the discharge current. The ESD generator used is P18.

the two guns. These measurements have been carried out by connecting the grounding cable at 330 mm and 650 mm distances, on both the right and the left with respect to the target. The 30N gun maintains a good stability and repeatability, as shown in Fig. 4.6 and Fig. 4.7. Differently, the P18 gun shows a strong dependence on the ground strap position (Fig. 4.8 and Fig. 4.9): in particular, the parameter I_{30} is often very close to the tolerance limits fixed by the standards. The current behaviour in the time range 1 ns to 20 ns complies with the reference current, except a high second peak which is not considered by the standards.

Tripod type

The influence of the type of the gun support is to be investigated here. As mentioned above, two different tripods have been used. The 30N gun is again quite stable and does not present appreciable differences as a function of the tripod type. Conversely, the P18 gun differs in its behaviour because of the high capacitive couplings between the ground strap and the tripod

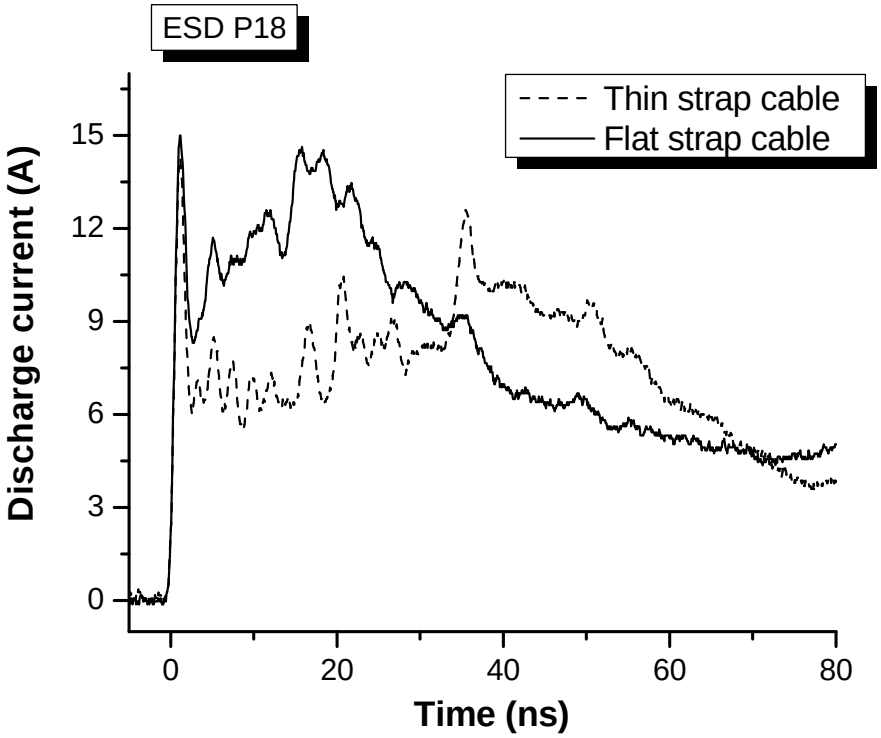

Fig. 4.5: Influence of the grounding cable cross-section on the current waveform. The ESD generator used is P18.

itself (Fig. 4.10).

4.4.2 AD mode analysis

As far as the AD method is concerned, EMC standards do not recommend any specific calibration method. Some authors have also shown how the use of a target for the measurement of the AD current presents a wide numerical dispersion [25].

Only the tolerance of the charge voltage is specified and set equal to $\pm 5\%$ of the nominal value. Therefore, the measurement of the charge voltage may be used for the calibration, by means of high input impedance systems. This operation is carried out by closing the switch S' (see Fig. 4.2) and keeping the generator tip in contact with the input terminals of a high impedance probe, whose output voltage is read by a multimeter (Fig. 4.11). The waveform of the voltage can be drawn on a digital oscilloscope. After an initial transient phase, the output voltage reaches a steady-state DC value, as shown

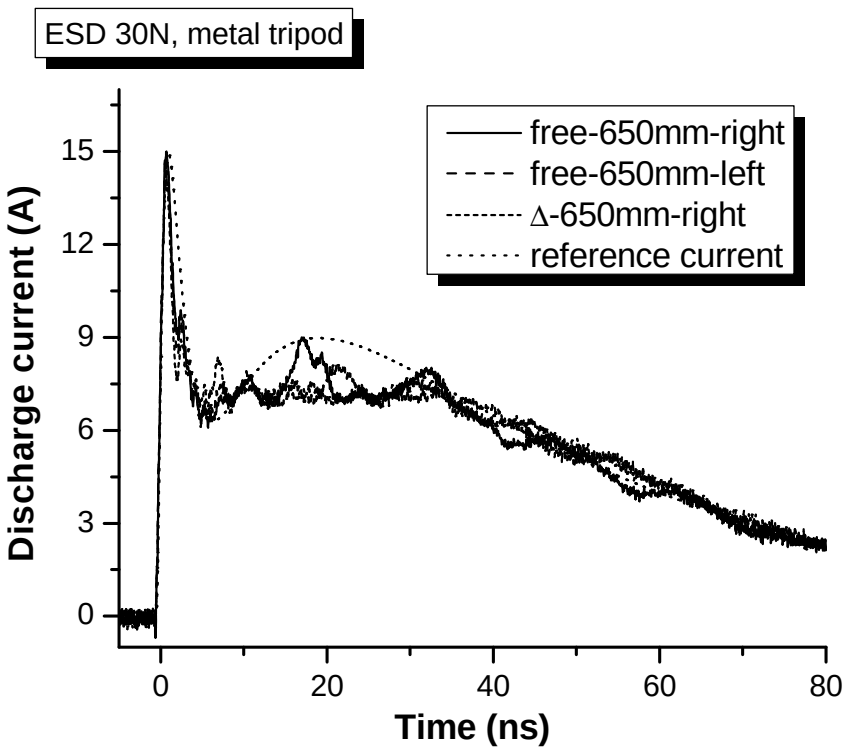

Fig. 4.6: Influence of the grounding cable connection at 650 mm distance and comparison with the reference current. The ESD generator used is 30N with a thin grounding cable.

in Fig. 4.12. Since the input impedance is very high but finite, the measurement chain exhibits a load effect. The aim is to find out the minimum input impedance that guarantees an acceptable load effect, in comparison to the required tolerance.

Many high voltage probes for DC measurements are available on the market, with an input impedance of about 1 GΩ and a nominal divider ratio r equal to 10^3 ($r = V_{in}/V_{out}$). By using a 40 kV probe with those characteristics, an important load effect of about 15% can be detected (Fig. 4.12). The values in the graph are all normalized with respect to the charge voltage value v_0 (4 kV). This effect has been proved through measurements for several voltage levels (from 1 to 15 kV) and an analogous behaviour has been found at each step.

In order to reduce this effect, a resistive voltage divider with an input impedance of 10 GΩ and r equal to 10^4 has been built as a voltage converter device [41]. The voltage waveform detected by using the INRIM 10 GΩ

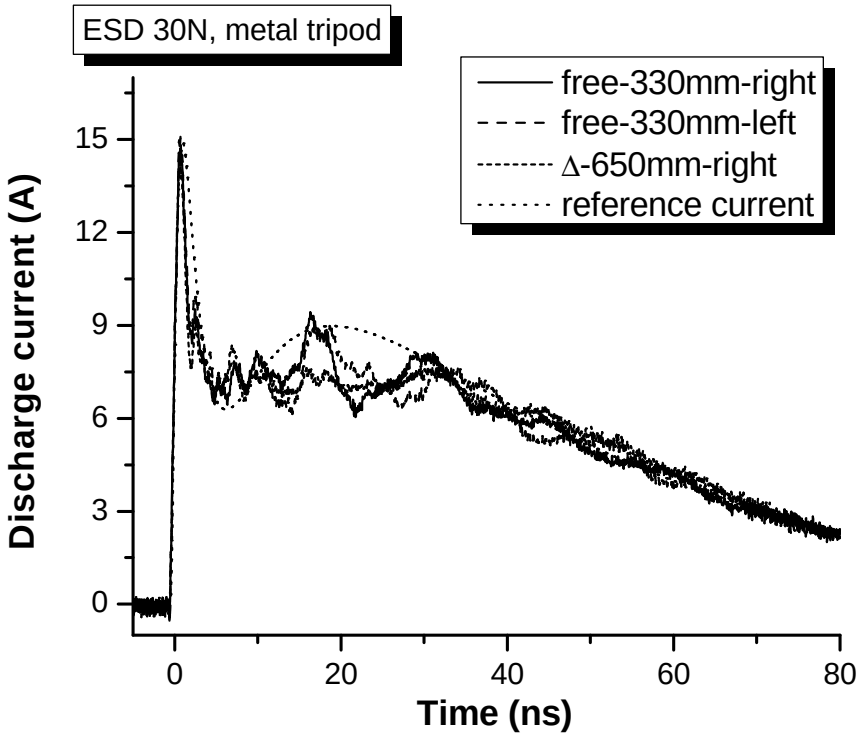

Fig. 4.7: Influence of the grounding cable connection at 330 mm distance and comparison with the reference current. The ESD generator used is 30N with a thin grounding cable.

divider, coupled with the DSO, shows a reduced load effect of about 0.8% (Fig. 4.12).

To further reduce the voltage drop, a new resistive voltage divider with an input impedance equal to 50 GΩ has been designed and built recently. The design of the divider started with the choice of the high-voltage (HV) resistors. Ten 5 GΩ resistors mounted on a dielectric support have been used to achieve the aim of a high resistance value and a good dielectric strength. The resistors have been selected to obtain a uniform voltage distribution along the resistors chain (Fig. 4.13). The low voltage resistance consists of two resistors connected in parallel. The thermal coefficient of low voltage resistors is 100 ppm/°C, the same as the HV ones. The divider ratio ($r = 10^4$) has been chosen according to the high input impedance/high accuracy range of the multimeter used for measuring the output voltage. Both high and low voltage resistors have been placed in a PMMA cylinder. Two electrodes mounted on the top and on the bottom of the cylinder avoid the occurrence

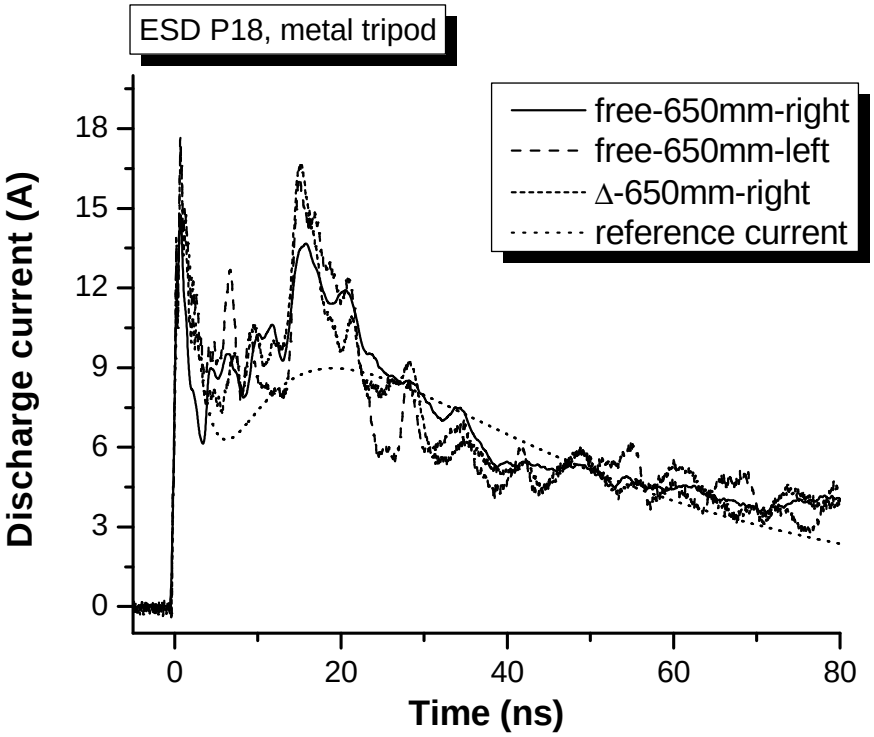

Fig. 4.8: Influence of the grounding cable connection at 650 mm distance and comparison with the reference current. The ESD generator used is P18 with a flat ground strap.

of the corona discharge. As the HV resistor values can be affected by surface conductivity, the humidity in the cylinder is lowered using silica gel. The linearity is ensured by making a comparison with the INRIM HV DC reference measuring system. The scale factor of all three voltage probes is determined at 1 kV, supplying the probes by means of a DC calibrator.

The behaviours of the three employed probes are gathered in Fig. 4.12. As expected on the basis of the 10 GΩ divider results, a load effect of about 0.1% is obtained with the 50 GΩ device. The ripple on the 10 GΩ and 50 GΩ waveforms is caused by the power network interference (50 Hz), picked up by the high input impedance of the divider.

It can be inferred that a satisfactory reduction of the load effect is obtained through the use of a voltage divider with at least 10 GΩ input impedance.

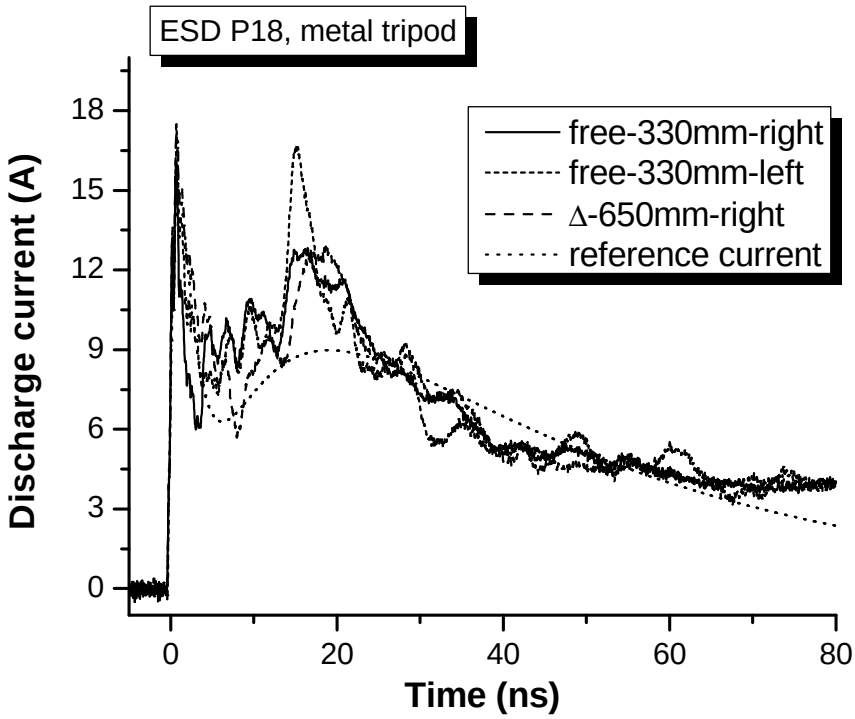

Fig. 4.9: Influence of the grounding cable connection at 330 mm distance and comparison with the reference current. The ESD generator used is P18 with a flat ground strap.

4.5 Preliminary modelling approach

With regard to the CD calibration set-up, a great effort has been made in the implementation of a suitable non-commercial numerical model, which allows to compute and identify the optimal set-up configurations, to improve the measurement repeatability and reproducibility. As a full-wave model requires a large effort, preliminary considerations are derived from a simple circuital-based approach.

In the literature, some authors have proposed both circuital and full-wave ESD generator models [28, 29, 47, 48]. To assure model accuracy, a key issue is the accurate computation of those stray distributed parameters which strongly affect the discharge current waveform, in particular the current tail.

A preliminary analysis of some stray parameter effects on the ESD waveform can be carried out through the circuital model [28], sketched in Fig. 4.14: In order to investigate the sensitivity of the current waveform to the

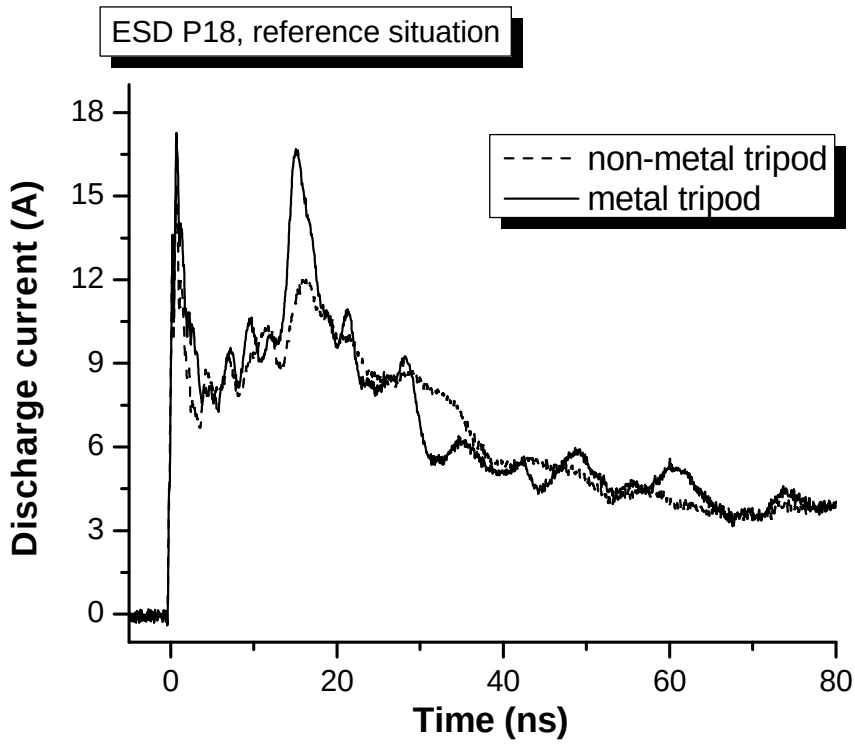

Fig. 4.10: Influence of the tripod type on the current waveform. The ESD generator used is P18.

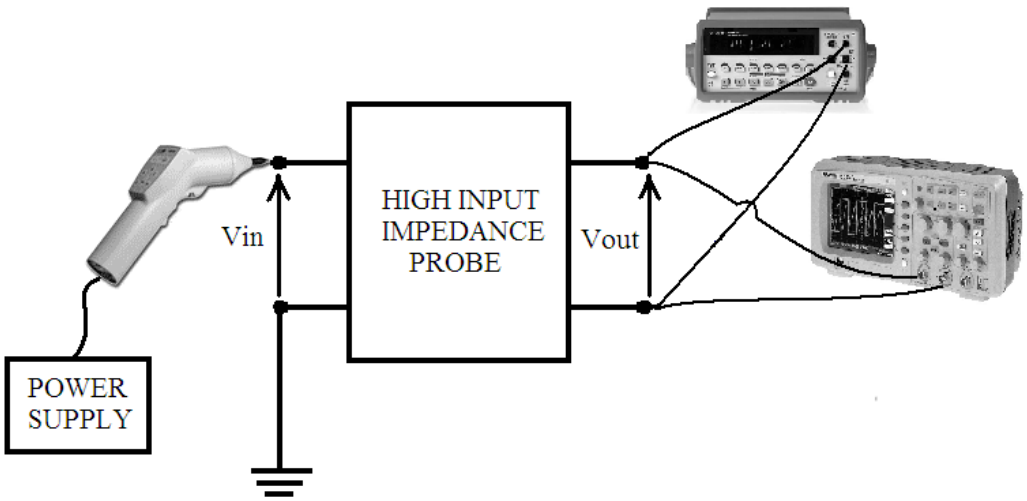

Fig. 4.11: Measurement system for the ESD generator calibration-AD mode.

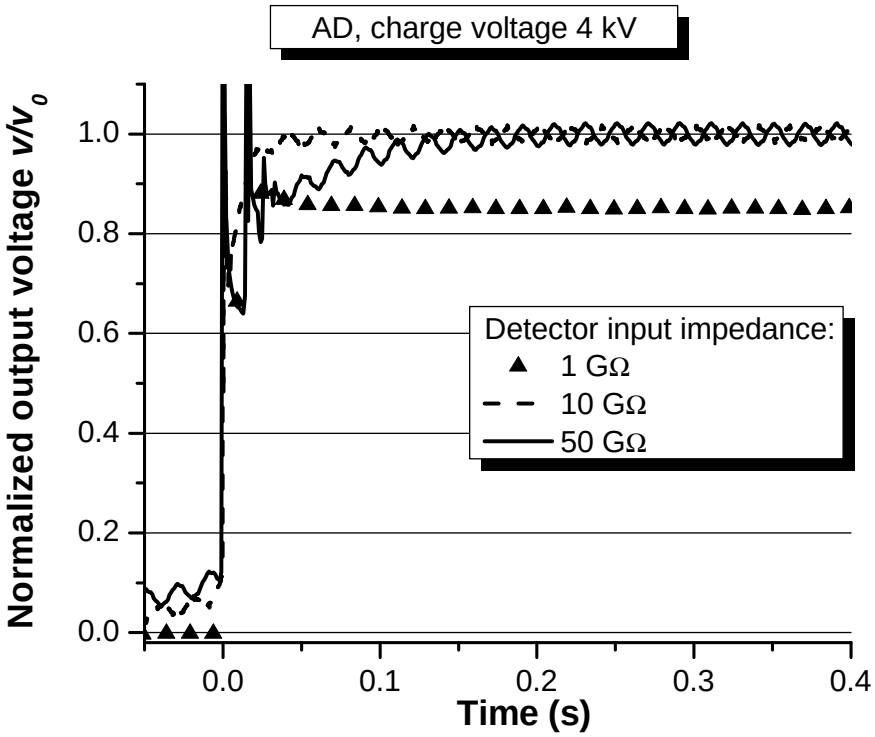

Fig. 4.12: Comparison of the load effect on a 4 kV charge voltage, by using a 1 GΩ, a 10 GΩ and a 50 GΩ divider.

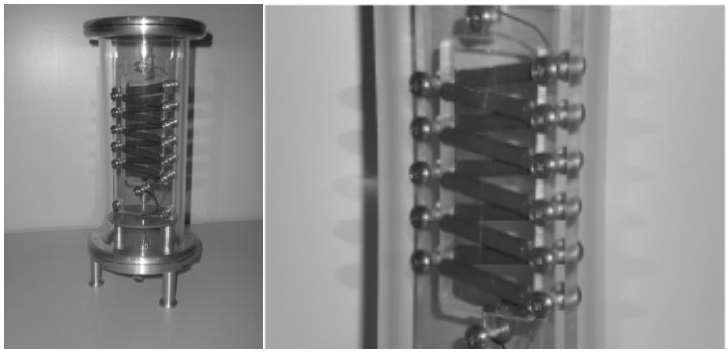

Fig. 4.13: Details of the INRIM 50 GΩ voltage divider.

stray parameters, it is interesting to analyse different circuital situations, in which one or more parameters are changed within an appropriate range. The resulting current waveforms are then compared with the IEC reference current. The following figures highlight the strong sensitivity of the current waveform to the gun-wall capacitance (Fig. 4.15), and to the characteristic

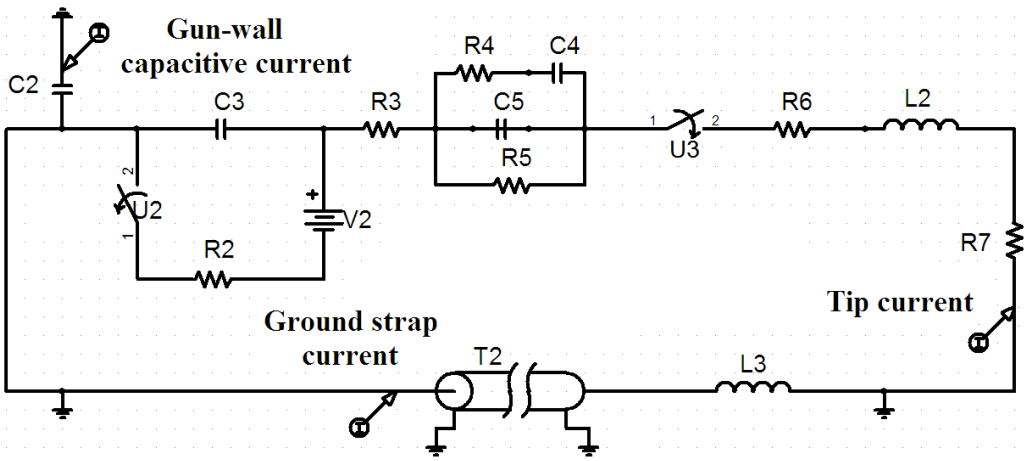

Fig. 4.14: Circuital model of the ESD generator and the experimental set-up (CD method).

parameters (time delay and characteristic impedance) of the ground strap cable modelled as a transmission line (Fig. 4.16). As in the results of the

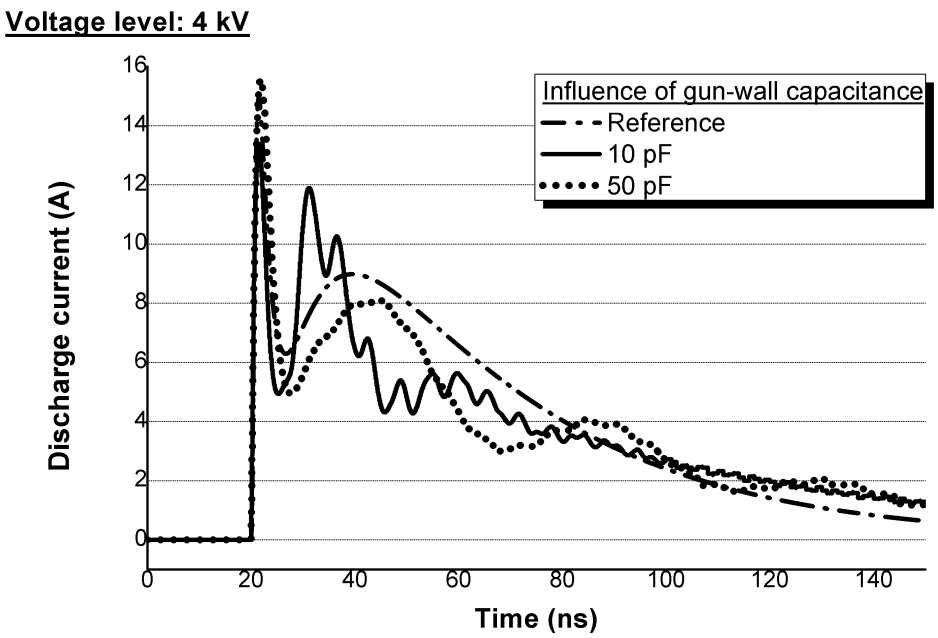

Fig. 4.15: Sensitivity of the current waveform to the gun-wall capacitance.

measurements, the current waveform in Fig. 4.15 shows the presence of a

second high peak, while the other figures underline the effects on the tail behaviour, in particular referring to the I_{30} and I_{60} parameters. However, the approximated approach of the circuital model does not allow an exhaustive and complete modelling analysis of the whole distributed system (ESD generator + ground strap + metallic wall), in particular as regards the investigation of the electromagnetic behaviour in the high part of the frequency spectrum. Therefore, our aim is to develop a more accurate modelling approach to describe the system completely (Chapter 5).

4.6 Further Considerations

This chapter deals with several critical aspects of the ESD generator calibration process in order to convey ideas and advice for the procedure improvement to both the scientific community and the laboratory technicians.

On the basis of the results presented above, some useful conclusions and practical suggestions can be drawn.

As far as the contact discharge mode calibration is concerned, the following issues may be considered in the review process of the future ESD standard editions:

- the bandwidth of the DSO should be enlarged to values greater than 2 GHz, in order to detect with higher accuracy the first current peak and the rise time values. Indeed, considerable variations can be pointed out (Fig. 4.3 and Fig. 4.4) with a DSO bandwidth ranging from 1 GHz to 6 GHz;

- Figure 4.5 highlights that the current waveform can significantly vary as a function of the used grounding cable. Therefore, as well as the cable length, its cross-section and size also play an important role in stating the features of the waveform. It should be desirable to make the measurement outcome as independent as possible of the cable geometry;

- a relevant second peak often appears in the time interval between 1 ns and 20 ns (Fig. 4.8 and Fig. 4.9). That current behaviour is surely indicative of an unevenness, which should be investigated and reduced as much as possible in order to improve the repeatability of the calibration procedure and reduce the related uncertainty. This phenomenon is also supported by numerical investigations in [28, 47].

However, it should be noted that the compliance with the present standard requirements (i.e. the reference situation and low loss tripod) allows

to fulfil the reference waveform parameters in a satisfactory way. Consequently, this implies the laboratory technicians performing the calibration should follow the standard recommendations with extreme care.

Taking into account the great variability of the CD calibration outcomes, the possibility to perform a calibration process with the support of numerical methods should be considered in the near future, giving rise to a hybrid experimental-numerical approach in order to verify the actual performance of the ESD generator.

As regards the air discharge mode calibration, the proposed measuring scheme (§ 4.4) can be considered suitable to fulfil the voltage requirements of the ESD standards.

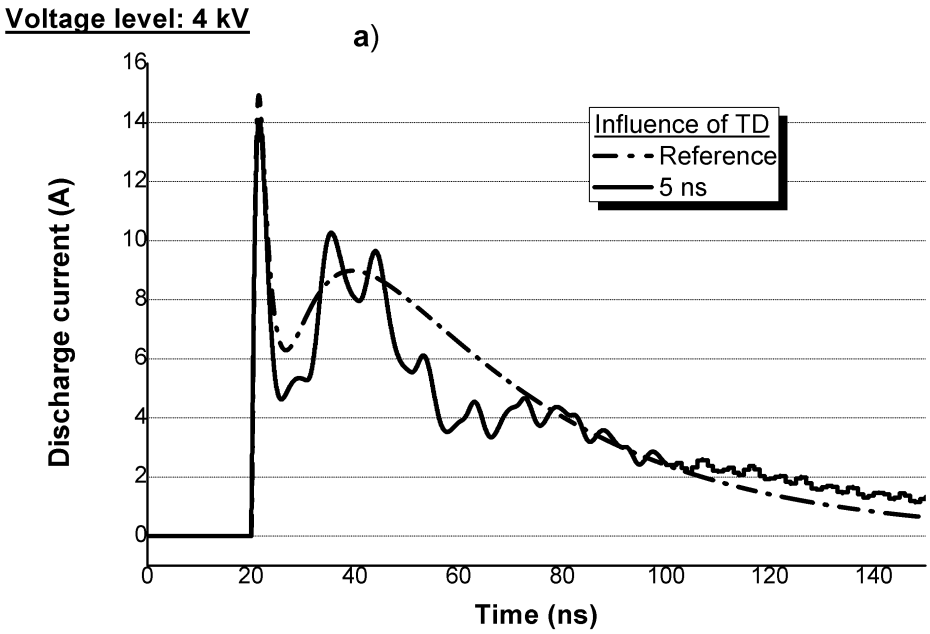

(a) time delay (TD)

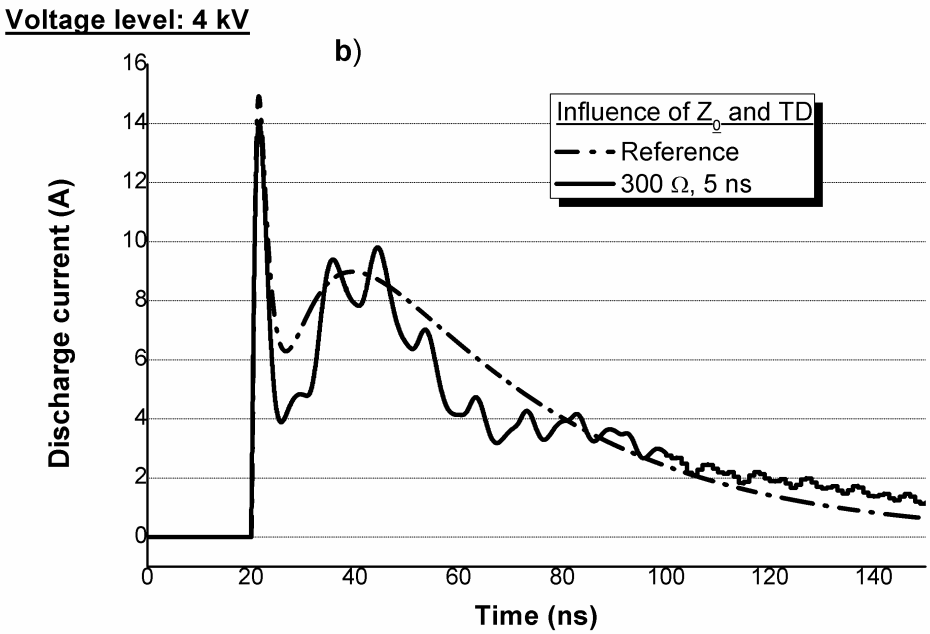

(b) characteristic impedance (Z_0)

Fig. 4.16: Sensitivity of the current waveform to the ground strap parameters.

Chapter 5

PEEC Global Approach

5.1 Introduction

The problems dealt with so far are characterized by a strong coupling between electromagnetic fields and circuits and they cover a very wide frequency bandwidth.

In order to support experimental outcomes and to provide a complete engineering tool for design and laboratory activities, a suitable computational method is sought.

A deep research in scientific literature on the main numerical methods is carried out and a great attention is addressed to those fulfil the following issues:

- Formulation in both time and frequency domain;
- Full-wave method: the mathematical formulation is based on the complete Maxwell's equations, i.e. they do not introduce some principle assumptions with respect to the wave-propagation modes;
- Full-spectrum method: model valid from DC to the maximum frequency determined by the meshing;
- Low computational time.

On the basis of these requirements, the Partial Element Equivalent Circuit (PEEC) method is considered the most suitable approach: it is based on the circuital interpretation of the mixed-potential integral equation (MPIE, see § 5.2) and it is characterized by a great versatility in its applications. The classical full-wave formulation of the PEEC method has been derived from the MPIE for the free space by A.E. Ruehli [49] in 1974. The later perfections and

modifications of the PEEC method use same derivation principles regarding to basis and weighting functions, partial elements, and an equivalent circuit representation.

In literature, the PEEC has been found particularly useful for modeling many problems, for example:

- ↪ non-uniform and non parallel transmission lines [50];
- ↪ multilayer printed circuit boards [51];
- ↪ lightning protection systems [52];
- ↪ very large-scale integration chips [53];
- ↪ multiconductor interconnection structures [54];
- ↪ air-core reactors [55];
- ↪ magnetic near field of a static converter [56].

Of course, no numerical method may be accepted as the best universal tool for all kinds of electromagnetic problems, as well, the PEEC method has advantages and disadvantages as compared to other approaches. Its main merit is an equivalent circuit representation, which allows the full-wave PEEC model to be directly included in a circuit-simulation code. Thus, the simultaneous modeling of electric systems with the lumped active devices is achieved, which is very suitable for the EMC analysis as well as the design of electrical devices.

5.2 Basic Principles

Starting with the equation for the electric field $\mathbf{E}$ at a point $\mathbf{r} = (x, y, z)$ in space:

$$\mathbf{E}(\mathbf{r}, t) = \mathbf{E}^{(i)}(\mathbf{r}, t) + \mathbf{E}^{(s)}(\mathbf{r}, t) = \mathbf{E}^{(i)}(\mathbf{r}, t) - \frac{\partial \mathbf{A}(\mathbf{r}, t)}{\partial t} - \nabla\Phi(\mathbf{r}, t) \tag{5.1}$$

where $\mathbf{E}^{(i)}$ is the incident electric field and $\mathbf{E}^{(s)}$ is the scattered electric field, as usual described in terms of electric scalar $\Phi(\mathbf{r}, t)$ and magnetic vector $\mathbf{A}(\mathbf{r}, t)$ potentials. Applying the Lorentz-gauge condition, the vector magnetic potential $\mathbf{A}$ and the scalar electric potential Φ are written as:

$$\mathbf{A}(\mathbf{r}, t) = \mu \int_{v'} G(\mathbf{r}, \mathbf{r}')\mathbf{J}_t(\mathbf{r}', t - \tau)\mathrm{d}V' \tag{5.2}$$

$$\Phi(\mathbf{r},t) = \frac{1}{\varepsilon_0}\int_{v'} G(\mathbf{r},\mathbf{r}')\rho_t(\mathbf{r}',t-\tau)\mathrm{d}V' \tag{5.3}$$

where

- $G(\mathbf{r},\mathbf{r}') = \dfrac{1}{4\pi \mid \mathbf{r}-\mathbf{r}' \mid}$ is the free space Green's function,
- $\tau = \dfrac{\mid \mathbf{r}-\mathbf{r}' \mid}{c}$ is the delay time due to the finite light speed c,
- $\mathbf{J}_t = \mathbf{J}_c + \mathbf{J}_d$ represents the sum of the conduction $\mathbf{J}_c$ and dielectric $\mathbf{J}_d$ current densities (dielectric materials, see § 5.2.2),
- $\rho_t = \rho_f + \rho_b$ is the sum of the free ρ_f and bounded ρ_b charge densities in the dielectric regions.

5.2.1 PEEC equation in a conducting region

If the field point $\mathbf{r}$ is set into a conducting region and (5.2),(5.3) are inserted into (5.1), the mixed-potential integral equation (5.4) is developed.

$$\begin{aligned}\mathbf{E}^{(i)}(\mathbf{r},t) = \frac{1}{\sigma}\mathbf{J}_c(\mathbf{r},t) + \mu\int_{v'} G(\mathbf{r},\mathbf{r}')\frac{\partial \mathbf{J}_c(\mathbf{r}',t-\tau)}{\partial t}\mathrm{d}V' + \\ + \mu\int_{v'} G(\mathbf{r},\mathbf{r}')\frac{\partial \mathbf{J}_d(\mathbf{r}',t-\tau)}{\partial t}\mathrm{d}V' + \\ + \frac{1}{\varepsilon_0}\nabla\int_{v'} G(\mathbf{r},\mathbf{r}')\rho_t(\mathbf{r}',t-\tau)\mathrm{d}V'\end{aligned} \tag{5.4}$$

Unlike the MoM-type solution, the charge density variable is not replaced by the current density through the continuity equation. The charges are assumed to be located on the surface of the volumes and then the relative integrals can be written as surface integrals.

To solve (5.4) numerically, volumes and surfaces are divided into elementary cells (*partial elements*). The spatial integrals over the conducting object become sum of integrals over the single cells.

Two kind of cells have to be created:

- *volume* (*current*) cells carrying the conduction (or dielectric) current;
- *surface* (*potential*) cells carrying the surface charges.

The length of cells has to be less than $\lambda_m/20$, where λ_m is the wavelength corresponding to the maximum frequency of interest. The current and charge

densities are represented via pulse basis functions as:

$$\mathbf{J}_t(\mathbf{r}) = \sum_{m\in M} \frac{I_m}{a_m}\hat{\mathbf{e}}_m b_m^v(\mathbf{r}), \quad b_m^v(\mathbf{r}) = \begin{cases} +1 & \mathbf{r} \in v_m \\ 0 & \mathbf{r} \notin v_m \end{cases}$$

$$\rho_t(\mathbf{r}) = \sum_{i\in K} \frac{q_i}{\Sigma_i} b_i^s(\mathbf{r}), \quad b_i^s(\mathbf{r}) = \begin{cases} +1 & \mathbf{r} \in s_i \\ 0 & \mathbf{r} \notin s_i \end{cases} \tag{5.5}$$

where v_m and a_m are the volume and the cross-section of current cells respectively, $\hat{\mathbf{e}}_m$ is the unit vector giving the direction of the current in the cell m, M is the set of current cells, I_m is the current in the cell m, Σ_i is the surface of potential cells, Q is the set of potential cells, q_i is the charge on the potential cell i.

Applying a Galerkin type weighting technique (basis functions equal to weighting functions, see § 2.4.1) through an inner product operator

$$\hat{\mathbf{e}}_\alpha \cdot \frac{1}{a_\alpha}\int_{v_\alpha} ... \quad \mathrm{d}V_\alpha$$

Eq. (5.4) is written for the generic n-th cell, as:

$$\begin{aligned} \frac{\hat{\mathbf{e}}_n}{a_n} \cdot \int_{v_n} \mathbf{E}^{(i)}(\mathbf{r},t)\mathrm{d}V_n = \frac{\hat{\mathbf{e}}_n}{a_n} \cdot \int_{v_n} \frac{1}{\sigma}\mathbf{J}_c(\mathbf{r},t)\mathrm{d}V_n + \\ + \frac{\mu}{a_n}\hat{\mathbf{e}}_n \cdot \int_{v_n}\int_{v'} G(\mathbf{r},\mathbf{r}')\frac{\partial \mathbf{J}_c(\mathbf{r}',t-\tau)}{\partial t}\mathrm{d}V'\mathrm{d}V_n + \\ + \frac{\mu}{a_n}\hat{\mathbf{e}}_n \cdot \int_{v_n}\int_{v'} G(\mathbf{r},\mathbf{r}')\frac{\partial \mathbf{J}_d(\mathbf{r}',t-\tau)}{\partial t}\mathrm{d}V'\mathrm{d}V_n + \\ + \frac{\hat{\mathbf{e}}_n \cdot \nabla}{\Sigma_n \varepsilon_0}\int_{s_n}\int_{s'} G(\mathbf{r},\mathbf{r}')\rho_t(\mathbf{r}',t-\tau)\mathrm{d}S'\mathrm{d}S_n \end{aligned} \tag{5.6}$$

where v', v_n are called source and observation volumes, respectively, and s', s_n are the source and observation surfaces.

The algebraic equation for a conducting volume can be then derived from (5.6), (5.5) and the gradient in (5.6) is replaced by the difference quotient that causes a shift of potential and current cells at a half of their length (Fig. 5.1).

The PEEC technique interprets equation (5.6) in terms of circuit elements. The left-hand side of (5.6) is equivalent to an independent voltage source, the terms in the right-hand side are equivalent to a resistive, inductive and capacitive voltage drops, respectively (Fig. 5.2). In fact, the following quantities can be defined:

$$\frac{1}{a_n}\int_{v_n} \hat{\mathbf{e}}_n \cdot \mathbf{E}^{(i)}(\mathbf{r},t)\mathrm{d}V_n \triangleq V_{sn} \quad \Rightarrow \textit{independent voltage source} \tag{5.7}$$

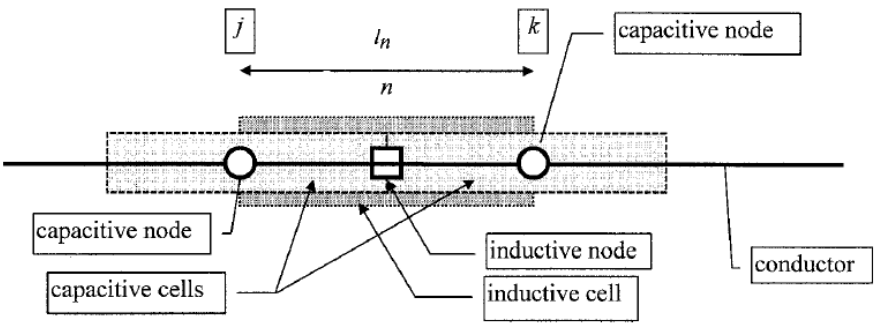

Fig. 5.1: A conductor divided in two capacitive PEEC cells and one inductive cell.

$$\int_{v_n} \frac{\mathrm{d}V_n}{\sigma a_n^2} \triangleq R_n \quad \Rightarrow \textit{series resistance} \tag{5.8}$$

$$\frac{\mu}{a_n a_m} \int_{v_n} \int_{v'_m} G(\mathbf{r}, \mathbf{r}') \hat{\mathbf{e}}_n \cdot \hat{\mathbf{e}}_m \mathrm{d}V'_m \mathrm{d}V_n \triangleq L_{nm} \quad \Rightarrow \textit{partial inductance} \tag{5.9}$$

$$\frac{1}{\varepsilon_0 \Sigma_n \Sigma_m} \int_{s_n} \int_{s'_m} G(\mathbf{r}, \mathbf{r}') \mathrm{d}S'_m \mathrm{d}S_n \triangleq p_{nm} \quad \Rightarrow \textit{potential coefficient} \tag{5.10}$$

5.2.2 PEEC equation in a dielectric region

Because we need an equation similar to (5.4) for a dielectric region, we have to give a material equation similar to Ohm's law for dielectrics [57]. We define the *dielectric* current density $\mathbf{J}_d$ the quantity derived from the right-hand side of the Ampere's law, as in the following:

$$\begin{aligned} \mathbf{J}_c + \varepsilon_0 \varepsilon_r \frac{\partial \mathbf{E}}{\partial t} &= \mathbf{J}_c + \varepsilon_0 \frac{\partial \mathbf{E}}{\partial t} - \varepsilon_0 \frac{\partial \mathbf{E}}{\partial t} + \varepsilon_0 \varepsilon_r \frac{\partial \mathbf{E}}{\partial t} = \\ = \mathbf{J}_c + (\varepsilon_r - 1)\varepsilon_0 \frac{\partial \mathbf{E}}{\partial t} + \varepsilon_0 \frac{\partial \mathbf{E}}{\partial t} &= \mathbf{J}_c + \mathbf{J}_d + \varepsilon_0 \frac{\partial \mathbf{E}}{\partial t} = \mathbf{J}_t + \varepsilon_0 \frac{\partial \mathbf{E}}{\partial t} \end{aligned} \tag{5.11}$$

where ε_r is the permittivity of the medium. Since

$$\mathbf{J}_d(\mathbf{r}, t) = (\varepsilon_r - 1)\varepsilon_0 \frac{\partial \mathbf{E}(\mathbf{r}, t)}{\partial t}$$

we get from the definition of the dielectric current above:

$$\mathbf{E}(\mathbf{r}, t) = \frac{1}{(\varepsilon_r - 1)\varepsilon_0} \int_{-\infty}^{t} \mathbf{J}_d(\mathbf{r}, \tau) d\tau \tag{5.12}$$

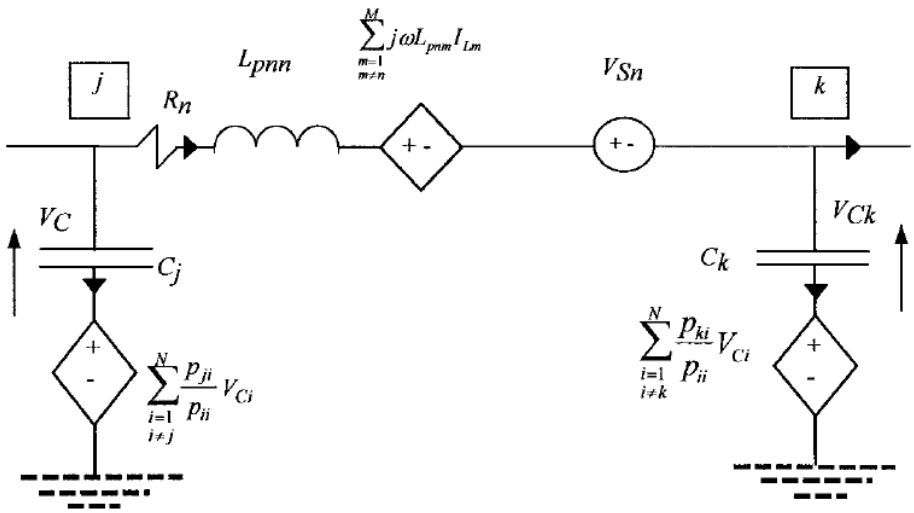

Fig. 5.2: Elementary PEEC conductive cell between nodes j and k.

Equation (5.1) for a point on a dielectric becomes:

$$\frac{1}{(\varepsilon_r - 1)\varepsilon_0} \int_{-\infty}^{t} \mathbf{J}_d(\mathbf{r}, \tau) d\tau + \frac{\partial \mathbf{A}(\mathbf{r}, t)}{\partial t} + \nabla \Phi(\mathbf{r}, t) = \mathbf{E}^{(i)}(\mathbf{r}, t) \tag{5.13}$$

or

$$\begin{aligned} \mathbf{E}^{(i)}(\mathbf{r}, t) = & \frac{1}{(\varepsilon_r - 1)\varepsilon_0} \int_{-\infty}^{t} \mathbf{J}_d(\mathbf{r}, \tau) d\tau + \mu \int_{v'} G(\mathbf{r}, \mathbf{r}') \frac{\partial \mathbf{J}_c(\mathbf{r}', t - \tau)}{\partial t} \mathrm{d}V' + \\ & + \mu \int_{v'} G(\mathbf{r}, \mathbf{r}') \frac{\partial \mathbf{J}_d(\mathbf{r}', t - \tau)}{\partial t} \mathrm{d}V' + \\ & + \frac{1}{\varepsilon_0} \nabla \int_{v'} G(\mathbf{r}, \mathbf{r}') \rho_t(\mathbf{r}', t - \tau) \mathrm{d}V' \end{aligned} \tag{5.14}$$

By applying a Galerkin approach to Eq. (5.14), we obtain the PEEC formulation for a dielectric object, in which the circuital equivalence can be obtained as well as (5.6). Instead of the series resistance parameter, the *excess capacitance* C_n^+ can be gathered from (5.12) for a homogeneous and

isotropic dielectric:

$$\frac{1}{a_n}\int_{v_n}\frac{\hat{\mathbf{e}}_n}{(\varepsilon_r-1)\varepsilon_0}\cdot\int_{-\infty}^{t}\mathbf{J}_d(\mathbf{r},\tau)d\tau\,dV_n=\frac{1}{a_n}\frac{1}{(\varepsilon_r-1)\varepsilon_0}\int_{v_n}\frac{1}{a_n}\int_{-\infty}^{t}i_d(\mathbf{r},\tau)d\tau\,dV_n=$$
$$=\frac{1}{a_n}\frac{1}{(\varepsilon_r-1)\varepsilon_0}\frac{1}{a_n}\int_{v_n}dV_n\int_{-\infty}^{t}i_d(\mathbf{r},\tau)d\tau=\frac{1}{a_n}\frac{1}{(\varepsilon_r-1)\varepsilon_0}d_n\int_{-\infty}^{t}i_d(\mathbf{r},\tau)d\tau=$$
$$=\frac{1}{C_n^+}\int_{-\infty}^{t}i_d(\mathbf{r},\tau)d\tau$$

where

$$C_n^+=\frac{(\varepsilon_r-1)\varepsilon_0 a_n}{d_n} \tag{5.15}$$

is simply the parallel plate capacitance between the two end surfaces of volume v_n in the direction of the current flow, assuming a dielectric of permittivity (ε_r-1).

The final circuit for a dielectric current between two dielectric surface nodes is given in Fig. 5.3. It consists of the excess capacitance in series with an inductance which couples to all other parallel inductances. The two capacitive nodes couple to all other capacitive nodes, either on conductors or on other dielectric surfaces.

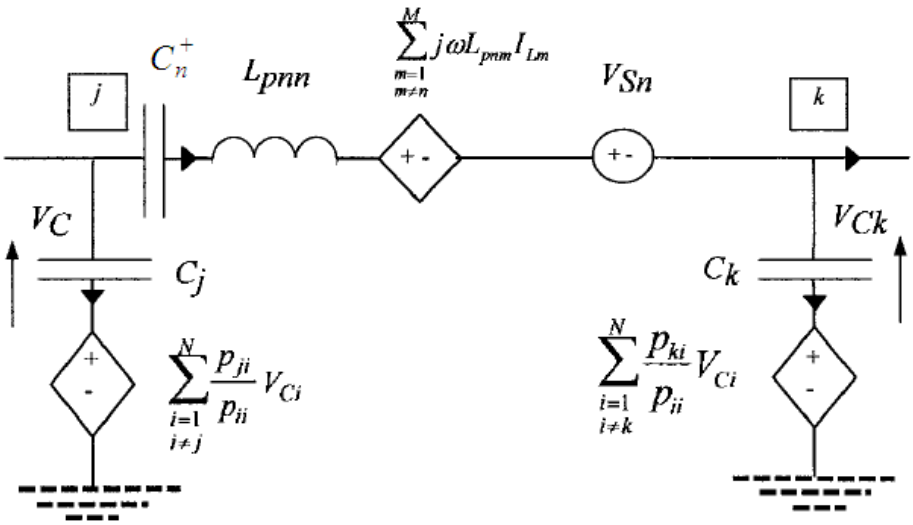

Fig. 5.3: Elementary PEEC dielectric cell between nodes j and k.

5.2.3 Retardation

The PEEC model described so far approximates a full-wave solution as long as the wavelength of the highest frequency of interest is much larger than the physical length of the longest coupling of interest. We include retardation by using

$$t_{ij} = \frac{\mid \mathbf{r_i} - \mathbf{r_j} \mid}{c}.$$

where $\mathbf{r_i}$, $\mathbf{r_j}$ are the center coordinate of cell i and j, respectively.

An immediate consequence of this inclusion is that the charges and potentials are taken at different time points.

$$\Phi_i(t) = \sum_{j=1}^{K} p_{ij} q_j(t - t_{ij}) \tag{5.16}$$

The retardation is approximated by the time of flight of an electromagnetic field between the center points of two cells (and is zero for the self terms). Due to the retardation it is impossible to solve (5.16) for q_j to get a capacitance equation. In other words, retarded circuits cannot be expressed in terms of capacitances and we must first find a circuit formulation that uses only coefficients of potential.

A single capacitance to the reference point at infinity is needed for each capacitive cell. We choose

$$C_i = \frac{1}{p_{ii}} \tag{5.17}$$

because this choice leads to a simplification of the dependent voltage source (see Fig. 5.2 and 5.3). Any other value for C_i would work as well and therefore we call it a *pseudocapacitance*. At any point, C_i will hold all the charge q_i stored on conductor i. The capacitance is therefore at the potential

$$\Phi_i^{'}(t) = p_{ii} q_i(t) \tag{5.18}$$

In order to get the correct potential Φ_i, we add a corrective voltage generator $u_i^C(t)$ to each conductor.

$$u_i^C(t) = \sum_{j \neq i}^{K} p_{ij} q_j(t - t_{ij}) = \sum_{j \neq i}^{K} \frac{p_{ij}}{p_{jj}} \Phi_j^{'}(t - t_{ij}) \tag{5.19}$$

We can derive a similar expression for replacing partial mutual inductances by a dependent voltage source $u_i^L(t)$ ($v_j^{'}(t)$ is the voltage over a partial auto inductance L_{jj}):

$$u_i^L(t) = \sum_{j \neq i}^{M} \frac{L_{ij}}{L_{jj}} v_j^{'}(t - t_{ij}) \tag{5.20}$$

5.3 PEEC Code Development

In this section a thorough and exhaustive description of the work carried out to develop the PEEC model is presented. It is worth emphasizing that the goal is to implement an original PEEC software, in order to have got a tool well adapted to any situation of interest (which excludes commercial tool). This entails numerical and programming issues that go far beyond the common use of the PEEC.

The description is focused on the techniques, problems and solutions adopted during the writing and validation phases of the code source. The code has been written using the Fortran 90 programming language and a great effort has been aimed at the computation efficiency and to reduce the computational time.

5.3.1 Meshing technique

The first step to create a PEEC model simulating electromagnetic couplings between large objects is the development of a suitable meshing algorithm.

As mentioned before, conductive and dielectric objects are discretized with two *intermeshing grids*, one referred to the volume cells, the other to the surface cells (in a similar way to the cell complexes in the Finite Integration Technique, [58]). Each volume (or inductive) cell is associated to a branch defined by two consecutive nodes, whereas each surface (or capacitive) cell is associated to a single node (Fig. 5.1).

In order to describe objects of any geometry, a meshing based on hexahedron and quadrilateral cells has been chosen.

The volume grid is made of a set of three different submeshes, one for each directions (local reference system (a, b, c)), with hexahedron-type cells. The surface grid is made of a mesh with quadrilateral-type cells, each of them covering one node.

In order to define an effective meshing algorithm, a *basic mesh* is detected in which the edges are associated with current paths, and all nodes represent terminals (to which impose continuity conditions), the superficial nodes are associated with capacitive coupling. To define easily the volumes surrounding each path and the surfaces around each capacitive node, a good strategy is to create a mesh in which the divisions along the three directions are double with respect to the basic mesh. Only nodes identified by three odd integer coordinates are capacitive nodes and terminals. The remaining nodes are used to detect volume and surface cells.

Figure 5.4 shows the global meshing of a hexahedral, non-orthogonal geometry, with three nodes in the $a-$direction and two nodes in both the $b-$

and $c-$directions. In this example, we obtain $3 \times 2 \times 2 = 12$ surface cells.

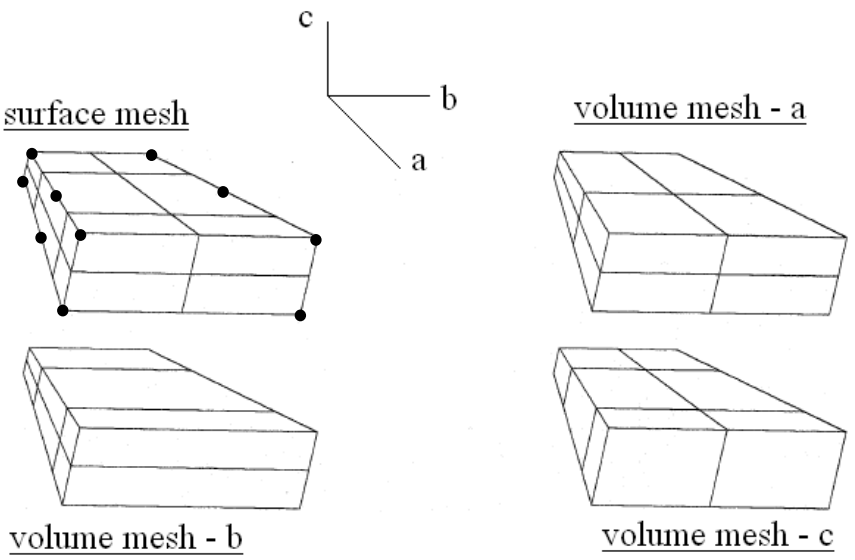

Fig. 5.4: Global PEEC meshing technique.

Since we detect a number of 8 branches in the $a-$direction, we define 8 volume cells along the $a-$axis. In a similar way, we detect a number of 6 branches in both the $b-$ and $c-$directions and thus we define 6 volume cells along the $b-$ and $c-$axis.

The above meshing approach allows to consider mutual inductive couplings among different axis, since in a non-orthogonal geometry the scalar product $\hat{\mathbf{e}}_n \cdot \hat{\mathbf{e}}_m$ $(n = a, b, c;\ m = a, b, c)$ in (5.9) is generally not equal to zero and thus an inductive coupling comes out.

Implementation of a global meshing technique requires to create a very large number of cells in all the three axis. Since most of the studied problems concern objects with a predominant geometric dimension with respect to the others, a favourite axis direction will be chosen in order to make the meshing generation process easy and light.

5.3.2 Partial parameter computation

The subsections below explain the approach used to solve the volume and superficial integrals (5.7), (5.8), (5.9) and (5.10). The main concern is addressed to the solution of double integrals in the computation of partial inductance and potential coefficient parameters. In fact, in the both cases a

strong computational effort and the singularity of the Green's function have to be faced.

For an orthogonal geometry, the calculation is quite simple, since many closed-form solutions can be found in literature, bypassing the singularity problem. For a non-orthogonal geometry, instead, the calculation has to be handled numerically. In this case, a *Gauss-Kronrod* numerical integration technique is adopted and an *isoparametric coordinate system* is used to handle the integration in a simpler way.

Isoparametric coordinate system

In order to describe elements with complex shapes, it easy to introduce the concept of *reference element*, with a simple geometric shape and defined in an adimensional space. The formulation is based on a one-to-one correspondence between an element with any shape described in a (x, y, z) cartesian system and an element with a simple shape described in a (ξ, η, ζ) *natural* (or *local*) system (Fig. 5.5). In fact:

$$\begin{aligned} x &= \sum_{i=1}^{N} n_i(\xi, \eta, \zeta) x_i \\ y &= \sum_{i=1}^{N} n_i(\xi, \eta, \zeta) y_i \\ z &= \sum_{i=1}^{N} n_i(\xi, \eta, \zeta) z_i \end{aligned} \tag{5.21}$$

where x_i, y_i, z_i are the cartesian coordinate of the N nodes of the element, n_i are the *shape functions* defined in the natural system (ξ, η, ζ) of the element. The shape functions are N as the number of element nodes and vary from 1 to 0. They are equal to 1 on the node i with coordinates (x_i, y_i, z_i) and equal to 0 on the other nodes of the element. The natural coordinates vary from -1 on one face to +1 on the opposite face, taking the value zero on the "median" face.

The hexahedron coordinates of the corners are:

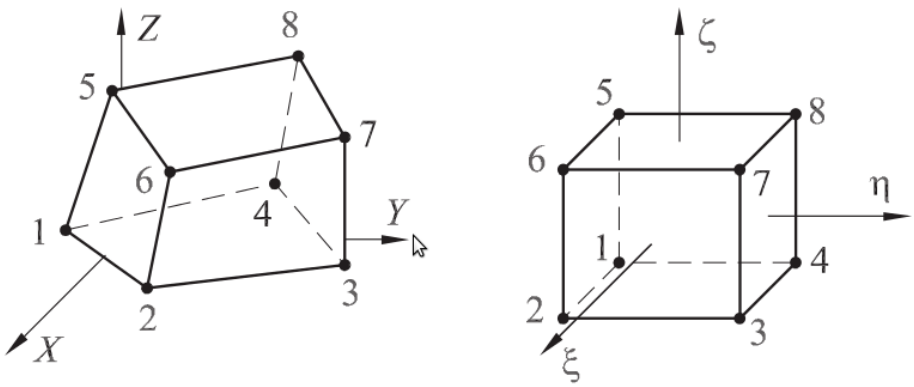

Fig. 5.5: The 8-node hexahedron and the natural coordinates (ξ, η, ζ).

Table 5.1

Node	ξ	η	ζ
1	-1	-1	-1
2	+1	-1	-1
3	+1	+1	-1
4	-1	+1	-1
5	-1	-1	+1
6	+1	-1	+1
7	+1	+1	+1
8	-1	+1	+1

The shape functions are:

$$
\begin{aligned}
n_1 &= \frac{1}{8}(1-\xi)(1-\eta)(1-\zeta) \quad & n_2 &= \frac{1}{8}(1+\xi)(1-\eta)(1-\zeta) \\
n_3 &= \frac{1}{8}(1+\xi)(1+\eta)(1-\zeta) \quad & n_4 &= \frac{1}{8}(1-\xi)(1+\eta)(1-\zeta) \\
n_5 &= \frac{1}{8}(1-\xi)(1-\eta)(1+\zeta) \quad & n_6 &= \frac{1}{8}(1+\xi)(1-\eta)(1+\zeta) \\
n_7 &= \frac{1}{8}(1+\xi)(1+\eta)(1+\zeta) \quad & n_8 &= \frac{1}{8}(1-\xi)(1+\eta)(1+\zeta)
\end{aligned}
\tag{5.22}
$$

These eight formulas can be summarized in a single expression as:

$$n_i = \frac{1}{8}(1 + \xi\xi_i)(1 + \eta\eta_i)(1 + \zeta\zeta_i) \tag{5.23}$$

where ξ_i, η_i, ζ_i denote the natural coordinates of the i-th node.

The Jacobian matrix of (x, y, z) with respect to (ξ, η, ζ) is:

$$\mathbf{J} = \frac{\partial(x, y, z)}{\partial(\xi, \eta, \zeta)} \tag{5.24}$$

Gauss-Kronrod integration method

The *Gauss–Kronrod* quadrature formula is a variant of the Gaussian quadrature, in which the evaluation points are chosen so that an accurate approximation can be computed by re-using the information produced by the computation of a less accurate approximation. It is an example of a *nested quadrature rule*. The difference between a Gauss quadrature rule and its Kronrod extension are often used as an estimate of the approximation error.

The problem in numerical integration is to approximate definite integrals of the form:

$$\int_V f(\tau)d\tau \tag{5.25}$$

Let us indicate as G_n the $n-$point Gauss formula:

$$G_n = \sum_{i=1}^{n} w_i f(\tau_i) \tag{5.26}$$

where w_i is the integration weight and $f(\tau_i)$ the function value at the observation point τ_i. This formula is exact for polynomials of order $2n - 1$, by considering n evaluation points. In order to evaluate the approximation error of (5.26), Alexander Kronrod (1965) has considered the following formula:

$$K_{2n+1} = \sum_{i=1}^{n} a_i f(x_i) + \sum_{j=1}^{n+1} b_j f(y_j) \tag{5.27}$$

that reuses the function values of (5.26). Kronrod has proven that it is possible to find $3n + 2$ parameters a_i, b_j, y_j so that (5.27) obtains a $3n + 1$ precision degree. The two formulas (G_n, K_{2n+1}) are called a Gauss-Kronrod couple. The computational effort is $2n + 1$ evaluations of the integrand function. The difference $\mid G_n - K_{2n+1} \mid$ is an error estimate of the integral (5.25) approximated by K_{2n+1}. The recommended error estimate is:

$$\mid \int_V f(\tau)d\tau - K_{2n+1}| \approx (200 \mid G_n - K_{2n+1} \mid)^{1.5} \tag{5.28}$$

The Gauss-Kronrod method is one of the most effective algorithms for the calculation of general integrals. For example, the calculation of $erf(1)$ provides:

$$G_7 = 0.842700792948824892; \quad K_{15} = 0.842700792949714861;$$

with $(200 \mid G_7 - K_{15} \mid)^{1.5} = 2 \cdot 10^{-15}$. The actual error of K_{15} is about $2 \cdot 10^{-17}$. In order to compare this result, it is worth referring to a 128 points trapezoidal rule, whose approximation error is about $4 \cdot 10^{-6}$.

Partial inductance parameter

In order to compute the partial inductance parameter, the Gauss-Kronrod integration method in natural coordinates is carried out. Starting with (5.9):

$$L_{nm} = \frac{\mu}{a_n a_m} \int_{v_n} \int_{v'_m} G(\mathbf{r}, \mathbf{r}') \hat{\mathbf{e}}_n \cdot \hat{\mathbf{e}}_m \mathrm{d}V'_m \mathrm{d}V_n$$

we define as N_{sou} and N_{obs} the number of Kronrod nodes for source v'_m and observation v_n inductive cells, where $N_{sou} = N_{s,\xi} \times N_{s,\eta} \times N_{s,\zeta}$ and $N_{obs} = N_{o,\xi} \times N_{o,\eta} \times N_{o,\zeta}$. The unit vectors $\hat{\mathbf{e}}_m$ and $\hat{\mathbf{e}}_n$ are defined along the ζ direction, that is supposed the prevalent direction of the density current vector in each volume cell.

The numerical integration becomes:

$$L_{nm} = \mu \left[\sum_{i=1}^{N_{o,\xi}} \sum_{j=1}^{N_{o,\eta}} \sum_{k=1}^{N_{o,\zeta}} \frac{\hat{\mathbf{e}}_n}{a_k} \cdot \left(\sum_{r=1}^{N_{s,\xi}} \sum_{t=1}^{N_{s,\eta}} \sum_{q=1}^{N_{s,\zeta}} G(\mathbf{r}_{ijk}, \mathbf{r}_{rtq}) \frac{\hat{\mathbf{e}}_m}{a_q} w_{s,rtq} J_{s,rtq} \right) w_{o,ijk} J_{o,ijk} \right] \tag{5.29}$$

where $w_{o,ijk}$, $J_{o,ijk}$ and $w_{s,rtq}$, $J_{s,rtq}$ are the integration weight and the determinant of the Jacobian matrix for the observation and source cells, respectively.

The computational effort to solve Eq. (5.29) is very high, as far as the quadrature rule for a double volume integral is concerned. Thus, we search for a strategy to both lower the computational weight and maintain a satisfactory numerical efficiency. From here on, the complete calculation (5.29) is referred to as *volume-volume* integration (VV) technique.

The first attempt to speed up the integration is the reduction of the external volume integral to a line integral. That is:

$$L_{nm} = \mu \left[\sum_{k=1}^{N_{o,\zeta}} \frac{\hat{\mathbf{e}}_n}{a_k} \cdot \left(\sum_{r=1}^{N_{s,\xi}} \sum_{t=1}^{N_{s,\eta}} \sum_{q=1}^{N_{s,\zeta}} G(\mathbf{r}_{ijk}, \mathbf{r}_{rtq}) \frac{\hat{\mathbf{e}}_m}{a_q} w_{s,rtq} J_{s,rtq} \right) w_{o,k} J_{o,k} \right] \tag{5.30}$$

where $J_{o,k}$ indicates the determinant of the linear Jacobian. The *line-volume* integration (LV) is very efficient for those cells whose distance is in the order of over 3 times the largest cell dimension. Instead, an accurate results can not be obtained for the auto-inductance calculation and the mutual-inductance between near cells, because the number of nodes for the external integral is not sufficient to accomplish the required goal.

The second attempt is addressed to the *surface/line-volume* integration (SLV), where the external volume integral is factorized into a surface and a line integrals:

$$L_{nm} = \mu \left\{ \sum_{k=1}^{N_{o,\zeta}} \frac{w_{o,k} J_{o,k}}{a_k} \left[\sum_{i=1}^{N_{o,\xi}} \sum_{j=1}^{N_{o,\eta}} w_{o,ij} J_{o,ij} \hat{\mathbf{e}}_n \cdot \left(\sum_{r=1}^{N_{s,\xi}} \sum_{t=1}^{N_{s,\eta}} \sum_{q=1}^{N_{s,\zeta}} G(\mathbf{r}_{ijk}, \mathbf{r}_{rtq}) \frac{\hat{\mathbf{e}}_m}{a_q} w_{s,rtq} J_{s,rtq} \right) \right] \right\} \tag{5.31}$$

where $J_{o,ij}$ is the determinant of the surface Jacobian. It can be shown in the tables below that this solution achieves the best results in terms of numerical accuracy and computational speed.

The validation and comparison of the formula (5.29), (5.30), (5.31) is mainly carried out by referring to analytical formula in literature. With regard to the auto-inductance, the validation procedure is made by comparison with Eq. (15) in [59], where a closed-form formula is proposed for rectangular conductors. Table (5.2) shows the best approximated results obtained with the three approach presented above and the percentage deviation with respect to the analytical one (AN). The integration on the source cell is made with a progressive number of nodes N_{sou} until the integral reduces under a specified numerical tolerance ($1 \cdot 10^{-3}$). The result obtained with

Table 5.2: Auto-inductance comparison. The rectangular conductor has dimensions $1 \times 1 \times 12$ cm. The inductance values are expressed in henry (H).

AN	**VV**	$\frac{VV}{AN}\%$	**LV**	$\frac{LV}{AN}\%$	**SLV**	$\frac{SLV}{AN}\%$
7.2624e-8	7.3220e-8	0.82	7.8351e-8	7.88	7.3282e-8	0.90

the VV-technique presents the most accurate value, as expected. It has to be considered that a number $N_{obs} = 63^3$ of nodes is used to get a very low percentage deviation, but a $N_{obs} = 567$ used in the SLV-technique allows to reduce strongly the computational time and obtain a very satisfactory result. As regards the LV-technique value, it is obtained with $N_{obs} = 126$, but the accuracy is extremely low.

If the geometrical dimensions of the rectangular conductor are changed (Tab. 5.3), the results support much more the considerations above.

Table 5.3: Auto-inductance comparison. The rectangular conductor has dimensions $1 \times 1 \times 4$ cm. The inductance values are expressed in henry (H).

AN	**VV** (N_{obs})	$\frac{VV}{AN}\%$	**SLV** (N_{obs})	$\frac{SLV}{AN}\%$
1.6078e-8	1.6106e-8 (**3375**)	0.17	1.6106e-8 (**343**)	0.17

In the VV- and SLV-techniques, the singularity of the Green's function is overcome by subdividing the source cell in four further volumes, so that the Kronrod nodes in the source and observation cells do not coincide during the whole integration procedure.

As far as the mutual inductance is concerned, the validation is carried out by comparing the numerical results with two examples proposed in [59]. Ruehli obtained the mutual inductance value through a filamentary approach, in which a massive conductor is approximated by a finite number of filaments, whose coupling is computed with a closed-form solution. Tables (5.4) and (5.5) show the comparison of the reference value (*Fil*) with that obtained through the LV and SLV-techniques, for the two cases in Fig. 5.6 and 5.7, respectively.

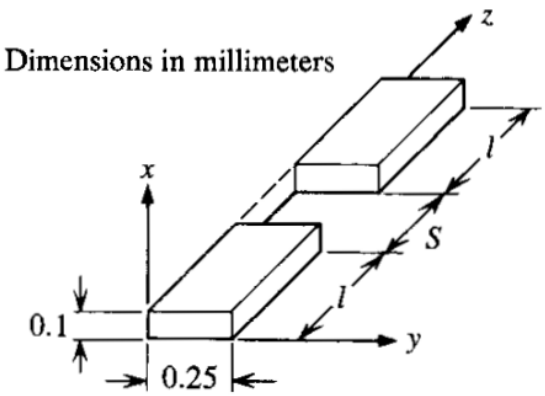

Fig. 5.6: Mutual inductance between two cells in the same plane.

So far, the validation process has been carried out by referring to parallelepiped (*orthogonal*) geometries. In order to derive more reliable considerations on the numerical accuracy, a validation test is performed with hexahedal (*non-orthogonal*) geometries.

Since the auto-inductance calculation is a tricky problem due to the singularity of the Green's function, a great attention is directed to the numerical validation of the auto-inductance parameter for non-orthogonal (NO) cells.

Table 5.4: Mutual-inductance comparison. The reference value is obtained with 2 filaments in x direction and 5 filaments in y direction. The inductance values are expressed in henry (H).

	Fil	**SLV** ($N_{obs} = 567$)	**LV** ($N_{obs} = 630$)
$\ell = 1$ mm, $S = 0.1$ mm	1.097e-10	1.097e-10	1.11e-10
$\ell = 1$ mm, $S = 10$ mm	0.091e-10	0.091e-10	0.091e-10

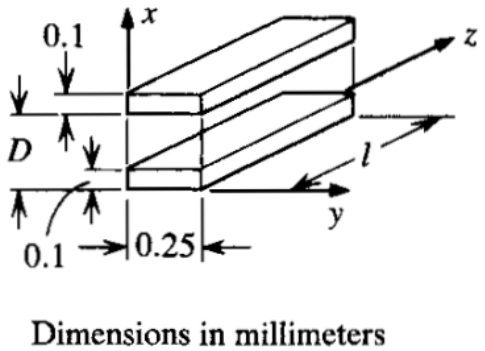

Fig. 5.7: Mutual inductance between two parallel cells.

Table 5.5: Mutual-inductance comparison. The reference value is obtained with 2 filaments in x direction and 5 filaments in y direction. The inductance values are expressed in henry (H).

	Fil	**SLV** ($N_{obs} = 567$)	**LV** ($N_{obs} = 630$)
$\ell = 1$ mm, $D = 1$ mm	0.931e-10	0.931e-10	0.908e-10
$\ell = 1$ mm, $D = 5$ mm	0.199e-10	0.199e-10	0.199e-10

Two truncated pyramidal cells are used and the related result comparison with the reference value (*Fil*) is shown in Table (5.6).

On the basis of these results, it can be discerned that the SLV approach fulfils our requirements, in terms of good accuracy and reasonable computational time.

As a full partial inductance matrix has to be computed, a great effort is made to reduce the execution time of the entire matrix evaluation. To this end, the following items are developed:

Table 5.6: Auto-inductance comparison for two non-orthogonal cells. The reference value is obtained with 20 filaments in x direction and 20 filaments in y direction. The inductance values are expressed in henry (H).

	Fil	**SLV** ($N_{obs} = 567$)	**VV** ($N_{obs} = 3375$)
NO cell 1	0.174e-7	0.186e-7	0.185e-7
NO cell 2	0.168e-7	0.175e-7	0.171e-7

- ⇝ Only the upper (or lower) triangular part of the matrix is computed, thanks to its symmetrical property. The matrix symmetry is guaranteed by the reciprocity theorem.
- ⇝ The auto-inductance of those cells having similar geometrical shape and dimensions (difference under a fixed small tolerance) is computed one time for all.
- ⇝ The auto-inductance of orthogonal cells are computed analytically, according to Eq. (15) in [59].

Otherwise, the calculation is carried out numerically by adopting the SLV-technique. The Kronrod order for the source and observation cells is chosen by the user according to the problem geometry and the required accuracy.

Potential coefficient parameter

In order to compute the potential coefficient parameter, the Gauss-Kronrod integration method in natural coordinates is carried out. Starting with (5.10):

$$p_{nm} = \frac{1}{\varepsilon_0 \Sigma_n \Sigma_m} \int_{s_n} \int_{s'_m} G(\mathbf{r}, \mathbf{r}') \mathrm{d}S'_m \mathrm{d}S_n$$

the numerical integration becomes:

$$p_{nm} = \frac{1}{\varepsilon_0} \sum_{i=1}^{N_{o,\xi}} \sum_{j=1}^{N_{o,\eta}} \frac{1}{\Sigma_n} \left(\sum_{r=1}^{N_{s,\xi}} \sum_{t=1}^{N_{s,\eta}} \frac{1}{\Sigma_m} G(\mathbf{r}_{ij}, \mathbf{r}_{rt}) w_{s,rt} J_{s,rt} \right) w_{o,ij} J_{o,ij} \qquad (5.32)$$

where $w_{s,rt}, J_{s,rt}$ and $w_{o,ij}, J_{o,ij}$ are the superficial Kronrod weights and Jacobian determinants for the source and observation capacitive cells. $N_{sou} = N_{s,\xi} \times N_{s,\eta}$ and $N_{obs} = N_{o,\xi} \times N_{o,\eta}$ are the total number of Kronrod nodes.

In a similar way to the partial inductance computation techniques, a LLS-technique is developed and used. The internal integration is performed as

a superficial integration, whereas the external one is factorized in two line integrations (5.33).

$$p_{nm} = \frac{1}{\varepsilon_0} \sum_{i=1}^{N_{o,\xi}} w_{o,i} J_{o,i} \sum_{j=1}^{N_{o,\eta}} \frac{w_{o,j} J_{o,j}}{\Sigma_n} \left(\sum_{r=1}^{N_{s,\xi}} \sum_{t=1}^{N_{s,\eta}} \frac{1}{\Sigma_m} G(\mathbf{r}_{ij}, \mathbf{r}_{rt}) w_{s,rt} J_{s,rt} \right) \quad (5.33)$$

The validation process follows a scheme similar to that used for the partial inductance calculation. The numerical results are compared with the analytical formula proposed by Ruehli and Brennan in [60]. The comparison is carried out by referring to the examples in Figg. 5.8, 5.9 and 5.10, where the mutual potential coefficient is evaluated for cells oriented in parallel and perpendicular and the auto potential coefficient is calculated for a thin square plate.

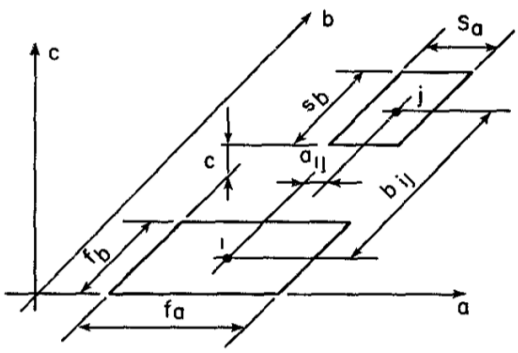

Fig. 5.8: Mutual potential coefficient between cells oriented in parallel.

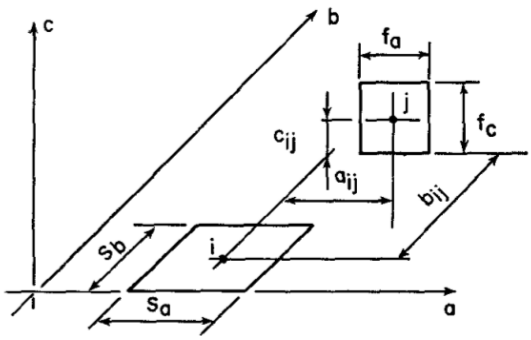

Fig. 5.9: Mutual potential coefficient between cells oriented perpendicular to each other.

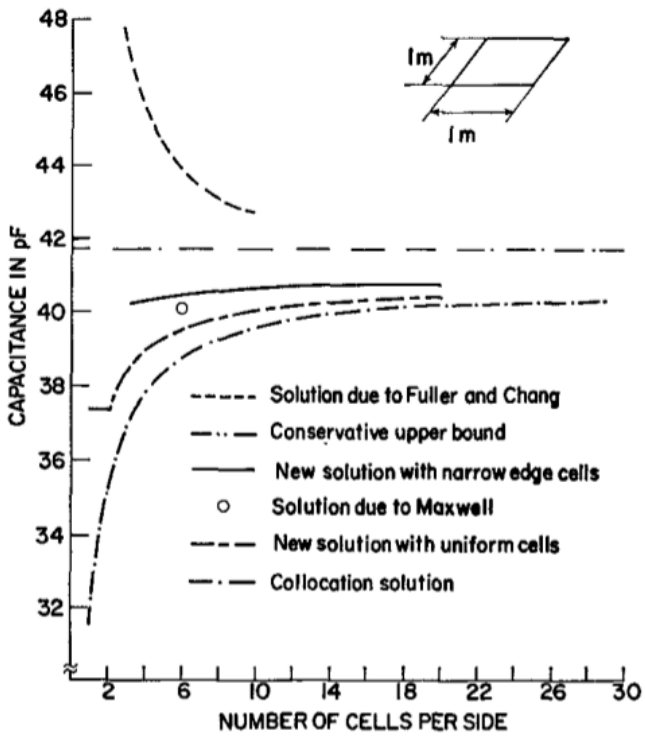

Fig. 5.10: Auto potential coefficient of a thin square plate.

For the all three example cases the numerical results deviate from the reference values of less than 0.1%. As above, the singularity of the Green's function is overcome again by subdividing the source cell in four further quadrilaterals, in order to avoid the superimposition of the Kronrod nodes in the source and observation cells.

Series resistance parameter

The series resistance parameter is evaluated according to Eq. (5.8)

$$R_n = \int_{v_n} \frac{\mathrm{d}V_n}{\sigma a_n^2}$$

and the numerical computation is:

$$R_n = \sum_{i=1}^{N_{o,\xi}} \sum_{j=1}^{N_{o,\eta}} \sum_{k=1}^{N_{o,\zeta}} \frac{1}{\sigma a_n^2} w_{ijk} J_{ijk} \tag{5.34}$$

where w_{ijk}, J_{ijk} are the Kronrod volume weights and the Jacobian determinant and σ the electrical conductivity of the conductive cell.

Since Eq. (5.34) can be seen as a part of Eq. (5.31), the resistance value is calculated during the partial inductance evaluation process and then the related computational effort is reduced a lot.

External voltage generator

The external field contribution is taken into account by Eq. (5.7)

$$V_{sn} = \frac{1}{a_n} \int_{v_n} \hat{\mathbf{e}}_n \cdot \mathbf{E}^{(i)}(\mathbf{r}, t) \mathrm{d}V_n$$

The integration is handled numerically through the Kronrod quadrature rule, that is:

$$V_{sn} = \sum_{i=1}^{N_{o,\xi}} \sum_{j=1}^{N_{o,\eta}} \sum_{k=1}^{N_{o,\zeta}} \frac{\hat{\mathbf{e}}_n}{a_n} \cdot \mathbf{E}^{(i)}(\mathbf{r}_{ijk}, t) w_{ijk} J_{ijk} \tag{5.35}$$

On the basis of electric field values obtained from measurements or further computations is possible to calculate the independent voltage generator in the PEEC basic circuit by means of Eq. (5.35).

5.3.3 Numerical solver

The PEEC approach is suitable to solve electromagnetic problems both in time and frequency domain.

In order to solve complex and varied problems, the first attempt is to deal with the simplest example of electric circuit, made by the series of circuital lumped elements and objects to be discretized (Fig. 5.11).

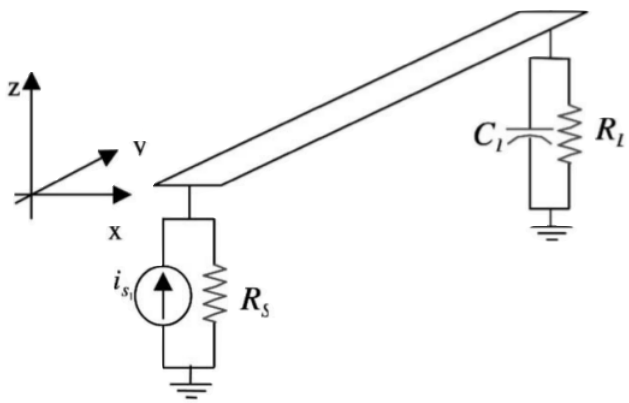

Fig. 5.11: Example of simple electric circuit.

The goal of this section is to present the method to build the entire linear system, i.e. the system matrix and the right-hand side array, together with the numerical solver to be used.

With regard to the basic cell circuit of Fig. 5.2, the PEEC equations are developed in the frequency-domain. Starting with the equations for the $n-$cell:

$$\begin{cases} v_j - v_k - R_n i_{Ln} - j\omega L p_{nn} i_{Ln} - \sum_{m=1,m\neq n}^{M} j\omega L p_{nm} i_{Lm} = V_{sn} \\ j\omega c_k v_{ck} - i_{Ln} + i_{Ln+1} = 0 \\ -v_k + v_{ck} + \sum_{i=1,i\neq k}^{Q} \dfrac{p_{ki}}{p_{ii}} v_{ci} = 0 \end{cases} \tag{5.36}$$

and being M the number of inductive cells and Q the number of potential cells, the following quantities are defined:

- ◇ $L_p \in \mathbb{R}^{M\times M}$ is the partial inductance matrix.
- ◇ $P \in \mathbb{R}^{Q\times Q}$ is the potential coefficient matrix.
- ◇ $R \in \mathbb{R}^{M\times M}$ is the diagonal resistance matrix.
- ◇ $v \in \mathbb{R}^{Q\times 1}$ is the node potential array.
- ◇ $i_L \in \mathbb{R}^{M\times 1}$ is the cell current array.
- ◇ $v_{SE} \in \mathbb{R}^{M\times 1}$ is the external voltage generator array.
- ◇ $v_c \in \mathbb{R}^{Q\times 1}$ is the voltage array across the pseudocapacitances.
- ◇ $C_d \in \mathbb{R}^{Q\times Q}$ is the diagonal pseudocapacitance matrix.
- ◇ $A \in \mathbb{R}^{M\times Q}$ is the connectivity matrix, where the element $a_{ij} = +1$ if the current arrow i points towards node j, $a_{ij} = -1$ if the current arrow i points away from node j and $a_{ij} = 0$ if node i and node j are not connected.
- ◇ $T \in \mathbb{R}^{Q\times Q}$ is a matrix whose elements $t_{ij} = \frac{p_{ij}}{p_{ii}}$.
- ◇ $\Pi \in \mathbb{R}^{M\times M}$ is the identity matrix.

The equation system (5.36) written in a matrix form becomes:

$$\begin{cases} Av - Ri_L - j\omega L_p i_L = v_{SE} \\ j\omega C_d v_c + A^t i_L = 0 \\ -v + Tv_c = 0 \end{cases} \tag{5.37}$$

where A^t is the transpose matrix of A. In order to solve the example in Fig. 5.11, the system (5.37) has to be completed with boundary conditions, represented by the Kirchhoff laws at the source and load node terminals.

To this end, each lumped circuital element is managed as a voltage source, that is the series of an ideal voltage source and its internal impedance. In this way, a source, a resistance, an inductance and a capacitance can be modelled by the same bipole, by modifying the real and imaginary parts. The only exception is the ideal current source that is managed separately. A current source, i.e. the parallel of an ideal current source and a conductance, is worth being converted into a voltage source.

In order to form the global solution matrix, the following approach is taken into account:

- Each object is preceded and followed by a lumped circuital elements.
- The unknown quantities related to an object are: a number of currents equal to the number of inductive cells + two currents inwards and outwards the object; a number of potentials equal to the number of nodes and a number of capacitive voltages equal to the number of superficial nodes.
- The unknown quantities related to a circuital element are one current and two potentials.

As final stage, the entire complex linear system:

$$\Upsilon x = \beta \rightarrow x = \Upsilon^{-1}\beta$$

where Υ is the system matrix, β the right-side vector and x the unknown array, is solved by the Gauss elimination method.

The circuital example of Fig. 5.11 is solved for several operating frequencies in sinusoidal steady-state behaviour and an optimal agreement with analytical results is obtained.

In order to deal with time-varying electromagnetic and circuital problems, a *step-by-step* procedure solution is developed.

As the derivative function $\frac{dx}{dt}$ can be approximated by the incremental ratio:

$$\frac{dx}{dt} = \frac{x(t_n) - x(t_{n-1})}{h} \tag{5.38}$$

where $h = (t_n - t_{n-1})$ is the difference between two samples t_n and t_{n-1}, the derivative function can also be expressed through the linear combination:

$$\frac{dx}{dt} = (1 - \Theta)\frac{dx}{dt}|_{t_{n-1}} + \Theta\frac{dx}{dt}|_{t_n} \tag{5.39}$$

The parameter Θ is the weight of the linear combination, whose value has given rise in literature to several numerical methods for solution of differential equations. The most wide-spread parameter values are: $\Theta = 0$ (*Eulero Forward*), $\Theta = 1$ (*Eulero Backward*) and $\Theta = \frac{1}{2}$ (*Crank-Nicholson*). Due to stability issues, a reasonable Θ would be $\frac{1}{2} < \Theta < 1$ and the optimal value $\Theta = \frac{2}{3}$ is usually set.

According to Eq. (5.38) and (5.39), the following equality is written:

$$x(t_n) - x(t_{n-1}) = h(1-\Theta)\frac{dx}{dt}|_{t_{n-1}} + h\Theta\frac{dx}{dt}|_{t_n}$$

and the unknown value $x(t_n)$ can be expressed as a function of the previous value $x(t_{n-1})$, as:

$$x(t_n) = x(t_{n-1}) + h(1-\Theta)\frac{dx}{dt}|_{t_{n-1}} + h\Theta\frac{dx}{dt}|_{t_n} \tag{5.40}$$

In a similar way as Eq. (5.36), the PEEC equations are developed in time-domain. Starting with the equations for the $n-$cell:

$$\begin{cases} v_j - v_k - R_n i_{Ln} - Lp_{nn}\dfrac{di_{Ln}}{dt} - \sum_{m=1,m\neq n}^{M} Lp_{nm}\dfrac{di_{Lm}}{dt} = V_{sn} \\ c_k\dfrac{dv_{ck}}{dt} - i_{Ln} + i_{Ln+1} = 0 \\ -v_k + v_{ck} + \sum_{i=1,i\neq k}^{Q}\dfrac{p_{ki}}{p_{ii}}v_{ci} = 0 \end{cases} \tag{5.41}$$

The equation system (5.41), written in a matrix form, becomes:

$$\begin{cases} Av - Ri_L - L_p\dfrac{di_L}{dt} = v_{SE} \\ C_d\dfrac{dv_c}{dt} + A^t i_L = 0 \\ -v + Tv_c = 0 \end{cases} \tag{5.42}$$

Equation system (5.42) is a differential equation system, where the unknowns are $(v \quad i_L \quad v_c)^t$. The differential operators can be handled by means of (5.39). Then,

$$\frac{dv_c}{dt} = -C_d^{-1}A^t i_L$$

is written as:

$$v_c(t_n) - v_c(t_{n-1}) = h(1-\Theta)\left[-C_d^{-1}A^t i_L(t_{n-1})\right] + h\Theta\left[-C_d^{-1}A^t i_L(t_n)\right]$$

The variable v_c at time sample t_n is:

$$v_c(t_n) = v_c(t_{n-1}) + h(1-\Theta)\left[-C_d^{-1}A^t i_L(t_{n-1})\right] + h\Theta\left[-C_d^{-1}A^t i_L(t_n)\right] \tag{5.43}$$

v_c is a function of quantity $i_L(t_n)$, that is unknown at the nth iteration.

In a similar way, the second differential equation:

$$\frac{di_L}{dt} = L_p^{-1}\left(Av - Ri_L - v_{SE}\right)$$

is approximated by:

$$\begin{aligned} i_L(t_n) - i_L(t_{n-1}) = h(1-\Theta)L_p^{-1}[Av(t_{n-1}) - Ri_L(t_{n-1}) - v_{SE}(t_{n-1})] + h\Theta L_p^{-1}[Av(t_n) + \\ - Ri_L(t_n) - v_{SE}(t_n)] \end{aligned}$$

The variable i_L at time sample t_n is:

$$\begin{aligned} i_L(t_n) + h\Theta L_p^{-1}Ri_L(t_n) = i_L(t_{n-1}) - h(1-\Theta)L_p^{-1}Ri_L(t_{n-1}) + \\ + h(1-\Theta)L_p^{-1}Av(t_{n-1}) - h(1-\Theta)L_p^{-1}v_{SE}(t_{n-1})] + \\ + h\Theta L_p^{-1}Av(t_n) - h\Theta L_p^{-1}v_{SE}(t_n) \end{aligned} \tag{5.44}$$

i_L is a function of quantity $v(t_n)$, that is unknown during the iteration n.

Being $v = Tv_c$, Eq. (5.43) is re-written as follows:

$$v(t_n) = v(t_{n-1}) - h(1-\Theta)TC_d^{-1}A^t i_L(t_{n-1}) - h\Theta TC_d^{-1}A^t i_L(t_n) \tag{5.45}$$

By substituting Eq. (5.45) in Eq. (5.44):

$$\begin{aligned} i_L(t_n) + h\Theta L_p^{-1}Ri_L(t_n) = i_L(t_{n-1}) - h(1-\Theta)L_p^{-1}Ri_L(t_{n-1}) + \\ + h(1-\Theta)L_p^{-1}Av(t_{n-1}) - h(1-\Theta)L_p^{-1}v_{SE}(t_{n-1}) + \\ + h\Theta L_p^{-1}A[v(t_{n-1}) - h(1-\Theta)TC_d^{-1}A^t i_L(t_{n-1}) - h\Theta TC_d^{-1}A^t i_L(t_n)] + \\ - h\Theta L_p^{-1}v_{SE}(t_n) \end{aligned} \tag{5.46}$$

In this equation the only unknown quantity is $i_L(t_n)$. In other words $i_L(t_n)$ depends only on $i_L(t_{n-1})$, $v(t_{n-1})$, $v_{SE}(t_{n-1})$ and $v_{SE}(t_n)$, that have been already calculated.

In order to make clearer (5.46), the following matrices are defined:

$$Q = L_p^{-1}R; \quad S = L_p^{-1}APA^t; \quad F = L_p^{-1}A; \quad D = PA^t$$

and the formal expression for $i_L(t_n)$ becomes:

$$\begin{aligned} i_L(t_n)[\Pi + h\Theta Q + h^2\Theta^2 S] = i_L(t_{n-1})[\Pi - h(1-\Theta)Q + \\ - h^2\Theta(1-\Theta)S] + v(t_{n-1})[h(1-\Theta)F + h\Theta F] + \\ - h(1-\Theta)L_p^{-1}v_{SE}(t_{n-1}) - h\Theta L_p^{-1}v_{SE}(t_n) \end{aligned} \tag{5.47}$$

Once the value of i_L is known at time t_n, the node potential v at the same time is:

$$v(t_n) = v(t_{n-1}) - h(1-\Theta)Di_L(t_{n-1}) - h\Theta Di_L(t_n) \tag{5.48}$$

The value of $v(t_n)$ allows to compute $v_c(t_n)$ through $v_c(t_n) = T^{-1}v(t_n)$.

When all variables are calculated at sample t_n, the following iteration $(n+1)$ is able to begin from (5.47) and thereon.

Matrices in (5.47) and (5.48) have to be calculated once and the approach step-by-step allows to handle time-varying problems in a feasible way.

One of the most relevant efforts in the PEEC method is represented by the skin effect: the numerical results are reliable until the cross-section dimension is small enough with respect to the penetration depth. Otherwise, an accurate dedicated approach is necessary (see [1], [61], [62]).

5.4 Future Developments and Applications

The future developments of the present PEEC model are going to allow a great variety of applications. In order to do that, the following improvements are scheduled:

- Generation of circular and helicoidal objects;
- Introduction of dielectric volume cells and calculation of the excess capacitance parameter;
- Introduction of the propagation effects both in time and frequency domain;
- Development of the images method.

The above enhancements allow to use the PEEC model to study Rogowski probes for high frequency and transient current applications with a considerable accuracy. They can be able to simulate also the calibration test environment for the ESD generators, by improving the approximated analysis of transmission line model (§ 4.5) and fulfil a hybrid numerical-experimental calibration approach.

Bibliography

[1] S. V. Kochetov, "Time- and frequency-domain modeling of passive interconnection structures in field and circuit analysis," Ph.D. dissertation, Res Electricae Magdeburgenses, 2008.

[2] J. D. Ramboz, "Machinable rogowski coil, design, and calibration," *IEEE Trans. Instrum. Meas.*, vol. 45, pp. 511–515, Apr. 1996.

[3] M. Bombonato and D. D'Amore, "A classical device for the modern measurements: The rogowski coil," "un componente classico per le misure moderne: la bobina di rogowski," *L'Elettrotecnica*, vol. LXXVI, pp. 765–771, Sep. 1989.

[4] D. A. Ward, J. La, and T. Exon, "Using rogowski coils for transient current measurements," *Eng. Sci. Educ. J.*, vol. 2, pp. 105–113, Jun. 1993.

[5] M. Argueso, G. Robles, and J. Sanz, "Implementation of a rogowski coil for the measurement of partial discharges," *Rev. Sci. Instrum.*, vol. 76, pp. 1–7, Jun. 2005.

[6] L. A. Kojovic, "Rogowski coils suit relay protection and measurement," *IEEE Comput. Appl. Power*, vol. 10, pp. 47–52, Jul. 1997.

[7] D. E. Destefan, "Calibration and testing facility for resistance welding current monitors," *IEEE Trans. Instrum. Meas.*, vol. 45, pp. 453–456, Apr. 1996.

[8] K.-W. Lee, J.-N. Park, S.-H. Kang, Y.-S. Lee, G.-H. Ham, Y.-M. Jang, and K.-J. Lim, "Geometrical effects in the current measurement by rogowski sensor," in *Proc. ISEIM*, Himeji, Japan, Nov. 2001, pp. 419–422.

[9] Y. Chekurov and J. Hällström, "Influence of busbar geometry on ac current measurement using rogowski coil," in *Proc. Dig. Precision Electromagn. Meas. Conf.*, Broomfield, USA, Jun. 2008, pp. 542–543.

[10] K. Draxler and R. Styblikova, "Determination of rogowski coil constant," in *Proc. Appl. Electron.*, Pilsen, Czech Republic, Sep. 2006, pp. 241–243.

[11] G. Xiaohua, L. Jingsheng, Z. Mingjun, and Y. Miaoyuan, "Improved performance rogowski coils for power system," in *Proc. Transmiss. Distrib. Conf. Expo.*, Dallas, USA, Sep. 2003, pp. 371–374.

[12] J. D. Ramboz, D. E. Destefan, and R. S. Stant, "The verification of rogowski coil linearity from 200 a to greater than 100 ka using ratio methods," in *Proc. IEEE Instrum. Meas. Technol.*, Anchorage, Alaska, May 2002, pp. 687–692.

[13] M. Faifer and R. Ottoboni, "An electronic current transformer based on rogowski coil," in *Proc. IEEE Instrum. Meas. Technol.*, Victoria, Canada, May 2008, pp. 1554–1559.

[14] J. Hlavacek, R. Prochazka, K. Draxler, and V. Kvasnicka, "The rogowski coil design software," in *Proc. 16th IMEKO TC4 Int. Symp.*, Firenze, Italy, Sep. 2008, pp. 295–300.

[15] G. Beccherini, S. D. Fraia, M. Marracci, B. Tellini, C. Zappacosta, and G. Robles, "Critical parameters for mutual inductance between rogowski coil and primary conductor," in *Proc. 12MTC*, Singapore, May 2009, pp. 432–436.

[16] L. Ferkovic, D. Ilic, and R. Malaric, "Mutual inductance of a precise rogowski coil in dependence of the position of primary conductor," *IEEE Trans. Instrum. Meas.*, vol. 58, pp. 122–128, Jan. 2009.

[17] M. Rezaee and H. Heydari, "Mutual inductances comparison in rogowski coil with circular and rectangular cross-sections and its improvement," in *Proc. 3rd IEEE Conf. Ind. Electron. Appl. Conf.*, Singapore, Jun. 2008, pp. 1507–1511.

[18] J. Letosa, J. S. Artal, M. Samplon, A. Uson, and F. J. Arcega, "Modelization of current sensors by finite elements method," *Measurement*, vol. 35, pp. 233–241, Apr. 2004.

[19] Q. Chen, H. Li, M. Zhang, and Y. Liu, "Design and characteristics of two rogowski coils based on printed circuit board," *IEEE Trans. Instrum. Meas.*, vol. 55, pp. 939–943, Jun. 2006.

[20] C. D. M. Oates, A. J. Burnett, and C. James, "The design of high performance rogowski coils," in *Proc. Power Electron., Mach. Drives Conf.*, Bath, U.K., Apr. 2002, pp. 568–572.

[21] O. Bottauscio, M. Chiampi, and D. Chiarabaglio, "Magnetic flux distribution and losses in narrow ferromagnetic strips," *J. Magn. Magn. Mater.*, vol. 215/216, pp. 46–48, Jun. 2000.

[22] *Supplement 1 to the Guide to the Expression of Uncertainty in Measurement–Propagation of Distributions Using a Monte Carlo Method*, Joint Committees for Guides in Metrology, 2008.

[23] *Electrostatics-Part 5-1: Protection of electronic devices from electrostatic phenomena-General requirements*, IEC Std. 61 340-5-1, 2007.

[24] *EMC Directive 2004/108/EC*, European Commission, 2004.

[25] M. Borsero, S. Caniggia, A. Sona, M. Stellini, and A. Zuccato, "A new proposal for the uncertainty evaluation and reduction in air electrostatic discharge tests," in *Proc. Int. Symp. on EMC*, Hamburg, Germany, Sep. 2008, pp. 1–6.

[26] R. Chundru, D. Pommerenke, K. Wang, T. Van Doren, F. Centola, and J. Huang, "Characterization of human metal ESD reference discharge event and correlation of generator parameters to failure levels-part 1: Reference event," *IEEE Trans. Electromagn. Compat.*, vol. 46, pp. 498–504, Nov. 2004.

[27] J. Huang, D. Pommerenke, and W. Huang, "Problems with the electrostatic discharge (ESD) immunity test in electromagnetic compatibility (EMC)," in *Proc. Asia-Pacific Conf. on Env. Electromag.*, Hangzhou, China, Nov. 2003, pp. 251–254.

[28] S. Caniggia and F. Maradei, "Circuit and numerical modeling of electrostatic discharge generators," *IEEE Trans. Ind. Appl.*, vol. 42, pp. 1350–1357, Dec. 2006.

[29] K. Wang, D. Pommerenke, R. Chundru, T. Van Doren, J. L. Drewniak, and A. Shashindranath, "Numerical modeling of electrostatic discharge generators," *IEEE Trans. Electromagn. Compat.*, vol. 45, pp. 258–271, May 2003.

[30] J. Kumar, S. Nagesh, P. K. Mishra, N. D. Ghatpande, and T. Dhanabalan, "Study and modeling of electrostatic discharge (ESD) simulator," in *Proc. Int. Conf. on Electromag. Interf. and Comp.*, Bangalore, India, Nov. 2008, pp. 199–204.

[31] A. Morando, M. Borsero, A. Sardi, and G. Vizio, "Modeling and practical suggestions to improve ESD immunity test repeatability," in *Proc. 17th Symposium IMEKO TC 4-Measurement of Electrical Quantities 15th International Workshop on ADC Modelling and Testing 3rd Symposium IMEKO TC 19-Environmental Measurements, IMEKO 2010*, Kosice, Slovakia, Sep. 2010, pp. 1–5.

[32] F. Maradei and M. Raugi, "Analysis of upsets and failures due to ESD by the FDTD-INBCs method," *IEEE Trans. Ind. Appl.*, vol. 38, pp. 1009–1017, Aug. 2002.

[33] C. Qing, J. Koo, A. Nandy, D. Pommerenke, J. S. Lee, and B. S. Seol, "Advanced full wave ESD generator model for system level coupling simulation," in *Proc. Int. Symp. on EMC*, Detroit, USA, Aug. 2008, pp. 1–6.

[34] A. Wallash and A. Tazzoli, "Application of 3-D electromagnetic modeling to ESD design and control for Class 0 devices," in *Proc. EOS/ESD Symposium*, Detroit, USA, Sep. 2009, pp. 1–7.

[35] G. Cerri, S. Chiarandini, S. Costantini, R. De Leo, V. M. Primiani, and P. Russo, "Theoretical and experimental characterization of transient electromagnetic fields radiated by electrostatic discharge (ESD) currents," *IEEE Trans. Electromagn. Compat.*, vol. 44, pp. 139–147, Feb. 2002.

[36] G. Cerri, R. De Leo, and V. M. Primiani, "ESD indirect coupling modeling," *IEEE Trans. Electromagn. Compat.*, vol. 38, pp. 274–281, Aug. 1996.

[37] W. D. Greason, "Idealized model for charged device electrostatic discharge," *IEEE Trans. Ind. Appl.*, vol. 35, pp. 240–258, Feb. 1999.

[38] ——, "Methodology for the characterization of the electrostatic discharge (ESD) event for bodies in approach," *IEEE Trans. Ind. Appl.*, vol. 37, pp. 488–494, Apr. 2001.

[39] *Electromagnetic Compatibility-Part 4-2: Testing and Measurement Techniques-Electrostatic discharge immunity test*, IEC Std. 61 000-4-2, 2008.

[40] *Road vehicles-Test methods for electrical disturbances from electrostatic discharges*, ISO Std. 10 605, 2008.

[41] M. Borsero, A. Sardi, and G. Vizio, "Calibration methods for electrostatic discharge generators," in *CPEM 2008 Conf. Digest*, Broomfield, USA, Jun. 2008, pp. 504–505.

[42] M. Borsero, A. Morando, A. Sardi, and G. Vizio, "Practical experience in calibration of ESD generators," in *CPEM 2010 Conf. Digest*, Daejeon, Korea, Jun. 2010, pp. 749–750.

[43] J. Koo, Q. Cai, D. Pommerenke, K. Wang, J. Mass, M. Hirata, and A. Martwick, "The repeatability of system level ESD test and relevant ESD generator parameters," in *Proc. Int. Symp. on EMC*, Detroit, USA, Aug. 2008, pp. 1–6.

[44] J. Sroka and W. L. Klampfer, "Target influence of the calibration uncertainty of ESD simulators," in *Proc. of INCEMIC 2003*, Chennai, India, Dec. 2003, pp. 241–244.

[45] J. Baran and J. Sroka, "Distortion of ESD generator pulse due to limited bandwidth of verification path," *IEEE Trans. Electromagn. Compat.*, 2010, to be published.

[46] EMTest. ESD Generators. [Online]. Available: http://www.emtest.com/products/overview_esd.php

[47] S. Caniggia and F. Maradei, "Numerical prediction and measurement of ESD radiated fields by free-space field sensors," *IEEE Trans. Electromagn. Compat.*, vol. 49, pp. 494–503, Aug. 2007.

[48] R. Zaridze, D. Karkashadze, R. Djobava, D. Pommerenke, and M. Aidam, "Numerical calculation and measurement of transient fields from electrostatic discharges," *IEEE Trans. Compon., Packag., Manuf. Technol. C*, vol. 19, pp. 178–183, Dec. 1996.

[49] A. Ruehli, "Equivalent circuit models for three-dimensional multiconductor systems," *IEEE Trans. Microw. Theory Tech.*, vol. 22, pp. 216–221, Mar. 1974.

[50] G. Antonini, "Fast multipole method for time domain PEEC analysis," *IEEE Trans. Mobile Comput.*, vol. 2, pp. 275–287, Oct. 2003.

[51] S. V. Kochetov, M. Leone, and G. Wollenberg, "PEEC formulation based on dyadic green's functions for layered media in the time and frequency domains," *IEEE Trans. Electromagn. Compat.*, vol. 50, pp. 953–965, Nov. 2008.

[52] G. Antonini, S. Cristina, and A. Orlandi, "PEEC modeling of lightning protection systems and coupling to coaxial cables," *IEEE Trans. Electromagn. Compat.*, vol. 40, pp. 481–491, Nov. 1998.

[53] J. F. Fan, H. Shi, A. Orlandi, J. L. Knighten, and J. L. Drewniak, "Modeling dc power-bus structures with vertical discontinuities using a circuit extraction approach based on a mixed-potential intergral equation formulation," *IEEE Trans. Adv. Packag.*, vol. 24, p. 143–157, May 2001.

[54] G. Wollenberg and A. Goerisch, "Analysis of 3-d interconnect structures with PEEC using SPICE," *IEEE Trans. Electromagn. Compat.*, vol. 41, pp. 412–417, Nov. 1999.

[55] M. Enohnyaket and J. Ekman, "Analysis of air-core reactors from dc to very high frequencies using PEEC models," *IEEE Trans. Power Del.*, vol. 24, pp. 719–729, Apr. 2009.

[56] J. Aime, J. Roudet, E. Clavel, . Aouine, C. Labarre, F. Costa, and J. Ecrabey, "Prediction and measurement of the magnetic near field of a static converter," in *Industrial Electronics, 2007. ISIE 2007. IEEE International Symposium on*, Vigo, Spain, Jun. 2007, pp. 2550–2555.

[57] H. Hebb and A. Ruehli, "Three-dimensional interconnect analysis using partial element equivalent circuits," *IEEE Trans. Circuits Syst. I*, vol. 39, pp. 974–982, Nov. 1992.

[58] E. Tonti, "Finite formulation of the electromagnetic field," in *Progress In Electromagnetics Research, PIER*, Jun. 2001, pp. 1–44.

[59] A. E. Ruehli, "Inductance calculations in a complex integrated circuit environment," *IBM J. RES. DEVELOP.*, pp. 470–481, Sep. 1972.

[60] A. E. Ruehli and P. Brennan, "Efficient capacitance calculations for three-dimensional multiconductor systems," *IEEE Trans. Microw. Theory Tech.*, vol. 21, pp. 76–82, Feb. 1973.

[61] M. Al-Qedra, J. Aronsson, and V. Okhmatovski, "A novel skin-effect based surface impedance formulation for broadband modeling of 3-d interconnects with electric field integral equation," *IEEE Trans. Microw. Theory Tech.*, vol. 58, pp. 3872–3881, Dec. 2010.

[62] K. M. Coperich, A. E. Ruehli, and A. Cangellaris, "Enhanced skin effect for partial-element equivalent-circuit (peec) models," *IEEE Trans. Microw. Theory Tech.*, vol. 48, pp. 1435–1442, Sep. 2000.

List of Papers

Fonte dati: Sito docente MiUR-Cineca

Regular Papers

- Chiampi M., Crotti G., Morando A., Evaluation of Flexible Rogowski Coil Performances In Power Frequency Applications, IEEE TRANSACTIONS ON INSTRUMENTATION AND MEASUREMENT, IEEE, pp. 9, 2011, Vol. 60, ISSN: 0018-9456, DOI: 10.1109/TIM.2010.2060223
- Morando A., Borsero M., Sardi A., Vizio G., Critical Aspects in Calibration of ESD Generators, MEASUREMENT SCIENCE REVIEW, pp. 6, 2011, Vol. 11, ISSN: 1335-8871, DOI: 10.2478/v10048-011-0002-5

Proceedings

- Borsero M., Morando A., Sardi A., Vizio G., Practical Experience in Calibration of ESD generators, In: Digest CPEM2010, CPEM 2010, Conference on Precision Electromagnetic Measurement, Daejeon, Korea 13-18 June 2010, pp. 2, 2010, ISBN: 9781424467969
- Morando A., Borsero M., Sardi A., Vizio G., Modeling and Practical Suggestions to Improve ESD Immunity Test Repeatability, In: 17th Symposium IMEKO TC 4 - Measurement of Electrical Quantities 15th International Workshop on ADC Modelling and Testing 3rd Symposium IMEKO TC 19 - Environmental Measurements, IMEKO 2010, Kosice, Slovakia Sept. 8-10, 2010, pp. 5, 2010, ISBN: 9788055304243
- Crotti G., Giordano D., Morando A., Analysis of Rogowski Coil Behavior Under Non Ideal Measurement Conditions, IMEKO XIX World Congress, Lisbona (Portogallo) Sept. 2009, pp. 6, 2009, ISBN: 9789638841001